DISSIPATIVE HEATING AND NONTHERMAL DISTRIBUTIONS IN BLACK HOLE ACCRETION FLARING EVENTS

BY

ERIC PETERSEN

DISSERTATION

Submitted in partial fulfillment of the requirements
for the degree of Doctor of Philosophy in Physics
in the Graduate College of the
University of Illinois at Urbana-Champaign, 2020

Urbana, Illinois

Doctoral Committee:

Professor Gilbert Holder, Chair
Professor Charles F. Gammie, Director of Research
Professor Jeffrey P. Filippini
Professor S. Lance Cooper

Abstract

The center of the Milky Way galaxy contains a supermassive black hole called Sgr A*, which has been observed at radio, mm, X-ray, and near infrared (NIR) wavelengths. The NIR emission flares about once per day with the flaring state being about an order of magnitude brighter than the non-flaring state. These flares have a flat spectrum which drops off at high frequency much slower than would be expected from thermal emission alone. This thesis describes work to model these flares using general relativistic magnetohydrodynamics (GRMHD) and radiative transfer calculations with a nonthermal κ distribution function (which effectively adds a power-law tail to the thermal distribution) for electrons accelerated by resistive heating in reconnecting current sheets. This approach is well supported by the literature on the acceleration of electrons in magnetized plasma, which shows that current sheets do accelerate electrons and those electrons can have an distribution function similar to a κ distribution. In axisymmetric (two dimensional) simulations presented here, a model with a constant fraction of electrons in the κ distribution is able to enhance NIR emission, but is unable to produce any substantial variability in the NIR flux density. Similar models which heat electrons through resistive dissipation are able to produce flares. In three dimensional standard and normal evolution (SANE) and magnetically arrested disk (MAD) models, the total current in the simulation showed only small variability. This resulted in some small-scale variability in the light curve, but no flares are observed. In all cases, nonthermal models were able to reproduce the observed spectral slope of Sgr A* in the NIR region.

Acknowledgements

I would like to thank my advisor, Dr. Charles Gammie, for helping me through the long process of conducting my research. Dr. Gammie's patient advice has made my work possible and his vast knowledge of astrophysics and numerical methods has greatly aided my research. I would also like to thank the other members of my committee. Dr. Gil Holder and Dr. Jeff Filippini have provided insightful comments during weekly seminars and during my preliminary exam. Dr. Lance Cooper has given valuable advice throughout my graduate career. Finally, Dr. Stu Shapiro has given me many instructive comments through courses, seminars, and my preliminary exam.

Thanks are also due to my fellow students in Dr. Gammie's research group: Hotaka Shiokawa, Mani Chandra, Ben Ryan, George Wong, Ben Prather, Patrick Mullen, Vedant Dhruv, and Alex Pandya. I would like to thank these people for guidance and for helpful discussions about astrophysics and numerical methods. Most importantly, however, I would like to thank them for many, many invaluable comments as I was drafting various documents (especially the many iterations of this thesis) and sitting through all of the rehearsals needed to prepare me for presentations (especially my defense).

I would also like to thank several of my friends outside of the research group. Specifically, I would like to thank Dr. Vatsal Dwivedi, Dr. Bill Karr, Dr. Tom Rao, Vasilios Passias, Souvik Dutta, Oleg Dubinkin, Veronika Dubinkina, and Andrew Lei. I would like to thank them for their support and help drafting my thesis and rehearsing my defense. Finally, I would like to thank my family for their love and support. I would especially like to thank my sister, Dr. Rebecca Petersen.

Contents

1 Introduction

This thesis will discuss attempts to model the near infrared (NIR) flares observed from the source at the center of the Milky Way galaxy, Sgr A*, by using reconnecting current sheets to accelerate electrons into a nonthermal distribution function. To start off, chapter 1 will explain what type of source Sgr A* is, summarize the observations of the source, review previous attempts at modeling the NIR flares, and discuss the nonthermal distribution function used as well as how current sheets can heat electrons into this distribution function. Then, chapter 2 will go over the numerical methods used to perform the calculations. Chapter 3 will present results from a variety of axisymmetric models. In chapter 4, results from fully three dimensional simulations will be discussed. Similarly, chapter 5 will show results from a different set of three dimensional simulations, this time with larger magnetic fields which affect the plasma accretion rate. Chapter 6 will provide a summary and discuss possible avenues for future research

1.1 Astrophysical Background

The numerical models presented in this work exist in a rich astrophysical context. The basics of the system to be simulated, plasma accreting onto a black hole, must be understood before the relevance of the work of presented here can be fully appreciated. In the study of these systems, a terminology has developed which will be used throughout this work. Here, the relevant astrophysical systems will be introduced and some degree of familiarity with the language used to describe them will be provided.

1.1.1 Kerr Black Holes

The general theory of relativity is one of the most remarkable developments of 20th century physics. It forces one to abandon a naïve understanding of such basic concepts as space, time, and geometry while entirely reworking how one is to view gravity. Nevertheless, all tests of the theory have confirmed it. However, it has been impractical, until recently, to test this theory in the strong-field limit. The most obvious tool to use for such a test is a black hole. Matter radiating in the region around a black hole exists in an extreme environment that can be very difficult to model.

In order to numerically model such a system, one must begin by describing the metric in the computational domain. The mass of an accreting black hole is dominated by the hole itself, so the self-gravity of the surrounding matter can be safely ignored. As a charged black hole would preferentially accrete matter of the opposite charge, any astrophysical black hole can be assumed to be uncharged to a high degree of accuracy. There is no similar argument to be made about the angular momentum, however. Thus, it is proper to use the Kerr metric (Kerr, 1963), the line element for which is given by equation 1.1.

$$\begin{aligned} ds^2 = &-\left(1-\frac{2Mr}{\Sigma}\right)dt^2 - \frac{4Mar\sin^2(\theta)}{\Sigma}dtd\phi + \frac{\Sigma}{\Delta}dr^2 + \\ &\Sigma d\theta^2 + \left(r^2+a^2+\frac{2Ma^2r\sin^2(\theta)}{\Sigma}\right)\sin^2(\theta)d\phi^2 \end{aligned} \tag{1.1}$$

Here, (t, r, θ, ϕ) are the Boyer-Lindquist coordinates, M is the mass of the black hole, a is the dimensionless spin parameter on the interval [0,1), $\Sigma \equiv \mathrm{r}^2 + \mathrm{a}^2\cos^2(\theta)$, $\Delta \equiv \mathrm{r}^2 - 2\mathrm{r} + \mathrm{a}^2$, and geometric units, such that G=1=c, are used.

There are several consequences of this metric (Misner et al., 1973). One is an event horizon located at $\mathrm{r_h} = \mathrm{M} + \sqrt{\mathrm{M}^2 - \mathrm{a}^2}$; matter within this radius cannot radiate to observers at infinity. Another surface, $\mathrm{r_E} = \mathrm{M} + \sqrt{\mathrm{M}^2 - \mathrm{a}^2\cos^2(\theta)}$, defines the outer boundary of the so-called ergosphere, inside of which matter must corotate with the black hole. There are also the so-called photon orbits. These are null geodesics which neither escape to infinity nor cross the event horizon. In general, these orbits can be complicated but, in the equatorial plane, there are two (prograde, denoted with a +, and retrograde, denoted with a -) unstable solutions: $\mathrm{r}_{\pm} = 2\mathrm{M}\,(1+\cos{(2/3\,\arccos{(\pm|\mathrm{a}|/\mathrm{M})})})$. Finally, there is the innermost stable circular orbit (ISCO), inside of which any perturbation to a circular orbit will cause a test particle to cross the event horizon or escape to infinity. For a nonspinning black hole, this occurs at $\mathrm{r}_{\mathrm{ISCO}}$=6M, for a maximally spinning black hole rotating opposite to the angular momentum of the test particle $\mathrm{r}_{\mathrm{ISCO}}$=9M, and for a maximally spinning black hole with angular momentum aligned with the test particle's orbital angular momentum $\mathrm{r}_{\mathrm{ISCO}}=\mathrm{r}_{\mathrm{h}}$ (see Bardeen et al., 1972, for the full expression). If an object on a nearly circular orbit crosses the ISCO it will rapidly fall to the event horizon. Thus, the volume $r_h < r < r_{ISCO}$ is referred to as the plunging region.

1.1.2 Black Hole Accretion

Some of the most luminous objects in the universe are thought to be powered by gas accretion onto black holes with masses in excess of 10^6 solar masses; these objects are called supermassive black holes (SMBHs). Many galaxies, including the Milky Way, are thought to have an SMBH in their core; this is inferred from the characteristics of stellar orbits and the motion of gas clouds in the core. For the brightest of these sources, the radiation can be so intense that it causes a pressure large enough to balance the gravitational force; for a spherically symmetric system, this is called the Eddington luminosity, L_{E} (see, e.g., Padmanabhan, 2000). Equation 1.2 expresses the Eddington luminosity in terms of the black hole mass, M_{BH}, the Thomson cross section, σ_{T}, proton mass, m_{p} (the plasma is assumed to be pure Hydrogen), the mass of the sun, $M_{\odot}$, and the luminosity of the sun, $L_{\odot}$.

$$L_E = \frac{4\pi G M m_p c}{\sigma_T} \approx 3\times 10^4 \frac{M L_{\odot}}{M_{\odot}} \tag{1.2}$$

If this radiation occurs with an accretion rate of $\dot{\mathrm{M}}$ and gravitational energy is transformed to radiation with an efficiency of η, then the luminosity would be $\mathrm{L} = \eta\dot{\mathrm{M}}\mathrm{c}^2$. Thus, the Eddington accretion rate can be defined according to equation 1.3.

$$\dot{M}_E = \frac{L_E}{\eta c^2} = \frac{4\pi G M_{BH} m_p}{\eta c \sigma_T} \tag{1.3}$$

As matter from the host galaxy falls onto the black hole, gravitational energy becomes available to be radiated away (see Netzer, 2006) through a variety of mechanisms (e.g., synchrotron radiation, bremsstrahlung, and Compton scattering) at a wide range of frequencies from γ rays through radio waves. Under certain conditions, accreting matter can also gain energy from the interaction of the electromagnetic field produced by the accreting matter and a spinning black hole (see Blandford and Znajek, 1977). The characteristics (i.e., intensity, spectrum, and variability) of the resulting emission depends on several factors including the mass of the black hole, the spin of the black hole, the accretion rate, and the viewing angle.

The brightest non-transient objects in the observable universe, active galactic nuclei (AGNs), are powered by rapidly accreting SMBHs. AGNs form a very diverse class of objects — as evidenced by the number of subcategories (see, e.g., Tadhunter, 2008; Padovani, 1997). The main distinctions between these subcategories are the radio luminosity and the width of optical emission lines. Sources that are "radio–quiet" with narrow lines include Seyfert 2 galaxies, sources that are radio–quiet but include broad lines include Seyfert 1 galaxies and radio quiet quasars (RQQs, which account for most quasars, or QSOs), radio–loud sources with narrow optical emission lines include narrow–line radio galaxies (NLRGs), and radio–loud sources with broad lines include broad–line radio galaxies (BLRGs) and radio–loud quasars (steep spectrum radio quasars, SSRQs, and flat spectrum radio quasars, FSRQs). Other AGNs show optical variability; examples include the brightest AGNs: blazars. Blazars appear far more luminous than other AGNs primarily because they have a relativistic jet that happens to be pointing at Earth. Viewing angle can also explain more subtle differences between AGN classification (e.g., broad optical emission lines may be blocked from view by a gas torus if viewed from the plane of the torus).

There is likely a small SMBH ($M_{BH} \sim 4 \times 10^6 M_\odot$) at the center of the Milky Way galaxy. Due to intersteller dust, radiation from this source is only visible in radio (Sgr A*, the name of the radio source, is often used to refer to the central object), mm, infrared, and X-ray frequencies. Due to its low luminosity, this SMBH is not considered to be an AGN.

1.2 Observations of Sgr A*

Sgr A* has been observed for many years at multiple frequencies. As any model of the source must account for these observations, they form the foundation of any attempt to understand the accretion flow. While some models can already explain certain observed characteristics of the emission, others, such as the variability in the near infrared (NIR) are more difficult to match. Upcoming observations, including mm images from the Event Horizon Telescope (Doeleman et al., 2008) and NIR astrometry and polarization data from GRAVITY (Gravity Collaboration et al., 2018), will also be exciting to compare to numerical models.

1.2.1 System Parameters

In order to compare the observed emission to the calculated emission, one must first know the mass of the central black hole and the distance between it and Earth. One method of determining the mass of the central mass is by observing the elliptical paths of stars that orbit it (the so–called “S–stars”) and applying Kepler’s Third Law. Figure 1.1, taken from Genzel et al. (2010a), shows some of these stars, with special emphasis on the one which passes closest to the central mass, S2. For the rest of this work, the mass given by Abuter et al. (2019), $M_{\rm BH} = (4.152 \pm 0.014) \times 10^6\ M_{\odot}$, will be used. The observed distance to the black hole of $(8.178 \pm 0.013 \pm 0.022)$ kpc from Abuter et al. (2019) will also be used.

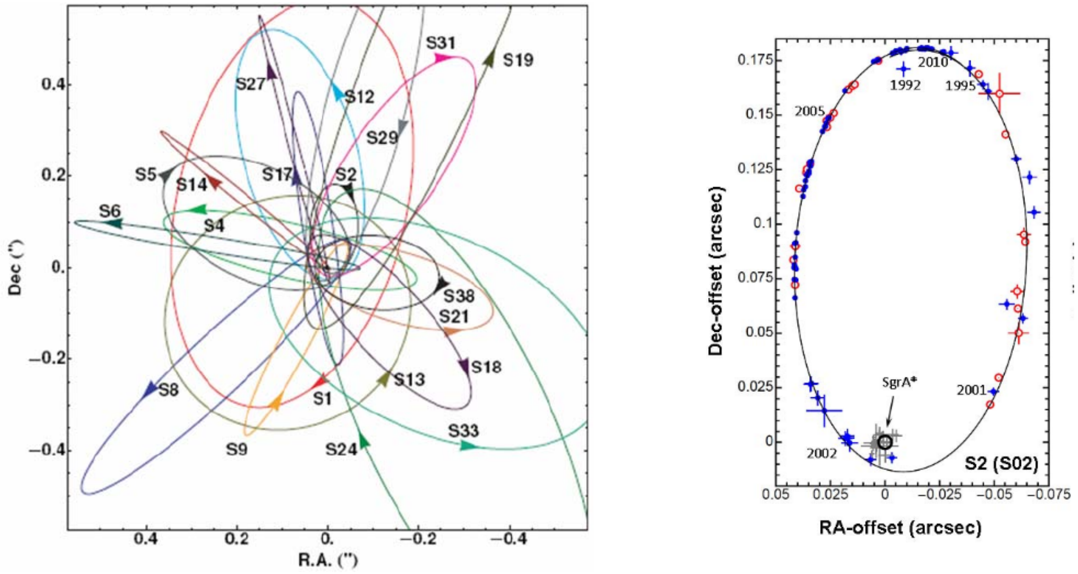

Figure 1.1: The orbits of stars near Sgr A*. *left*: several of the stars orbiting Sgr A* and traces of their orbits. *right*: a view concentrating on S2, the star which passes closest to Sgr A*. Images are duplicated from Genzel et al. (2010a) with data from Ghez et al. (2008), Gillessen et al. (2009a), and Gillessen et al. (2009b).

Observations can also constrain, albeit somewhat more loosely, the rate at which plasma is falling onto the central mass ($\dot{M}$). This can be done using the rotation measure. Rotation measure, RM, relates electric vector polarization angle, EVPA, to the frequency of radiation, ν. Rotation measure is dependent on the integral of the electron number density, n_e, and the component of the magnetic field parallel to the direction of propagation, $B_{\|}$, along the line of sight, $\mathrm{RM} = \int n_e B_{\|}$ (see Padmanabhan, 2000, chapter 9.5.1). Thus, an estimate of the electron number density can be obtained by using an estimate of the magnitude of the magnetic field at the source and measurements of the polarization at several frequencies. Using this method, an accretion rate of $2 \times 10^{-9}\ M_{\odot}\mathrm{yr}^{-1} < \dot{M}_{\rm SgrA*} < 2 \times 10^{-7}\ M_{\odot}\mathrm{yr}^{-1}$

has been obtained (Bower et al., 2005; Marrone et al., 2006a, 2007, see, e.g.,). Assuming a radiative efficiency of $\eta \sim$10%, then the accretion rate of Sgr A* is $2 \times 10^{-8} \dot{M}_{Edd} < \dot{M}_{SgrA*} < 2 \times 10^{-6} \dot{M}_{Edd}$. Given that the dynamics of accretion flows with $\dot{M}/\dot{M_{Edd}} < 10^{-7}$ are not greatly affected by radiative cooling (see Dibi et al., 2012), it is reasonable to neglect radiation in models of Sgr A*.

1.2.2 230GHz (mm)

Many observations of Sgr A* have been made at wavelengths of around one millimeter for over two decades (see Falcke et al., 1998a; Aitken et al., 2000; Melia et al., 2000; Bower et al., 2003; Marrone et al., 2006b). The mean 1.3 mm (230GHz) flux density for Sgr A* is 3.7Jy (Bower et al., 2015). This figure varies over time, with a standard deviation of ~0.7Jy (see e.g., Fish et al., 2011; Haubois et al., 2012; Bower et al., 2013; Liu et al., 2016). Figure 1.2 shows multi-day light curves at wavelengths of about 1mm taken from Bower et al. (2015).

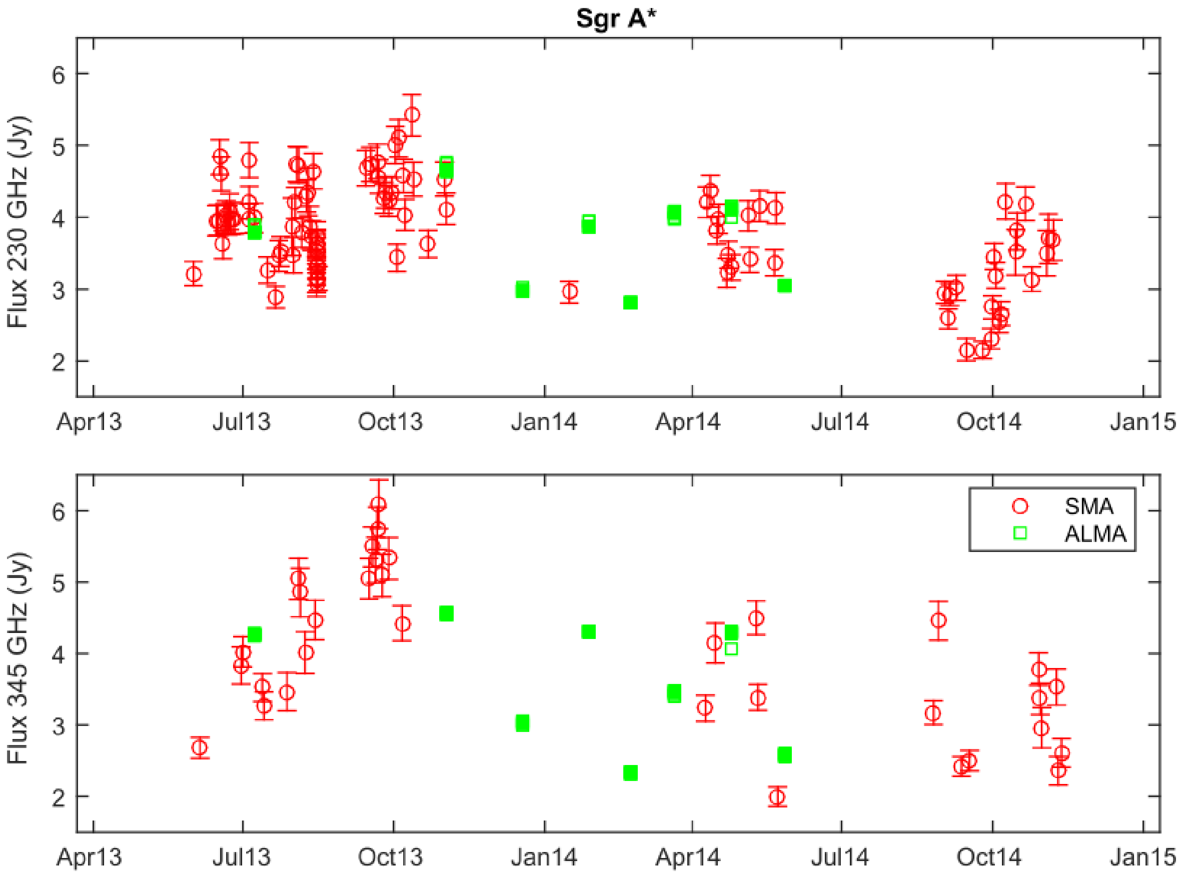

Figure 1.2: light curves from Bower et al. (2015) of Sgr A* at 230GHz and 345GHz.

The Event Horizon Telescope (EHT) collaboration has made very long baseline interferometry (VLBI) observations of Sgr A* at mm wavelengths which are able to resolve angular scales similar to the gravitational radius of the central black hole. While future observations of Sgr A* may provide resolved images of the central accretion flow, similar to work done with the AGN M87 (see Event Horizon Telescope Collaboration et al., 2019a,b,c,d,e,f), current measurements of Sgr A* are limited to the size of the image (described by its full width at half maximum, FWHM). Initial measurements showed a relatively small source size of 37 μas (Doeleman et al., 2008), but estimates have increased over time to 52 μas (Lu et al.,

2018) and, most recently, 60 μas (Johnson et al., 2018).

1.2.3 140THz (NIR)

Observations of Sgr A* at 2.2μm (140THz) indicate that the source is highly variable and that these variations are neither periodic nor quasi-periodic (Do et al., 2009). The most notable features of this variability are the flares with emission about an order of magnitude higher than the non-flaring state and which last about an hour (Dodds-Eden et al., 2009). Above 5 mJy, Dodds-Eden et al. (2011) find that the 2.2 μm flux density distribution follows a power law with index 2.7. This means that the fraction of the time that Sgr A* is observed at a flux density, F_ν, as a function of F_ν is higher for large values of F_ν than would be expected if there were no flaring state. A light curve from this work is reproduced in figure 1.3 and flux histograms from this work are presented in figure 1.4. Observations at 4.5 μm (using the Spitzer Space Telescope, see Hora et al., 2014) over a continuous ~24 hour period show a light curve with the flux density usually below 5 mJy and a flare with a duration of a few hours. Further observations of Sgr A* show that the NIR luminosity follows a power law in frequency: $\nu \mathrm{L}_\nu \propto \nu^\alpha$ with a spectral index of $\alpha \approx 0.4$ (see Gillessen et al., 2006; Hornstein et al., 2007; Marrone et al., 2008; Dodds-Eden et al., 2009; Witzel et al., 2012; von Fellenberg et al., 2018).

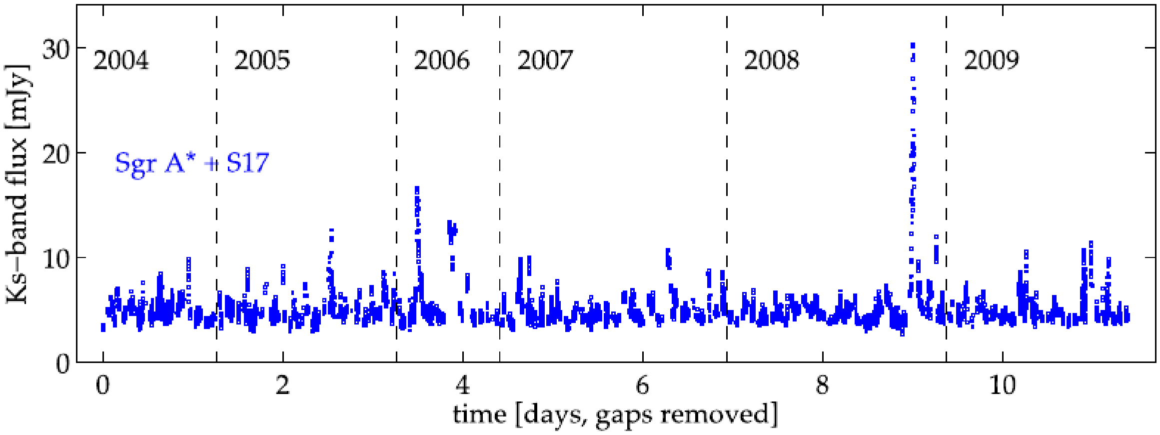

Figure 1.3: Light curve from Dodds-Eden et al. (2011) of Sgr A* at 2.2 μm.

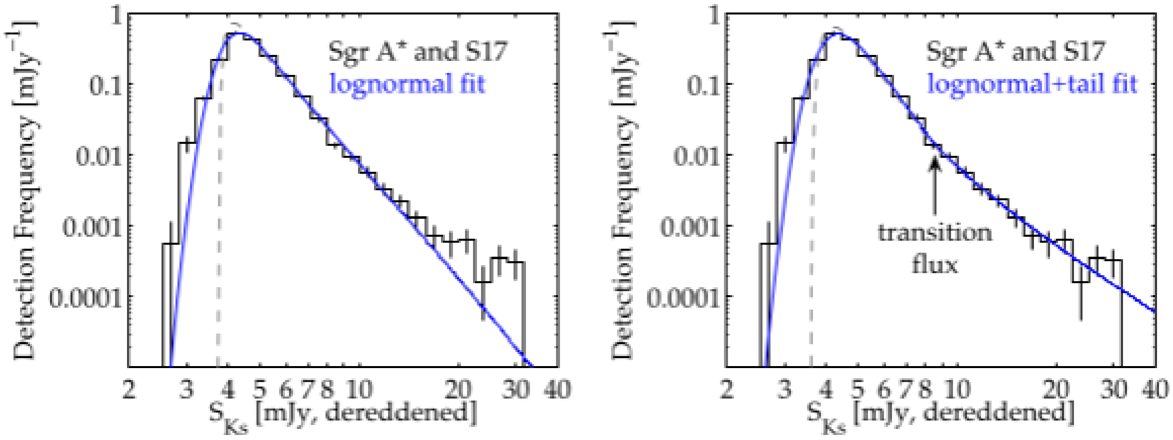

Figure 1.4: 2.2 μm flux density histograms of Sgr A* from Dodds-Eden et al. (2011).

Very large telescope interferometer (VLTI) observations of Sgr A* at 2.2 μm have been made by the GRAVITY collaboration (Gravity Collaboration et al., 2018). While this instrument is not able to produce spatially resolved images of the inner accretion flow (Eisenhauer et al., 2008) it can monitor the motion of the emission centroid with a precision of ∼10 μas. This motion has been measured (by Gravity Collaboration et al., 2018) as occurring on an angular scale of about 150 μas with a duration of around 45 minutes and indicating a face-on view of the orbit. Combining this with upcoming images from EHT gives two probes of the accretion flow very close to the central black hole.

1.2.4 Other Frequencies

The radio source at the center of the Milky Way Galaxy is called Sgr A* and it has been observed for several decades (Balick and Brown, 1974; Falcke et al., 1998a; Genzel et al., 2003; Baganoff et al., 2001; Ghez et al., 2008; Gillessen et al., 2009a; Genzel et al., 2010b). Sgr A* also appears in the X-ray; the X-ray light curve is characterized by large magnitude flares. These X-ray flares almost always occur during NIR flares, though many NIR flares have no associated X-ray flares (see e.g., Baganoff et al., 2001; Ponti et al., 2015). A spectral energy distribution (SED) composed of many independent observations and originally published by Genzel et al. (2010b) is reproduced in figure 1.5.

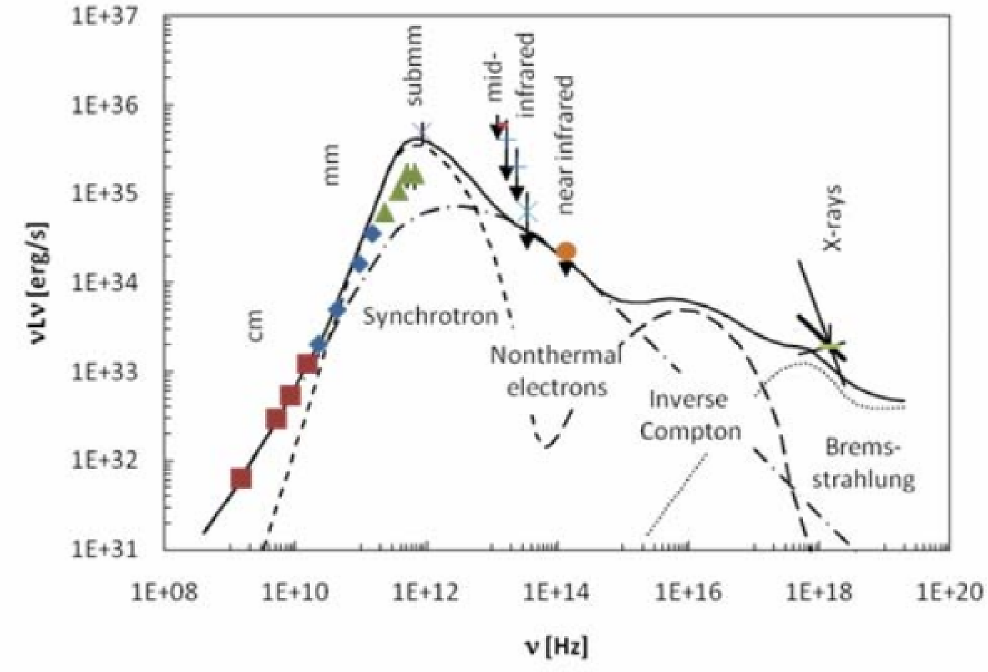

Figure 1.5: SED of Sgr A*from Genzel et al. (2010b) (with data from Zhao et al., 2001; Falcke et al., 1998b; Zylka et al., 1995; Serabyn et al., 1997; Cotera et al., 1999; Gezari, 1999; Schödel et al., 2007; Hornstein et al., 2002; Baganoff et al., 2003; Yuan et al., 2003a).

1.3 Reconnection and Heating

The core of this work is tying realistic fluid simulations to a physically motivated description for the acceleration of electrons into a nonthermal distribution function. Thus, it is important to discuss the particular distribution function to be used and also to describe the mechanism by which the acceleration takes place. These models assume that the acceleration is caused by resistive heating in current sheets and, therefore, set the heating rate proportional to the square of the fluid-frame 3-current density (see appendix A for a discussion of Ohm's law in the context of GRMHD). Various plasma simulations which support the physical basis for this model will be discussed at the end of this subsection.

1.3.1 Thermal and Nonthermal Distribution Functions

In these models, the electron distribution function has two components: a thermal portion described by a Maxwell-Jüttner distribution function and a nonthermal portion described by a relativistic κ distribution function (see Vasyliunas, 1968; Xiao, 2006; Pierrard and Lazar, 2010).

The Maxwell-Jüttner distribution function is given by equation 1.4, where $\mathrm{n_{e,T}}$ is the thermal electron number density, $\mathrm{K_2}$ is a modified Bessel function of the second kind, Θ_e is the electron temperature ($\Theta_e \equiv (k_B T_e) / (m_e c^2)$, where T_e is the temperature of the electrons), and the momentum space coordinates γ, ξ, and ϕ represent the Lorentz factor, pitch angle, and gyrophase, respectively.

$$\frac{\mathrm{d}n_{e,T}}{\mathrm{d}\gamma \mathrm{d}cos\xi \mathrm{d}\phi} = \frac{n_{e,T}\gamma \left(\gamma^2 - 1\right)^{1/2}}{4\pi\Theta_e K_2\left(\frac{1}{\Theta_e}\right)} \exp\left(-\frac{\gamma}{\Theta_e}\right) \tag{1.4}$$

The κ distribution function is given by equation 1.5, where $\mathrm{n_{e,NT}}$ is the number density of nonthermal electrons, and N is a normalization constant. There are also the parameters κ and w. A comparison of this distribution function and the Maxwell-Jüttner distribution function is given by figure 1.6.

$$\frac{dn_{e,NT}}{d\gamma\, dcos\xi\, d\phi} = \frac{N}{4\pi}\gamma\left(\gamma^2 - 1\right)^{1/2}\left(1 + \frac{\gamma - 1}{\kappa w}\right)^{-(\kappa+1)}. \tag{1.5}$$

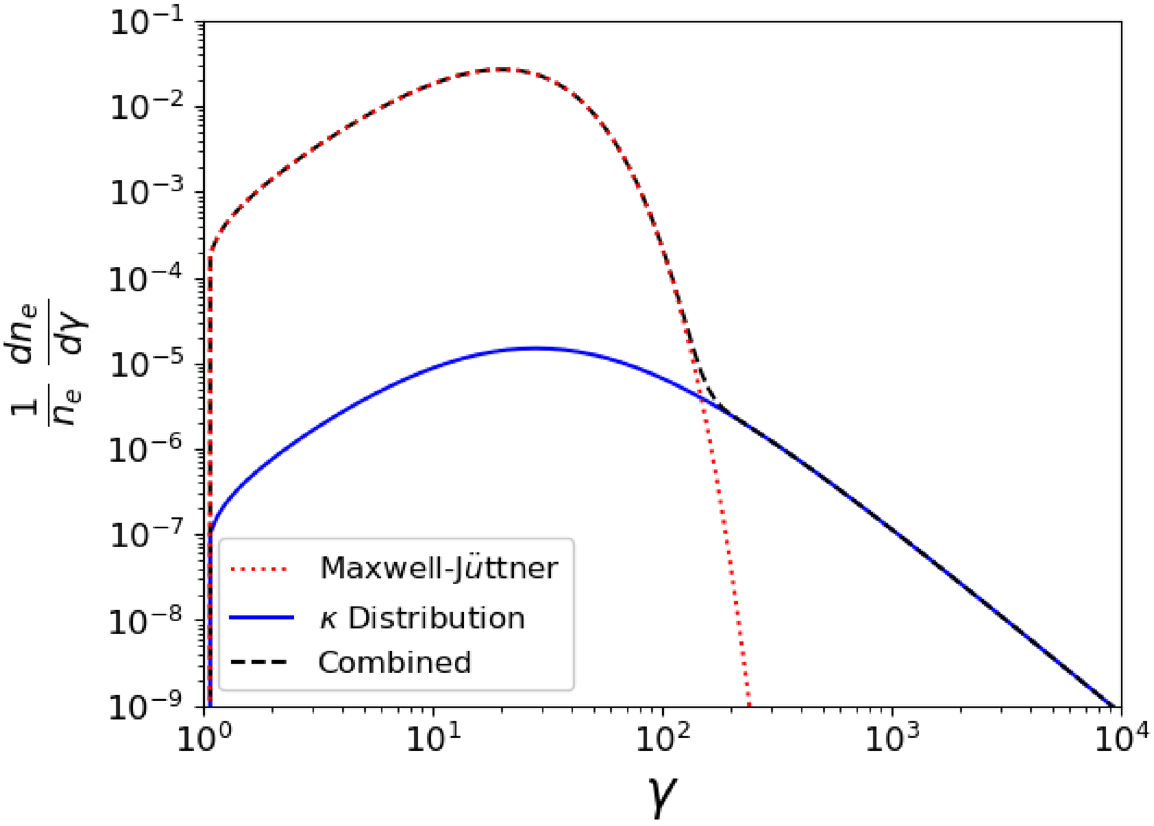

Figure 1.6: The combined distribution function is nearly identical to the thermal distribution at low γ and nearly identical to a power law at high γ. The transition to the power law tail is smooth; this is due to the choice w=Θ_e (which, in this case, is 10). The power law slope is set by the choice of κ; in this example, κ=3.2. The weighting of the distribution functions is such that the κ distribution accounts for 0.2% of the electrons.

At low γ, the κ distribution function is nearly thermal while at high γ, the distribution function is nearly a power law (where the distribution function is $f(\gamma) \propto \gamma^{-p}$, where -p is the power-law index, $d \ln f / d \ln \gamma$). The width parameter, w, determines the width of the thermal core. In the limit $\kappa \rightarrow \infty$, the distribution function approaches a Maxwell-Jüttner distribution function with temperature θ_e=w. In order to ensure a smooth total distribution function, all nonthermal models presented here set w=θ_e (where θ_e is the electron temperature calculated for the fluid). Thus, the dominant effect of the nonthermal electrons will be from the power law tail of the kappa distribution. The power law index of this portion of the distribution function is p $= \kappa - 1$.

1.3.2 Electron Acceleration Due to Reconnection

The relationship between plasma flows and sheets of electric current caused by magnetic reconnection has been known for well over three decades (see, e.g., Biskamp, 1986, 1996). Turbulent plasma flows generate X-points (see figure 1.7) where bulk fluid carries “frozen-in” magnetic field lines which are then topologically rearranged. This creates large, two-dimensional structures called Sweet-Parker current sheets (see e.g. Parker, 1957; Sweet, 1958). Simulations suggest that resistive dissipation in these structures cause the electron distribution function to acquire a power law tail.

Particle-in-cell (PIC) simulations evolve charged particles and electromagnetic fields to see how they interact; this makes them a perfect tool for ascertaining the distribution function of electrons in regions where heating is driven by currents. As it is difficult to resolve the behavior of species with very different mass ratios (as would be required for an ion-electron plasma), many of these simulations use a pair plasma (a plasma consisting solely of positrons and electrons) or an ion-electron plasma with the mass ratio artificially reduced. See Kagan et al. (2015) for a review of PIC simulations of pair plasmas.

Three dimensional pair plasmas studied by PIC simulation (see Liu et al., 2011) indicate that particle acceleration occurs in reconnecting regions but also (indeed, mostly) in the magnetic islands that accompany them. The distinction between these regions is unimportant for GRMHD accretion simulations as the spatial separation between magnetic islands and reconnection regions within the current sheets is much too small to be resolved. The dissipative heating is found to primarily produce a hot, thermal population of electrons, al-

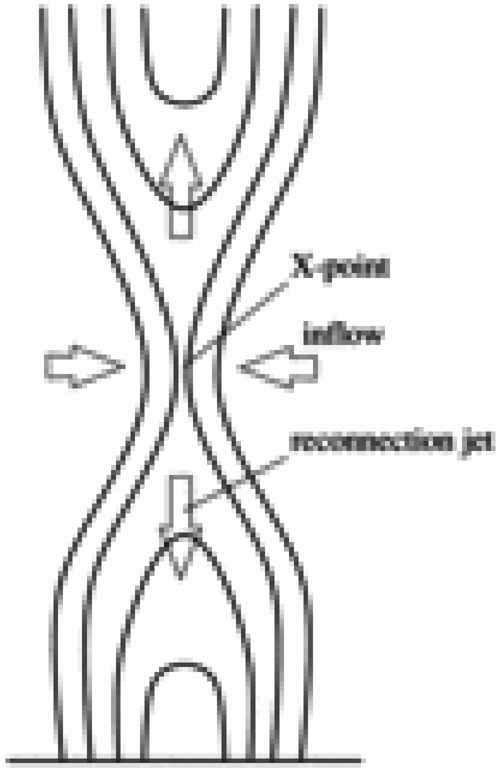

Figure 1.7: A diagram of a reconnecting X-point originally published by Yokoyama et al. (2001). Plasma (arrows) flows into the X-point (center) from the left and right. Magnetic field lines (solid lines) are frozen in with the fluid so that field lines are drawn towards the X-point with the fluid. At the region with high current near the center, the antiparallel field lines meet, break (top separating from bottom), and reconnect (left merging with right). As the fluid flows out, it drags the magnetic field lines with it, to create two U-shaped field lines.

though a nonthermal population is also present. Another three dimensional positron-electron PIC simulation (see Makwana et al., 2017) shows that current sheets produce dissipation in regions of low plasma β (i.e., regions with a low ratio of gas pressure to magnetic pressure). These heated electrons were found to exhibit a nonthermal tail at high energies.

A two dimensional (PIC) simulation of a pair plasma (see Cerutti et al., 2012) shows that magnetic dissipation due to reconnection can change the electron distribution. In this work, the resultant distribution function did not show a power law tail but scaled as $\gamma^{-1/2}\exp(-\gamma/5)$, where γ is the electron Lorentz factor. Continued work in three dimensions (Cerutti et al., 2013) shows an electron distribution function which follows a power law with index -2 due to synchrotron cooling of the high energy tail. Continued work in Cerutti et al. (2014) shows that this production of nonthermal electrons is less pronounced without an external field.

PIC simulations of pair plasmas in both 2D and 3D carried out by Sironi and Spitkovsky (2014) also show magnetic heating of electrons into non-thermal distribution functions. In two dimensions, the power law index of the distribution varies with the magnetization (σ, the ratio of magnetic energy to rest-mass energy), with an index of p $\approx$ 1.5 for $\sigma \approx 50$ and p $\approx$ 4 for $\sigma \approx 1$. This same work finds that a 3D simulation also produces a power law tail to the distribution function. In this case the magnetization was $\sigma = 10$ and produced a power law index of p $\sim$ 2.3 (similar to the 2D case with $\sigma = 10$ which produces an index of p $\sim$ 2.0). In both the two and three dimensional cases the distribution function evolved from a thermal distribution to the nonthermal distribution, but in three dimensions the amplitude of the power law tail was somewhat reduced and the high energy cutoff came at lower energy.

The literature on ion-electron plasmas is less extensive than pair plasmas. A two dimensional PIC simulation (see Siversky and Zharkova, 2009) of an ion-electron plasma (with the proton to electron mass ratio reduced to 100) find that a wide electron distribution function (with its width similar to its mean) arises in current sheets. Other two dimensional PIC simulations of an ion-electron plasma (with mass ratios from 1 to 20), reported by Riquelme et al. (2012), show both viscous and resistive electron heating. The acceleration due to reconnection produced a power law tail in the electron distribution function with a power law index ∼1.5.

A local shearing-box model (see Kunz et al., 2016) showed a collisionless disk with an ion distribution function well approximated by a κ distribution function with $\kappa \sim 5$. This was done by modeling the electrons as an isothermal fluid (hence, no information could be obtained about the electron distribution function) while the ions were treated kinetically.

Reconnection has long been thought to be important to the dynamics of solar flares (see Parker, 1963). Observations of the solar corona show filaments (believed to parallel magnetic field lines) merging at the same location (the X-point) where the plasma is inflowing from opposite directions (Shibata, 1996; Yokoyama et al., 2001). Continued observations (see, e.g., Su et al., 2013) show that the plasma outflow speed can be an order of magnitude greater than the inflow speed. Further work (see, e.g., Aschwanden, 2020) proposes that reconnection dissipates energy at a rate roughly proportional to B^2 (the square of the magnitude of the magnetic field).

1.4 Review of Previous Work

There have been many attempts to model the NIR variability displayed by Sgr A*. These models have used both thermal and nonthermal electron distribution functions. While many of these models have had success in reproducing some of the observed statistics of the 2.2 μm light curves, none of these models have been able to match all of them. Thermal models in particular are not able to reproduce the observed IR spectral index.

One thermal GRMHD model (Dexter and Fragile, 2013) posits an accretion disk that is misaligned with the spin axis of the black hole. This creates shocks which raise the electron temperature in the inner portion of the disk. These hot electrons then produce NIR flares. The spectral index in the NIR region is sensitive to black hole spin and the inclination of the disk, but it cannot be made to match observations. Another consequence of this model is that the image centroid moves by 30–50 μas independently of the IR flux. Purely thermal simulations described in Chan et al. (2015a) showed an infrared flare caused by gravitational lensing of magnetically dominated regions (these regions are assumed to have constant electron temperature). These simulations showed the importance of magnetic field strength to the NIR radiation. Early work on accretion disks with large magnetic fields (see Bisnovatyi-Kogan and Ruzmaikin, 1974, 1976) show the importance of magnetic field. Further work (see Igumenshchev et al., 2003) showed that initially poloidal fields can lead to slowed accretion and eventually the terms MAD (magnetically arrested disk) was coined by Narayan et al. (2003) in opposition to the SANE (standard and normal evolution) disks with lower magnetic flux (either with a toroidal magnetic field or alternating poloidal magnetic field lines) (see, e.g., Narayan et al., 2012; Tchekhovskoy et al., 2011a). In Chan et al. (2015a), SANE models produce a log-normal distribution of fluxes at 2.2 μm while the MAD models produce a flat distribution at large fluxes.

The assignment of a temperature to the electrons, has a major influence on the calculated emission. For a thermal, collisionless plasma (i.e., when the timescale between particle collisions is much longer than the dynamical timescale), the temperature of the electrons is largely decoupled from the more massive protons. For this reason, Chael et al. (2018) separately evolves the electron temperature (a two-temperature fluid model) in three dimensional general relativistic magnetohydrodynamic (3D GRMHD) simulations which include electron heating due to viscous dissipation and radiative cooling. While NIR variability is produced, the largest flares are a factor of ∼3 too small compared to observations. Additionally, the NIR spectral slope is too negative. Gravity Collaboration et al. (2020) also evolves the electron and ion temperatures separately and incorporates heating from grid-scale dissipation (see, e.g., Ressler et al., 2015; Sądowski et al., 2017; Ressler et al., 2017). These models use various prescriptions for distributing the dissipated energy between ions and electrons based on the local magnetic field strength and fluid parameters for dissipation due to viscosity (see Howes, 2010) or magnetic reconnection (see Rowan et al., 2017; Zhdankin et al., 2019). With certain conditions (most importantly, the strong magnetic fields resulting from MAD models) these models can produce large flares and some also produce approximately correct spectral slopes in the NIR.

Work by Özel et al. (2000) found that IR and radio (cm) emission could be explained by adding a power law component to the electron distribution function, with less than 10% of the electron energy distributed to the nonthermal electrons. A model placing a small, constant fraction (by energy) of electrons in a power law electron distribution function in a radiatively inefficient accretion flow (RIAF) model (Yuan et al., 2003b) was able to produce enhanced NIR emission, but not flares. In Chan et al. (2009) a distribution function is constructed to be thermal at low γ and a broken power law at high γ. By then introducing a density perturbation a flare was observed; however, it was not as strong as many observed flares and this work was not fully general relativistic. This lack of variability indicates that any mechanism which accelerates the electrons must be variable.

This is done by Dodds-Eden et al. (2010), who present a non-general relativistic, non-conservative MHD model with an explicit resistivity used to heat reconnecting regions. The resulting IR light curves showed flares with an approximately correct amplitude lasting for somewhat longer than an hour. Another non-relativistic model (see Kusunose and Takahara, 2011) has electrons with a power law distribution function injected into a bubble of plasma being ejected from near the black hole. This provided an approximately correct spectral slope, though it varied during the flare, but does not account for how often these pockets of accelerated electrons are created or what mechanism drives them.

A fully relativistic GRMHD calculation (see Ball et al., 2016) with nonthermal electrons injected in regions with a low value of plasma β (that is, locations with large magnetic fields and, thus, possibly reconnection) and cooled by synchrotron radiation produces NIR flares close to the observed magnitude but not the observed spectral index or flux distribution. An axisymmetric general relativistic radiative magnetohydrodynamic (GRRMHD) simulation including nonthermal electrons was presented by Chael et al. (2017). This model injected power law electrons based on viscous heating, advected them with the bulk flow, and cooled them (due to adiabatic effects, synchrotron radiation, inverse Compton scattering, bremsstrahlung, and Coulomb coupling). This resulted in enhanced emission at NIR frequencies, but because the nonthermal electrons were primarily injected at large radii, where there is little variability, no flares were observed. Davelaar et al. (2018) describe a model with a κ distribution of electrons in the jet sheath and purely thermal electrons in the disk. This work did not produce any light curves, so the variability could not be studied, but the spectral slopes for both quiescent (with 1% of the electrons in the κ distribution) and flaring (with ∼5–10% of the electrons in the κ distribution) states did match observations.

2 Numerical Methods

Ideally, the accretion flow of Sgr A* would be well-described by an analytic model. Shakura and Sunyaev (1973) describe an analytic model for an accretion disk; Novikov and Thorne (1973) present a similar model in a relativistic context. Here, the disk is assumed to be stationary, axisymmetric, and geometrically thin (that is, the height at a given radius, H, is much smaller than the radius, r, or H/r $\lesssim 0.1$). In order for accretion to occur, matter needs to shed both energy and angular momentum. Energy can be radiated away and turbulence can transport angular momentum from the inner portion of the disk to the outer portion. The effect of this turbulence can be modelled as a viscosity. This viscosity, ν, can be caused by turbulence on length scales less than or comparable to the disk height and with velocity less than or comparable to the the sound speed, v_s. This can be parameterized as $\nu = \alpha v_s H$, where $0 < \alpha \lesssim 1$ is an adjustable, dimensionless parameter. Another potential source of viscosity, magnetic stress, would give rise to the same viscosity relation and the same range for α. In these so-called α-disk models, the disk parameters (density, temperature, height) are determined by α. Interestingly, the radiated energy per unit area per unit time, F, is independent of α (see equation 2.1, where G is Newton's universal constant of gravity, M is the black hole mass, and $\dot{\mathrm{M}}$ is the accretion rate).

$$F = \frac{3GM\dot{M}}{8\pi r^3}\left(1 - \sqrt{\frac{r_{ISCO}}{r}}\right) \tag{2.1}$$

The above model is valid for a radiatively efficient flow; this condition is usually satisfied for an accretion rate of $\dot{M}/\dot{M}_{Edd} > 10^{-2}$ (see Esin et al., 1997). This is not the case for Sgr A*, so a radiatively inefficient accretion flow (RIAF) model is needed. One class of these models is the advection dominated accretion flow (ADAF) models, where the accreting matter transports energy away through advection instead of through radiation (see, e.g., Narayan and Yi, 1994; Abramowicz et al., 1995; Chen et al., 1997). In ADAF models, the ions, which store most of the gravitational energy, are weakly coupled to the electrons, which produce most of the radiation. The weak coupling, along with low density, means that radiation can only slowly reduce the energy stored with the ions, making these systems radiatively inefficient.

While an ADAF model can account for the accreting matter's energy loss by advection, the angular momentum still needs to be removed. This can be achieved by the magnetorotational instability (MRI, see Balbus and Hawley, 1991; Hawley and Balbus, 1991). To understand the MRI, imagine two adjacent regions of plasma in the accretion flow. Magnetic tension will tend to oppose any separation of these regions even as differential rotation causes the inner region to move ahead of the outer region. The magnetic tension acts like a spring between the two pockets of plasma and pulls back on the inner region and forward on the outer region. This causes the inner portion to lose angular momentum (and, thus, move to lower radius) and the outer portion to gain angular momentum (and, thus, to move to larger radius). Not only does this create an instability, but it also causes angular momentum to be transferred outward.

2.1 GRMHD

A powerful numerical tool for modeling ADAFs, as well as other problems, is general relativistic magnetohydrodynamics (GRMHD). In GRMHD, fluid is modeled under conditions where magnetic fields have an energy density comparable to the internal energy of the fluid and where gravitational fields are strong enough that general relativistic effects become noticeable; both of these conditions can be met near a black hole. The models considered in the work described here use ideal MHD, where the conductivity is assumed to be high enough to ensure that the Lorentz force in the fluid frame is zero (that is, $\vec{E} = -\vec{v} \times \vec{B}$) everywhere. These models are also collisionless, i.e., the timescale between particle collisions is assumed to be long compared to the dynamical timescale (which is of order $\mathrm{GM_{BH}/c^3}$) and the mean free path for collisions is assumed to be large compared to the system size (here, that is of order $\mathrm{GM_{BH}/c^2}$).

In GRMHD, conservation of particle number is given by equation 2.2 (see, e.g., Gammie et al., 2003; McKinney and Gammie, 2004). Here, ρ=mn is the rest mass density (with n the number density and m the rest mass per particle; here, m is the mass of a proton), u^μ is the fluid's bulk 4-velocity, and g is the determinant of the metric tensor: $g = det(g_{\mu\nu})$.

$$\frac{1}{\sqrt{-g}}\partial_\mu\left(\sqrt{-g}\rho u^\mu\right) = 0 \tag{2.2}$$

The equations for the conservation of energy-momentum can be written in terms of the stress-energy tensor. The MHD stress-energy tensor can be broken into the fluid and electromagnetic portions, as in equation 2.3.

$$T^{\mu\nu}_{MHD} = T^{\mu\nu}_{fluid} + T^{\mu\nu}_{EM} \tag{2.3}$$

The fluid portion of the stress-energy tensor (see Misner et al., 1973) is dependent on the internal energy density, u, and pressure, p, of the fluid, as seen in equation 2.4. In the simulations used here, the pressure is related to the internal energy density by a simple γ-law equation of state (see equation 2.5). In the nonrelativistic limit, appropriate for ions in a RIAF model, γ=5/3; in the ultrarelativistic limit, appropriate for electrons in a RIAF model, γ=4/3. For a neutral ion-electron plasma, the fluid as a whole is generally described with an adiabatic index of γ=13/9.

$$T^{\mu\nu}_{fluid} = (\rho + u + p)\, u^\mu u^\nu + p g^{\mu\nu} \tag{2.4}$$

$$p = (\gamma - 1)\, u \tag{2.5}$$

The electromagnetic portion of the stress-energy tensor, given by equation 2.6, can be written in terms of $F^{\mu\nu}$, the electromagnetic tensor (or "Faraday" in Misner et al. (1973)), which, in turn, can be written in terms of the four potential, A^{μ}, as shown in equation 2.7.

$$T^{\mu\nu}_{EM} = \frac{1}{4\pi}\left(F^{\mu\alpha}F^{\nu}{}_{\alpha} - \frac{1}{4}g^{\mu\nu}F_{\alpha\beta}F^{\alpha\beta}\right) \tag{2.6}$$

$$F_{\mu\nu} = \partial_{\mu}A_{\nu} - \partial_{\nu}A_{\mu} \tag{2.7}$$

This can be written in a more physically insightful manner by writing the zero Lorentz force condition in terms of the electromagnetic tensor, as in equation 2.8, and defining a magnetic four vector as in equation 2.9. Here, the Levi-Civita pseudotensor is represented by $\epsilon^{\mu\alpha\beta\gamma}$.

$$u_{\alpha}F^{\alpha\mu} = 0 \tag{2.8}$$

$$b^{\mu} \equiv \frac{1}{4\sqrt{\pi}}\epsilon^{\mu\alpha\beta\gamma}u_{\alpha}F_{\beta\gamma} \tag{2.9}$$

The Hodge dual of the Faraday tensor, ${}^{*}F^{\mu\nu}$ (called "Maxwell" in Misner et al. (1973)), is defined as ${}^{*}F_{\mu\nu} = \frac{1}{2}\epsilon_{\mu\nu\alpha\beta}F^{\alpha\beta}$. This can be rewritten as equation 2.10. This enables one to write Maxwell's equations as they are in equation 2.11.

$${}^{*}F^{\mu\nu} = b^{\mu}u^{\nu} - b^{\nu}u^{\mu} \tag{2.10}$$

$${}^{*}F^{\mu\nu}{}_{;\nu} = 0 \tag{2.11}$$

The ordinary magnetic field three vector, B^{i}, encodes components of the Maxwell tensor: $B^{i} = {}^{*}F^{it}$. This leads to relationships between the magnetic three-vector and the magnetic four-vector as given in equations 2.12–2.13. Finally, the time portion of equation 2.11 becomes the no magnetic monopoles constraint, equation 2.14, and the space portion becomes the evolution equation, equation 2.15.

$$b^t = B^i u^\alpha g_{i\alpha} \tag{2.12}$$

$$b^i = \frac{B^i + b^t u^i}{u^t} \tag{2.13}$$

$$\frac{1}{\sqrt{-g}}\partial_i\left(\sqrt{-g}B^i\right) = 0 \tag{2.14}$$

$$\partial_t\left(\sqrt{-g}B^i\right) = -\partial_j\left(\sqrt{-g}\left(b^j u^i - b^i u^j\right)\right) \tag{2.15}$$

GRMHD has been a popular method for simulating black hole accretion (see, e.g., De Villiers and Hawley, 2003; Anninos et al., 2005; Duez et al., 2005; Shibata and Sekiguchi, 2005; Mizuno et al., 2006; Antón et al., 2006; Anderson et al., 2006; Sekiguchi and Shibata, 2005; Giacomazzo and Rezzolla, 2007; Del Zanna et al., 2007; Cerdá-Durán et al., 2008; Yuan et al., 2009; Etienne et al., 2010; Kulkarni et al., 2011; Mościbrodzka and Falcke, 2013; Sądowski et al., 2015; Chan et al., 2015b; Chandra et al., 2017; Li et al., 2017; Ressler et al., 2018; Chael et al., 2018; Ryan et al., 2018, 2019, for some of the research using this tool). Implementations of GRMHD can include a wide variety of features: radiative cooling, dissipative heating, mesh refinement for greater accuracy, the ability to evolve the metric to simulate mergers between compact objects, and more.

GRMHD accretion simulations by Narayan et al. (2012) show different behavior from two classes of simulations. The standard and normal evolution (SANE) simulations have small magnetic flux around the black hole. Simulations with a magnetically arrested disk (MAD) have such high magnetic flux onto the black hole that the magnetic field has an impact on the fluid flow beyond causing angular momentum transfer through the MRI. SANE simulations can be created with initial conditions where the magnetic field lines form alternating poloidal loops; MAD simulations can be created by initial conditions with the magnetic field in a single poloidal loop, i.e., with a well-organized, large scale poloidal field.

2.1.1 `iharm` and `iharm3d`

This work makes use of the conservative, axisymmetric GRMHD code `iharm`[1], outlined in Gammie et al. (2003) and McKinney and Gammie (2004). The computational domain extends from just inside the event horizon to a radius of twenty gravitational radii and is broken into a statically refined grid with higher resolution close to the hole and around the equatorial plane. The effect of turbulence below the grid scale is not explicitly modeled and is, instead, approximated through numerical dissipation. In `iharm` this dissipation is implicitly modeled through the numerical scheme in what is called an implicit large eddy simulation, or ILES (see, e.g., Grinstein et al., 2007; Miesch et al., 2015). Thus, any calculation of the dissipation will depend on the resolution.

The initial state is based on a Fishbone-Moncrief torus (see Fishbone and Moncrief, 1976). This is an unstable, hydrostatic equilibrium solution. The initial state has this torus seeded with a magnetic field (depending on the magnitude and distribution of this field, the final state could be SANE or MAD) that causes the MRI to break apart the unstable torus and form a turbulent accretion disk. After a transition period where the initial transient damps down, the disk is relatively stable for ∼2000 $\mathrm{GM_{BH}/c^3}$ (∼12 hours for Sgr A*) before too much matter is lost to the hole or outflows at the outer boundary and the evolution becomes unreliable.

This code updates a list of primitive variables: the rest mass density (ρ), internal energy density(u), three components of the fluid three-velocity (v^i), and $^*F^{it}$ (the three components of the magnetic field in the fluid frame). At the beginning of each timestep, the primitive variables (collectively called P) are converted to conserved variables (U) given by equation

---

[1] Source code available at `https://github.com/AFD-Illinois/iharm2d_v3`.

2.16, where $g \equiv \det(g_{\mu\nu})$ and T^{μ}_{ν} is the stress-energy tensor (see, e.g., Misner et al., 1973).

$$\mathrm{U} = \sqrt{-g}\left(\rho u^t, T^t_t, T^t_i, B^i\right). \tag{2.16}$$

These conserved quantities are updated every timestep by adding the local Lax-Friedrichs flux across each face of a given cell. These fluxes, F, on each face are calculated from interpolated (using parabolic reconstruction) primitive variables (calculated at zone centers, just like conserved variables). While the functions U(P) and F(P) are analytic, F(U) and P(U) are not known to be analytic. As the updated U can be computed from F, which is determined by P, the operation P(U) must be performed every timestep. This is accomplished numerically with a secant method using the primitives from the prior timestep as the initial guess. The time steps are determined by a Courant condition; the time step, dt, is always less than the smallest grid crossing time for the fastest plasma wave. The $\vec{\nabla} \cdot \vec{B} = 0$ condition is maintained through each timestep by using a flux-interpolated constrained transport scheme developed by Tóth (2000).

Although these ILES models do not explicitly model dissipation, the dissipation can be expected to occur close to the grid scale, Δx. The effective numerical resistivity is thus $\propto \Delta x$, and, thus, the effective conductivity is $\sigma \propto 1/\Delta x$. The three-current density, j^μ, can be projected into the fluid frame to define $J^\mu = \left(g^\mu_\nu + u^\mu u_\nu\right) j^\nu$. As shown in appendix A, dissipation scales with the three-current density (J^μ) as J^2/σ. In this model, the total dissipation rate is proportional to $\Delta x \int d^3x J^2$. This should converge even if J does not. First, however, the current needs to be calculated from the `iharm` variables. This is accomplished by using the Faraday tensor that `iharm` naturally updates to track magnetic fields and using the relation given by equation 2.17 (see, e.g., Misner et al., 1973; Carroll, 2004).

$$j^\mu = F^{\mu\nu}{}_{;\nu} \tag{2.17}$$

The derivative is evolved numerically. Figure 2.1 shows J^2 throughout the domain for an Orszag-Tang vortex test (see Orszag and Tang, 1979) at a late time for three resolutions. As the resolution increases, the structure of the current changes and the smooth current sheets break into islands and sub-islands, consistent with the plasmoid instability (Loureiro et al., 2007).

Figure 2.2 shows the evolution of $(\Delta x)^{-1} \int J^2 d^3x$ in a superset of the models shown in figure 2.1. At late times, the transient due to the initial conditions has relaxed and an equilibrium is approached. Figure 2.3 shows the convergence of $(\Delta x)^{-1} \int J^2 d^3x$ with resolution. This figure shows that, even though J^2 does not converge, the total dissipation rate does converge. This lends credence to the notion that `iharm` is able to adequately model the resistive dissipation.

Finally, `iharm3d`[2] (see Noble et al., 2009), is used for three-dimensional accretion models. This code is an extension of the original `iharm` code to three spatial dimensions. While the numerical scheme is essentially unchanged except for the addition of an additional spatial dimension and the option to calculate turbulent heating through either of the models proposed by Howes (2010) or Kawazura et al. (2019) (which apportion the viscous heating rate to ions and electrons based on plasma β), the results are noticeably different. First, the additional degree of freedom allows additional features to be observed; for example, a two-dimensional model would not show a hotspot (a relatively small, brightly emitting region) orbiting the central mass. Further, the antidynamo theorem (see Cowling, 1933; Moffatt, 1978) prevents any axisymmetric system from sustaining a magnetic field. There is also the problem that axisymmetric systems eventually evolve into "channel solutions" (see, e.g., Hawley and Balbus, 1992; Goodman and Xu, 1994; Balbus and Hawley, 1998) where two streams of radially flowing fluid (one ingoing and one outgoing) dominate the flow. The third spatial dimension solves these issues by allowing the channels to become unstable and break up.

---

[2] Source code available at `https://github.com/AFD-Illinois/iharm3d`.

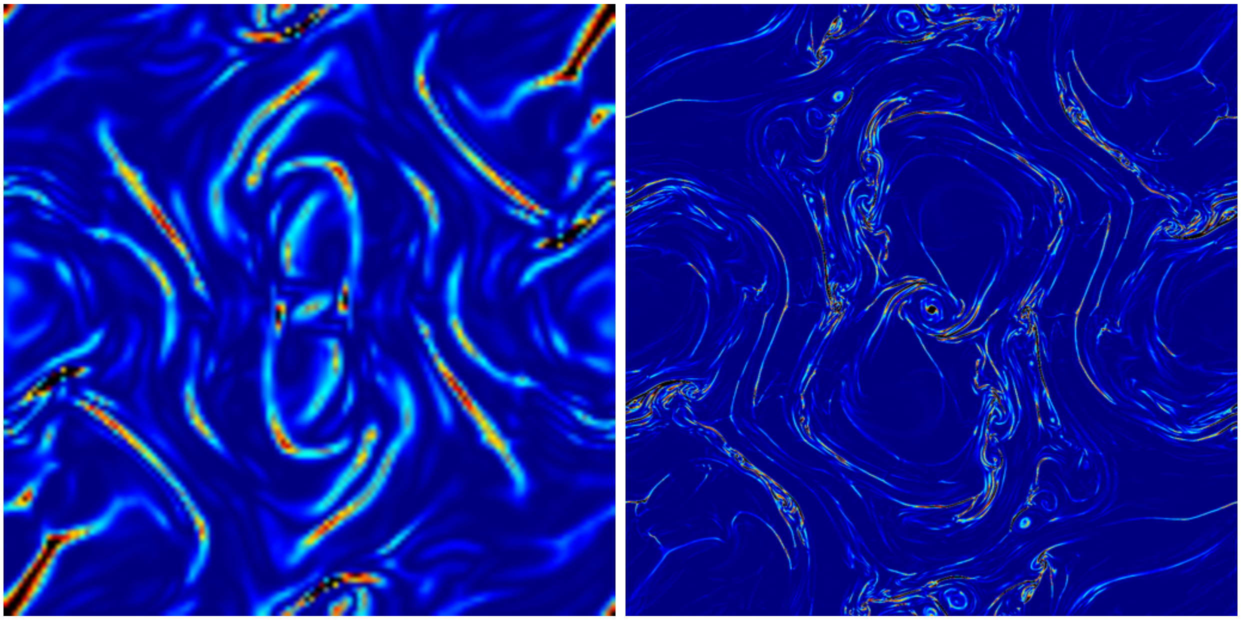

(a) 128^2 resolution. (b) 1024^2 resolution.

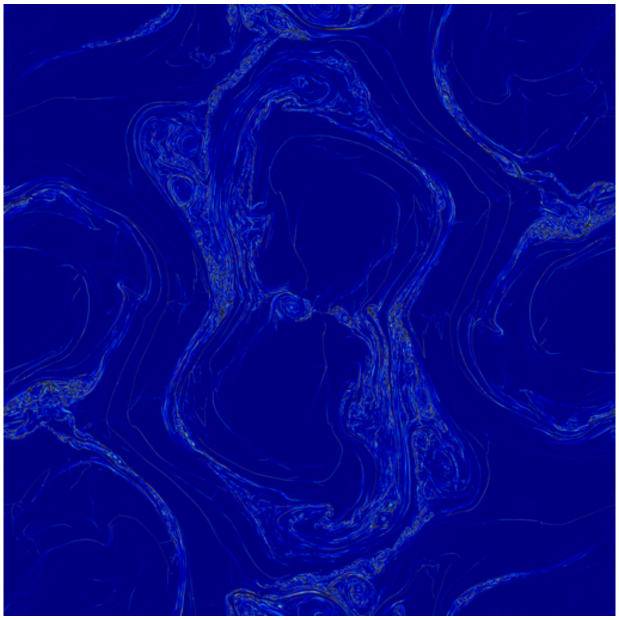

(c) 8192^2 resolution.

Figure 2.1: Snapshots of the square of the current density, J^2, for the Orszag-Tang vortex simulated using `iharm` at three different resolutions. All snapshots are from the same time. The current sheets break into turbulent substructure with increasing resolution. The evolution of $\int J^2 d^2x$ over the domain for these resolutions (as well as several intermediate resolutions) are shown in figure 2.2. The convergence of the integrated square of the current density is given by figure 2.3.

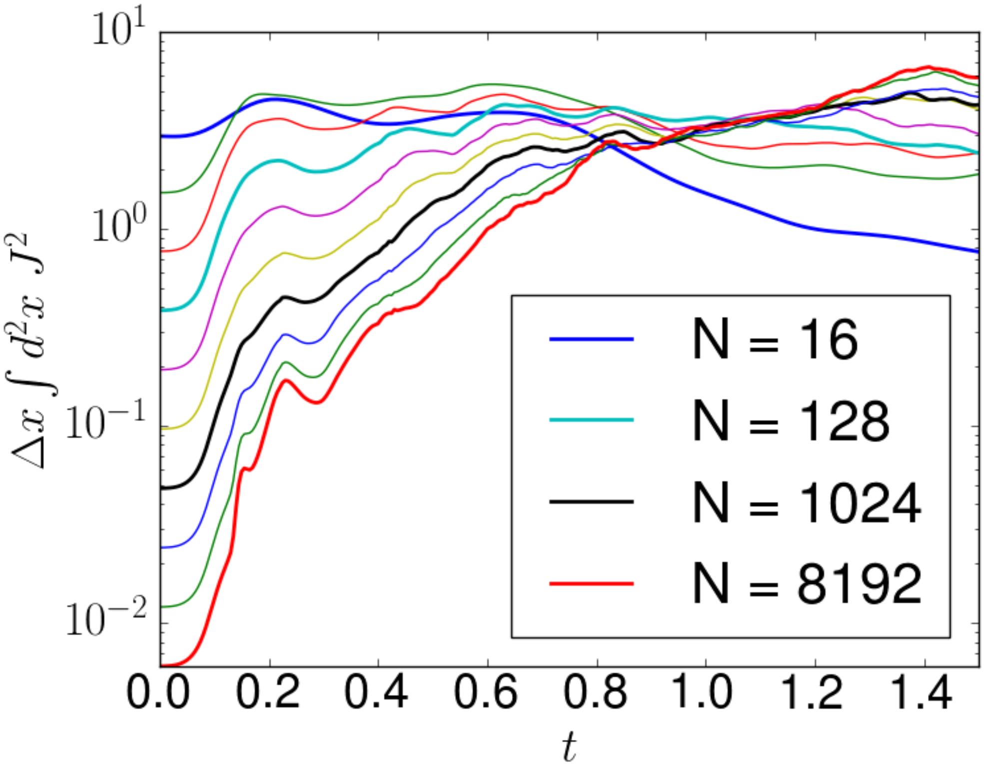

Figure 2.2: Evolution of $\frac{1}{N}J^2$ (i.e., the resistive heating rate) for various resolutions of an Orszag-Tang vortex test in `iharm`. The convergence with resolution is shown in figure 2.3.

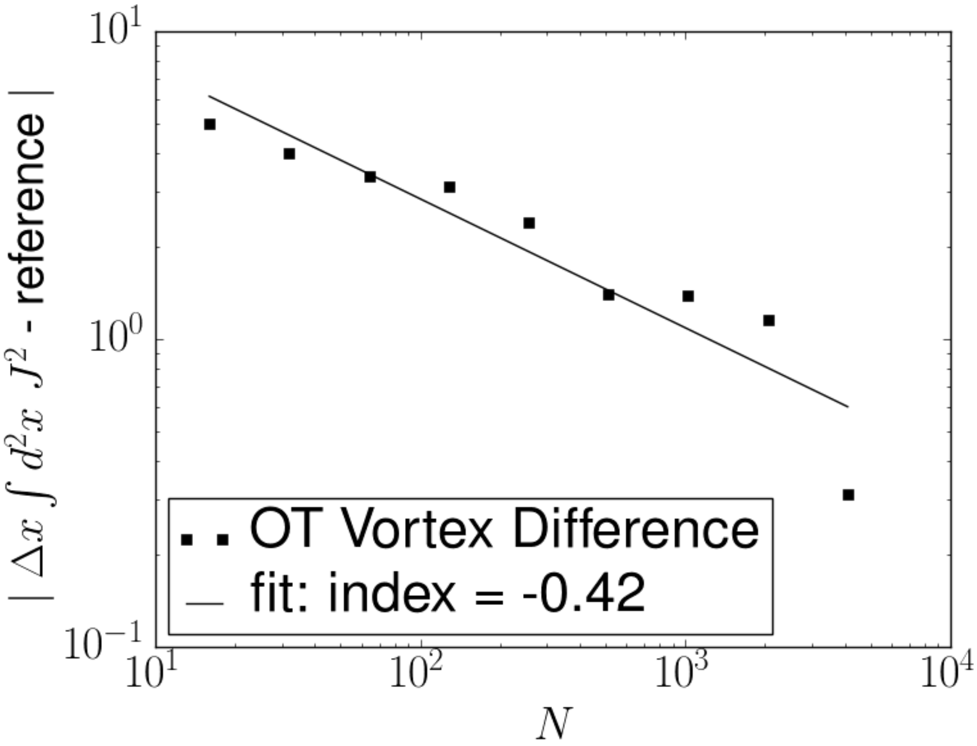

Figure 2.3: Convergence of $(N)^{-1}\int J^2 d^3x$ for N^2 resolution, relative to the highest resolution (N=8192).

2.2 Radiative Transfer

The results of GRMHD simulations (the values of the fluid variables at grid points around the black hole) are not directly comparable to observations. To compare fluid models to observations, simulated fluid data must be translated into simulated electromagnetic signals available to observers on Earth. The method of doing so is called radiative transfer.

The basic (without polarization or scattering) equation of radiative transfer (see Rybicki and Lightman, 1986) is given by equation 2.18. In this equation, ds denotes a small segment along the path of a ray of light while I_ν, j_ν, and α_ν are the specific intensity, emissivity, and absorptivity all at frequency ν.

$$\frac{dI_\nu}{ds} = j_\nu - \alpha_\nu I_\nu \tag{2.18}$$

In the region around a black hole, relativistic effects need to be accounted for. The covariant form of equation 2.18 can be found by first remembering that I_ν/ν^3 is an invariant (see, e.g., Misner et al., 1973). After making the appropriate substitutions for I_ν, clearly j_ν/ν^2 must be the invariant emissivity and $\alpha_\nu \nu$ must be the invariant absorptivity. Thus, the covariant radiative transfer equation, in terms of the affine parameter (λ), is given by equation 2.19.

$$\frac{\mathrm{d}}{\mathrm{d}\lambda}\left(\frac{I_\nu}{\nu^3}\right) = \left(\frac{j_\nu}{\nu^2}\right) - (\alpha_\nu \nu)\left(\frac{I_\nu}{\nu^3}\right). \tag{2.19}$$

The values of j_ν, and α_ν depend on the material that the ray is passing through. In Sgr A*, the synchrotron process is dominant for mm and NIR radiation (Yuan and Narayan, 2014). Synchrotron radiation, also called magnetobremsstrahlung, is the relativistic form of gyro or cyclotron radiation. It is caused by charged particles (almost exclusively electrons, due to their low mass) rapidly circling magnetic field lines at close to the speed of light.

The values for emissivity, j_ν, and absorptivity, α_ν, will depend on the distribution function of the electrons. The forms of the emissivity and absorptivity for the thermal (Maxwell-Jüttner) and nonthermal (in this case, κ) distribution functions (see equations 1.4 and 1.5 for the distribution functions) are given in Pandya et al. (2016). In both cases, the absorptivity and emissivity are dependent on the electron number density ($\mathrm{n_e}$), electron temperature (Θ_e, or w for the κ distribution), magnetic field strength (B), and the angle between the emission direction and magnetic field (θ).

Electrons in the tail of the κ distribution dominate emission in the NIR region and, as such, the slope of the tail can be constrained by the slope of the spectral energy density (SED) in the NIR region. Synchrotron emission due to a power law distribution with index p ($f(\gamma) \propto \gamma^{-p}$) of electrons results in an emissivity of $j_\nu \propto \nu^{-(p-1)/2}$. Therefore, in an optically thin system (in the models described here, at 2.2μm, the optical depth is $\tau < 10^{-8}$), $\nu L_\nu \propto \nu^{(2-\kappa/2)}$. Thus, for a source with $\nu L_\nu \sim \nu^\alpha$,

$$\kappa = 4 - 2\alpha. \tag{2.20}$$

As mentioned in chapter 1.2.3, the observed slope of Sgr A* in the NIR is $\alpha = 0.4$. This results in a value of κ=3.2, which is used throughout the work presented here.

2.2.1 `ibothros` and `ipole`

Radiative transfer is calculated by two codes in this work. The first is `ibothros`[3] (Noble et al., 2007). This code takes as input the plasma data produced by `iharm` and outputs synthetic radiation data that can be compared to observations (e.g., images, light curves, and spectra). It does so by creating an image from an array of pixels. A light curve is created by making many images over a specified time range and summing the flux through all pixels

---

[3] Source code available at `https://github.com/AFD-Illinois/ibothros2d`.

in each image; spectra are produced in a similar manner, but with images produced over a range of frequencies. For each pixel in an image, a null geodesic is numerically calculated corresponding to a light ray incident on a "camera" at a specified inclination angle and (large) radius. The geodesic is found by numerical integration of equations 2.21 and 2.22, where x^μ is the location on the geodesic, k^μ is the tangent vector along the geodesic at that point, $\Gamma^\alpha_{\mu\beta}$ is a connection coefficient, and λ is an affine parameter.

$$\frac{\mathrm{d}x^\mu}{\mathrm{d}\lambda} = k^\mu \tag{2.21}$$

$$\frac{\mathrm{d}k_\mu}{\mathrm{d}\lambda} = -\Gamma^\alpha_{\mu\beta} k_\alpha k^\beta, \tag{2.22}$$

Starting on the far end of this geodesic (either the surface of the black hole or the outer boundary of the `iharm` domain), equation 2.19 is numerically solved until the "camera" is reached and an intensity is recorded for that pixel. The step size for this integration is set adaptively, with smaller step sized used in regions with large emissivities or absorptivities. The step size is further constrained such that no step size is larger than the `iharm` grid size; this ensures sufficient sampling of the fluid. At every step, a bilinear interpolation of the `iharm` variables is used to calculate the local fluid velocity, magnetic field, electron number density, number density of nonthermal electrons (this is model specific; see chapter 3), and electron temperature. In the work presented here, the electron temperature is one third of the proton temperature, calculated from `iharm` variables, due to the assumption that lighter electrons cool more rapidly and because this temperature ratio produces mm results consistent with observations; see Mościbrodzka et al. (2009). With these variables, the local emissivity and absorptivity are calculated by taking a weighted average of the the thermal and nonthermal emissivity and absorptivity.

The second radiative transfer code used in this work is `ipole`[4] (Mościbrodzka and Gammie, 2018), which is used for all of the `iharm3d` models. It functions similarly to `ibothros` but with added capabilities. The difference which is most important for this work is in the electron thermodynamics. While `ibothros` uses a constant temperature ratio to connect the ions and electrons, `ipole` uses a more complicated model based on the local plasma β (the ratio of gas pressure to magnetic pressure). Equation 2.23 gives the proton to electron temperature ratio, T_p/T_e, in terms of plasma β (the ratio of gas pressure to magnetic pressure, $\beta = P/(B^2/8\pi)$), and the model parameters for the high and low β limits of the temperature ratio, r_{high} (in this work, this can range from about one to about one hundred) and r_{low} (which is always set to one, here), respectively.

$$T_p/T_e = \frac{r_{low} + \beta^2 r_{high}}{1 + \beta^2} \tag{2.23}$$

Alternatively, `ipole` can calculate electron temperatures by using either of the turbulent heating methods developed by Howes (2010) or Kawazura et al. (2019), both of which are implemented in `iharm3d`.

---

[4] Source code available at `https://github.com/AFD-Illinois/ipole`.

3 Axisymmetric Results

Original publication: Petersen, Eric and Gammie, Charles, *Non-thermal models for infrared flares from Sgr A**, MNRAS, vol. 494, pp. 5923-5935.

Axisymmetric GRMHD simulations are less computationally expensive than three dimensional GRMHD simulations. Thus, it is reasonable to start with a two dimensional model before moving on to the more expensive three dimensional ones. This approach can also provide guidance when designing the methods to be used for the 3D models. This chapter will explore three methods of adding a nonthermal component to the distribution function; one of these models (model C) will then form the basis for work in chapters 4–5. Table 3.2 provides a summary of the parameters used in and results of the axisymmetric models. All models presented here use an adiabatic index γ=13/9.

3.1 Axisymmetric Models

These models are used to assign a number density of electrons in the κ distribution, $n_{e,NT}$, throughout the spatial and temporal extent of a GRMHD simulation.

Model A assumes that all of the electrons are thermal and, thus, sets $n_{e,NT}=0$. This is useful to compare to previous models and also to discern the effect of the nonthermal portion of the other models. Model B places a constant fraction of electrons into the nonthermal distribution. This is also useful for comparison to prior work (see, e.g., Özel et al., 2000; Yuan et al., 2003b; Chan et al., 2009).

Model C ties the number density of the nonthermal electrons for reconnection by setting $n_{e,NT} \propto J^2$, where J is the magnitude of the three-current density measured in the frame of the plasma. This model is physically motivated by the results discussed in chapter 1.3, but less nuanced than model D (discussed below). It is also useful because it is less computationally expensive than model D.

Model D is the only model to require a modification to the GRMHD scheme (in this case, `iharm`); the previous models were able to confine all references to nonthermal electrons to the cheaper radiative transfer calculation (performed, in this case, by `ibothros`). Model D allocates electrons to the κ distribution with a rate density that is proportional to J^2. It then allows the nonthermal electrons to be advected with the bulk flow of the fluid. Finally, it permits them to cool, a process that is modeled here by returning electrons to the thermal part of the distribution function. Model C is the limit of model D with the cooling time set to zero.

In model D, the nonthermal electron number density evolves according to

$$\frac{\mathrm{d}n_{e,NT}}{\mathrm{d}\tau} = \eta\,\Omega\,(r)\,(n_{e,tot} - n_{e,NT})\,\frac{J^2}{J_0^2} - \frac{n_{e,NT}}{\tau_{cool}}. \tag{3.1}$$

Here, $\mathrm{d}/\mathrm{d}\tau$ is a Lagrangian derivative (the rate of change in the plasma frame), $\mathrm{n_{e,tot}}$ is the number density of all electrons, $\mathrm{n_{e,NT}}$ is the number density of nonthermal electrons, $\Omega(r)$ is a characteristic frequency set to be the local Keplerian orbital frequency ($(GM/r^3)^{1/2}$), J^2 is the square of the local 3-current density, η is a dimensionless parameter that controls the efficiency with which currents accelerate electrons into the nonthermal distribution function, $\mathrm{J_0}$ is a characteristic 3-current density, and τ_{cool} is a characteristic cooling time for synchrotron radiation.

In a nonrelativistic setting $\vec{J} = c\vec{\nabla} \times \vec{B}/(4\pi)$, so $\mathrm{J}^2 \sim \mathrm{c}^2\mathrm{B}^2/(16\pi^2\mathrm{L}^2)$, where L is a characteristic length scale which is set to r here. The magnetic pressure, $\mathrm{B}^2/8\pi$, is replaced by the (assumed to be similar) gas pressure p. With these substitutions, and dropping factors of order unity, $\mathrm{J}_0^2 \equiv \frac{\mathrm{c}^2\mathrm{P}}{\mathrm{r}^2}$.

The synchrotron cooling time (see e.g., Padmanabhan, 2000) depends on the Lorentz factor (γ) and B:

$$t_{cool,s} = \frac{9}{4}\frac{m_e^3 c^5}{e^4}\frac{1}{\gamma B^2}. \tag{3.2}$$

This, along with various forms of heating, are used by Ryan et al. (2018) and Ryan et al. (2019) for electrons confined to a thermal distribution function. Incorporating cooling into the nonthermal model would be difficult (though, see Chael et al., 2017, for a model that does cool nonthermal electrons to a thermal distribution, but with a less physically motivated electron acceleration model) because it would require evolving a dynamic distribution function (Chael et al., 2017, accomplishes this by breaking the distribution into bins) instead of using a constant form for the nonthermal electron distribution function (the κ distribution). Instead, a simplified model is adopted here in which cooling is modeled by transferring electrons from the nonthermal component to the thermal component of the distribution function on a timescale $\tau_{\rm cool}$. An estimate for $\tau_{\rm cool}$ can be obtained by applying equation 3.2 to electrons with a Lorentz factor of $\sim 10^4$ (appropriate for 2.2 μm emission) in a magnetic field that is typical for models of Sgr A* (about 30G). Doing so gives $\tau_{\rm cool} \approx$ 200 s $\approx$ 10 $\rm GM_{BH}/c^3$ for $\rm M_{BH} = 4 \times 10^6\ M_{\odot}$.

In the absence of cooling and acceleration, the nonthermal electrons are assumed to be advected with the flow and, therefore, obey a continuity equation $(\rm n_{e,NT}u^{\mu})_{;\mu} = 0$, where $\rm u^{\mu}$ is the plasma four-velocity. For a summary of the model parameters and their observational constraints, see table 3.1. For a brief discussion on the effects of the parameters from model D (η, $\tau_{\rm cool}$ as well as κ), see appendix B.

3.2 $\rm J^2$ Distribution

Figures 3.1 (covering the full simulation domain) and 3.2 (focusing on the inner region of the disk) show the simulated spatial distribution of $\rm J^2$ during a flare ($\rm t{=}550GM_{BH}/c^3$) and during quiescence ($\rm t{=}1700GM_{BH}/c^3$). The total squared current ($\rm J^2$ integrated over

Symbol	Description	Observational Constraint
T_p/T_e	ion-electron temperature ratio	mean mm flux
$\mathcal{M}$	mass of disk	mean mm flux/image size
i	viewing angle	mm image size
κ	NT distribution parameter	NIR spectral index
η	NT injection efficiency	mean NIR flux
τ_{cool}	nonthermal e^- cooling time	mean NIR flux
C	constant in $n_{e,NT} = Cn_{e,tot}J^2/J_0^2$	mean NIR flux
NT_{frac}	constant ratio $n_{e,NT}/n_{e,tot}$	mean NIR flux

Table 3.1: Summary of the model parameters (see chapters 1.3.1 and 3.1) and the observations that constrain them (see chapter 1.2).

the domain) is ten times larger during the flare than during quiescence. There are multiple current sheets within the ISCO radius and near (but not in) the midplane. During quiescent periods, the current tends to be further out and more diffuse.

Figure 3.3 shows the relationship between current density and radius during the flare and during quiescence. Current densities are larger near the midplane and at low radius. This is partially because current densities are larger in small zones and the grid refinement focuses resolution in these areas.

3.3 230GHz Images and Light Curves

The simulated mm wavelength outputs of the models of chapter 3.1 can be compared to the observational constraints listed in chapter 1.2.2. Figure 3.4 shows a representative image of the inner 35 $\mathrm{GM_{BH}/c^2}$ (∼1.6 AU or ∼200 μas). The snapshot was taken at $\mathrm{t=1000GM_{BH}/c^3}$ (∼5.5 hours into the simulation) and uses model D (the acceleration and cooling model). The elliptical Gaussian fit is given by the solid white ellipse while the

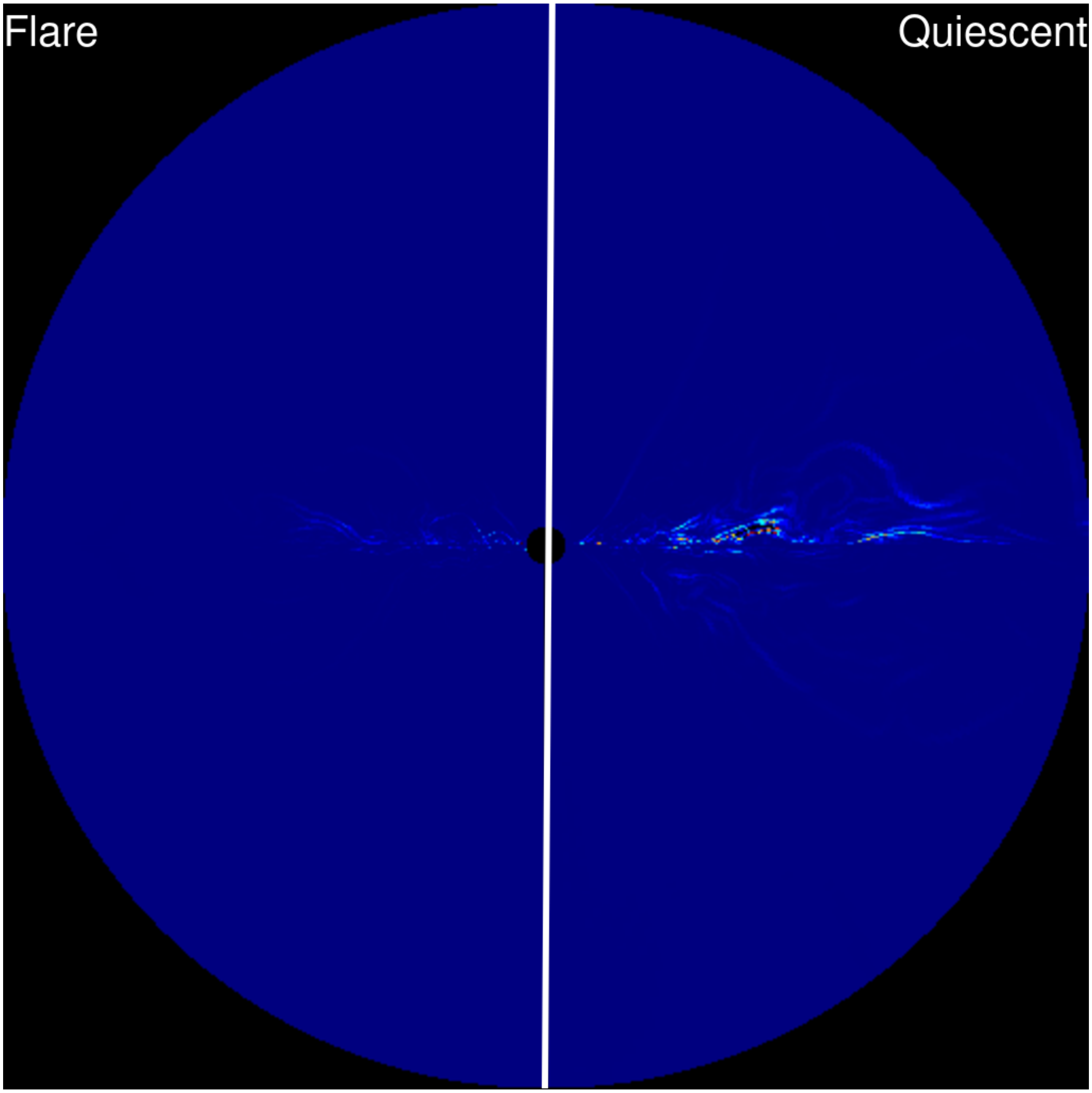

Figure 3.1: Spatial distributions of J^2 for the entire simulation domain (that is, out to $r=40GM_{BH}/c^2$), *left:* during a flare ($t=550GM_{BH}/c^3$) and *right:* during a quiescent period ($t=1700GM_{BH}/c^3$). Note that the color scales are different for each half of the image; the square of the current density integrated over the entire domain is a factor of ten larger during the flare than it is during quiescence.

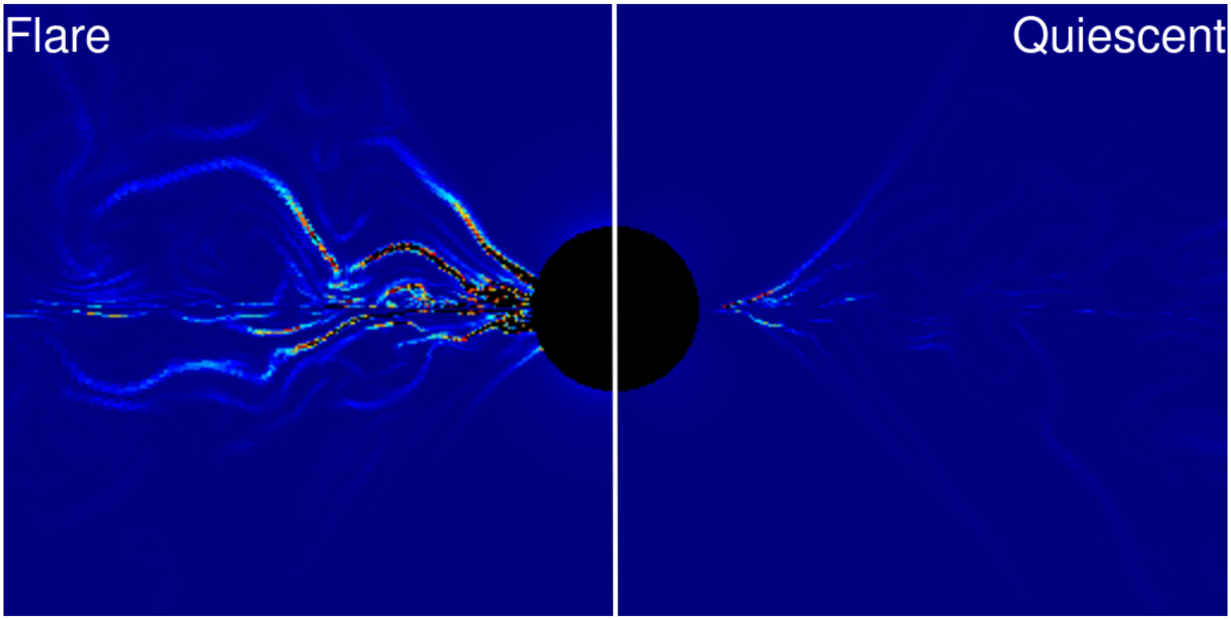

Figure 3.2: Maps of J^2 within $5GM_{BH}/c^2$ of the midplane and out to $r=10GM_{BH}/c^2$, *left:* during a flare ($t=550GM_{BH}/c^3$) and *right:* during a quiescent period ($t=1700GM_{BH}/c^3$). Note that the color scales are different for each half of the image; the square of the current density integrated over the entire domain is a factor of ten larger during the flare than it is during quiescence.

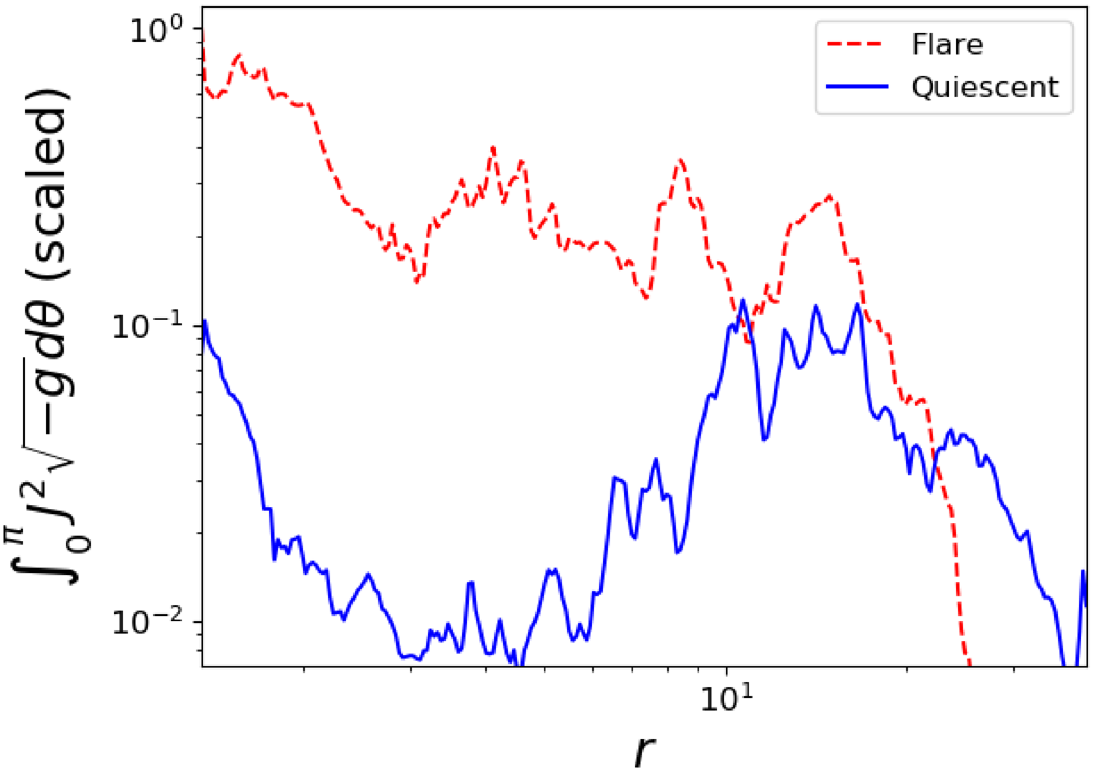

Figure 3.3: Distribution of current density integrated over solid angle ($\int J^2 d\theta$) versus radius. Currents are concentrated close to the black hole during the flare but are further out during quiescence. In the inner region, the square of the current density is around ten times higher during a flare than it is during the quiescent period.

observed size of 37μas (given by Doeleman et al., 2008, and which was the target of the fit) is traced by the dashed green circle. The full width at half maximum (FWHM) of the fit varies by ~15% during the course of the simulation, but this particular measurement has a size ratio (compared to the observation) of 1.0. For all four models, the FWHM is between 35μas and 37μas and the mass of the simulated disk ($\mathcal{M}$), after fitting for mm size and mean flux density, was $\dot{\mathrm{M}} \approx 2.3 \times 10^{-9}\ \mathrm{M}_{\odot}\mathrm{yr}^{-1} \approx 2.6 \times 10^{-8}\dot{\mathrm{M}}_{\mathrm{Edd}}$, which is within the range ($2 \times 10^{-9}\ \mathrm{M}_{\odot}\mathrm{yr}^{-1} < \dot{\mathrm{M}} < 2 \times 10^{-7}\ \mathrm{M}_{\odot}\mathrm{yr}^{-1}$ or $2 \times 10^{-8}\dot{\mathrm{M}}_{\mathrm{Edd}} < \dot{\mathrm{M}} < 2 \times 10^{-6}\dot{\mathrm{M}}_{\mathrm{Edd}}$) discussed in chapter 1.2.1.

Figure 3.5 compares the simulated flux density from all four models to the observed mean flux of 3.7Jy (taken from Bower et al., 2015). All four models have a mean mm flux density within 15% (0.7σ) of 3.7Jy. The observed mm light curve as well as the model light curves show substantial variability ($\sigma \approx$0.7Jy). The four model light curves are nearly identical; this indicates that the inclusion of a κ-law component to the total electron distribution function has little effect on the emission at mm wavelengths.

3.4 Spectral Energy Densities

The SEDs for all four models are shown in figures 3.6 (during a flare) and 3.7 (in quiescence). In both figures, the computed SEDs are compared to the observed mm luminosity and NIR luminosity in both the flaring and non-flaring states. A line indicating the observed spectral slope is also shown. All observations are discussed in chapter 1.2. The purely thermal model produces negative spectral slopes while the nonthermal models produce slopes within 10% of 0.4 (the observed value, see chapter 1.2.3), as was expected from the choice of κ.

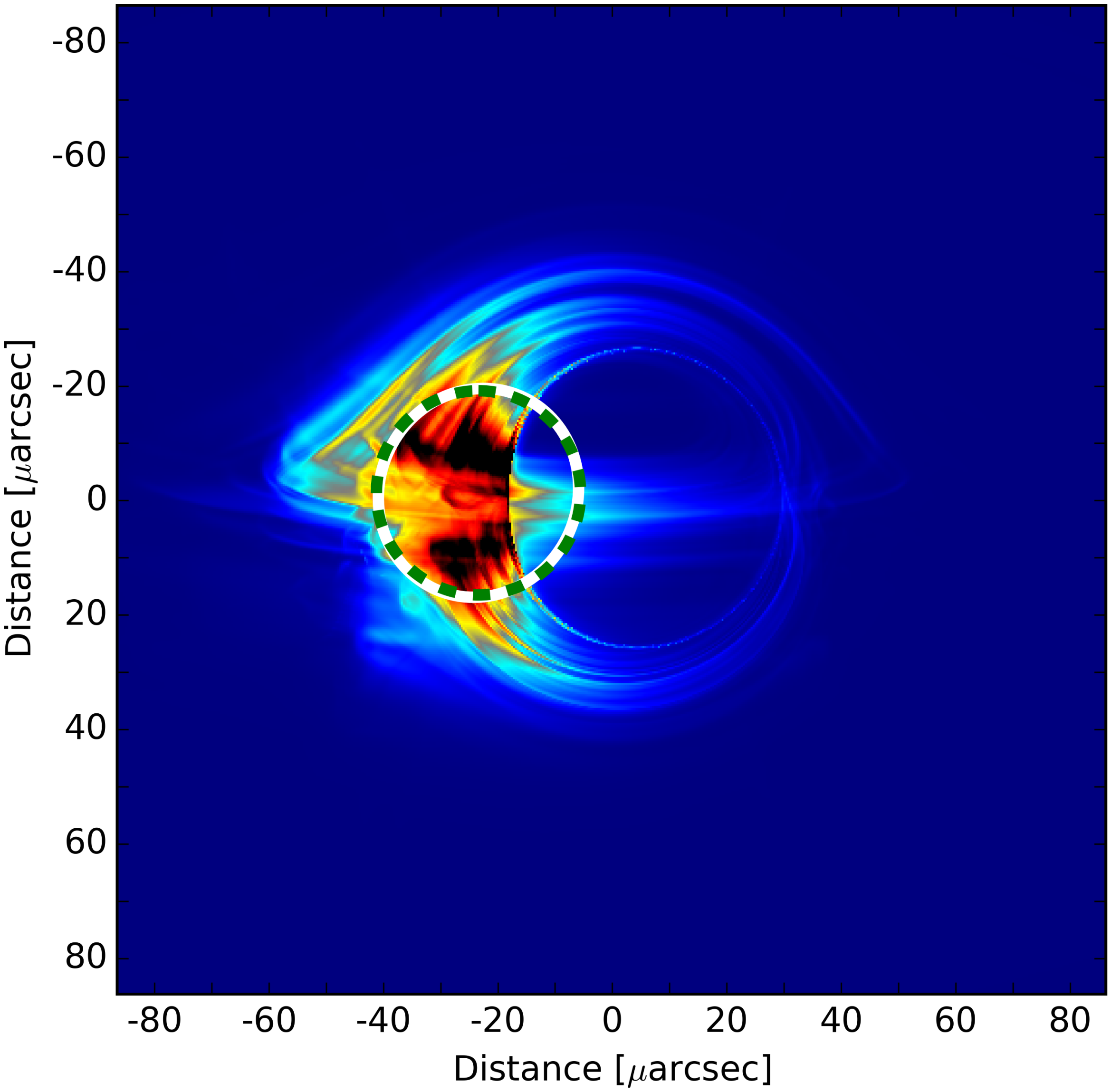

Figure 3.4: A simulated 230GHz image from t=1000GM$_{\mathrm{BH}}$/c^3 (∼5.5 hours) using model D. The (linear) color scale shows brighter regions as black or red and dimmer regions as dark or light blue. The solid white ellipse is a two-dimensional Gaussian fit to the image and the dashed green circle shows the observed image size (FWHM) from Doeleman et al. (2008).

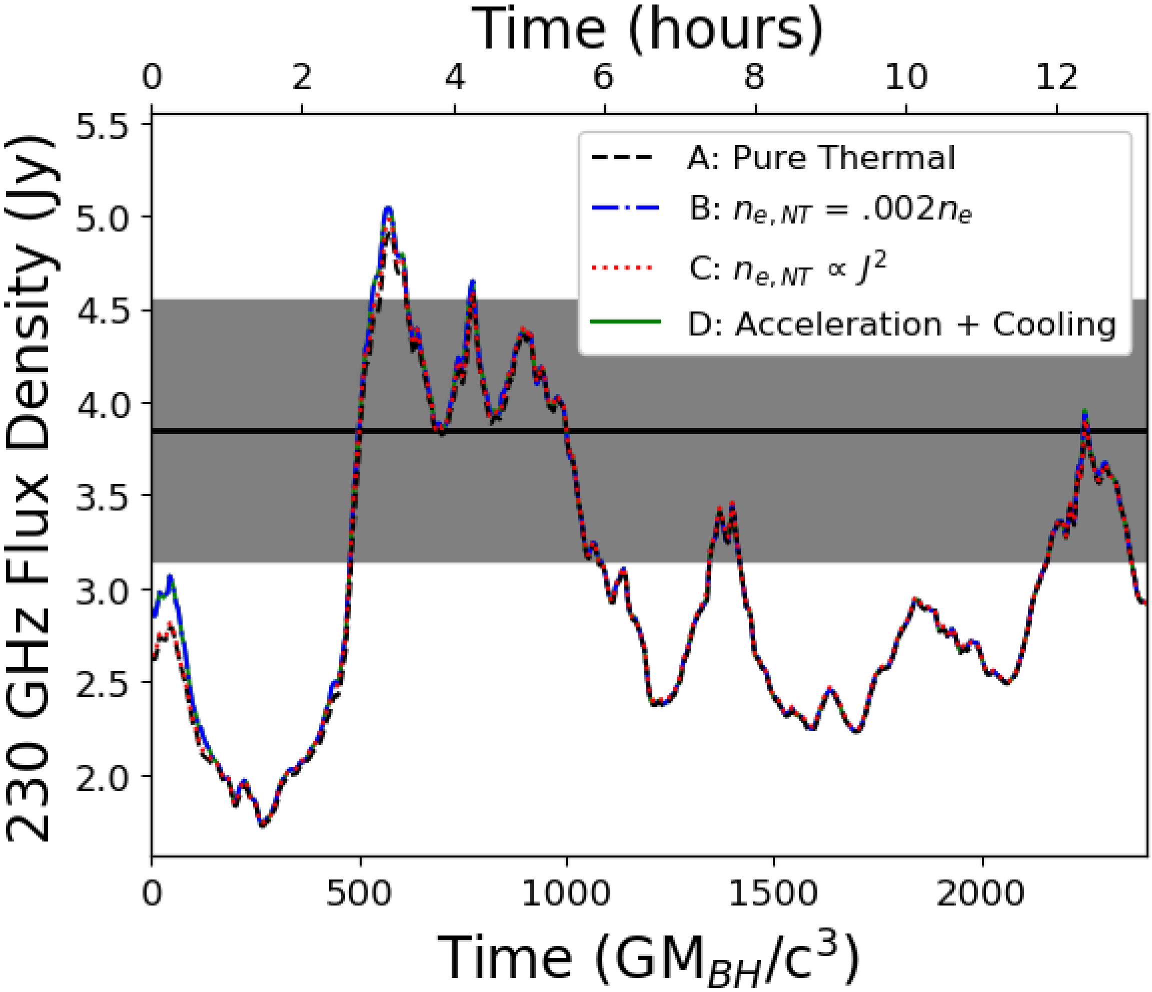

Figure 3.5: light curves for models A–D at 1.3mm compared to the mean observed flux density (Bower et al., 2015). The model light curves match almost exactly, indicating that changes in the nonthermal population have little impact on the 230GHz flux density. The observed mean mm flux density (3.7Jy, compared to 3.2Jy in models A–D) is given by the solid black line and the gray region shows the observed 1σ variability (0.7Jy, which is the same as the variability for the simulation models).

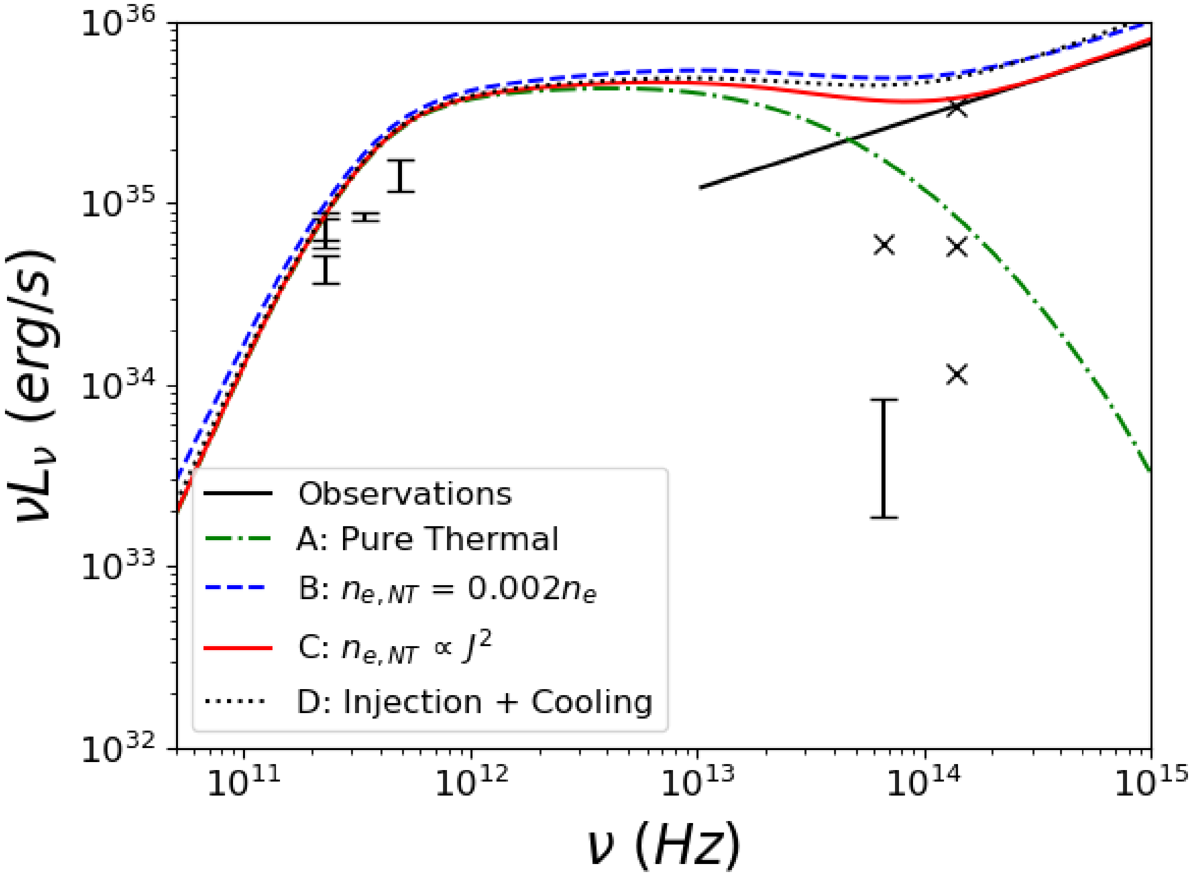

Figure 3.6: Model SEDs at t=550GM$_{\rm BH}$/c^3 (during a flare) compared with observations. Observational data, mm luminosity as well as the flaring/non-flaring luminosity and spectral slope ($\nu L_\nu \propto \nu^{0.4}$), are discussed in chapter 1.2.

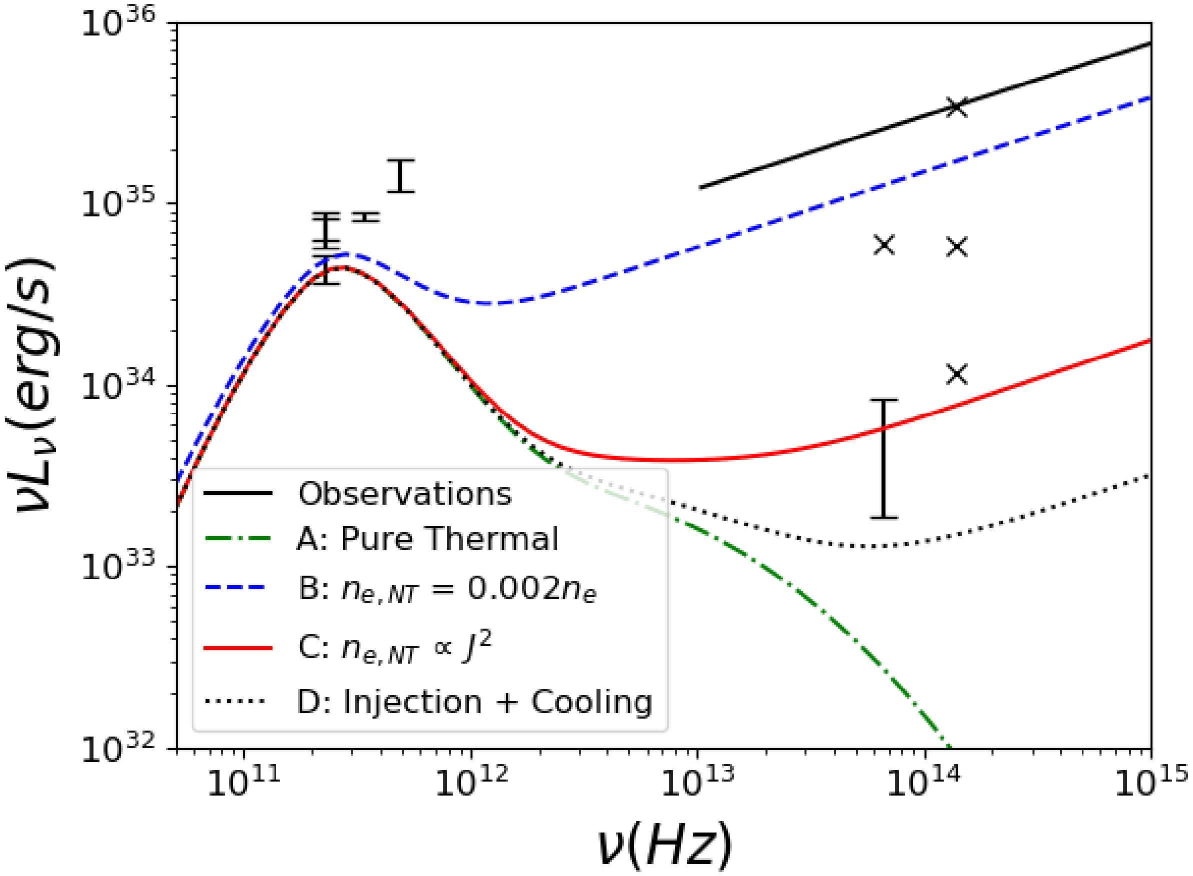

Figure 3.7: Model SEDs at t=1700GM$_{\mathrm{BH}}$/c^3 (during a quiescent period) compared with observations. Observational data, mm luminosity as well as the flaring/non-flaring luminosity and spectral slope ($\nu L_\nu \propto \nu^{0.4}$), are discussed in chapter 1.2.

3.5 2.2μm Light Curves and Motion

Figure 3.8 shows NIR light curves for models A–D. The thermal model (model A) vastly underproduces, compared to observations during a flare, the NIR flux density, with an average of less than 5mJy and very little variation. The nonthermal models produce much higher flux density (peaks of 40mJy, 22mJy, and 25mJy for models B, C, and D, respectively) thus, coming much closer to matching observations from chapter 1.2.3. Not all of these models recreate the observed variability (see figure 3.9 for the flux distribution), however. It is possible to tune model B to either produce a flux density similar to observations in the flaring state (this is shown in figure 3.8) or the correct quiescent flux density. However, model B never matches both flux density in the flaring state and the quiescent flux density with the same parameters. The mean quiescent flux density is computed by averaging from $t=1675GM_{BH}/c^3$ to $t=1725GM_{BH}/c^3$ as this period shows minimal NIR emission or variability. For model B, this mean quiescent flux density is 15mJy while all other models have a mean quiescent flux below 1mJy. In addition to matching the low quiescent flux density, models C and D also show approximately correct flare magnitude (of around 25mJy). In each model, the simulated flare lasts between one and two hours, which is similar to the duration (1–2 hours) of observed flares.

Figure 3.9 shows a histogram of flux density for all two dimensional models compared to the flux distribution found by Dodds-Eden et al. (2011). The thermal model (model A) never produces flux densities in excess of 10 mJy as seen during flares while the constant nonthermal fraction model (model B) never produces variability close to that which is observed. The nonthermal injection models fit the observed flux distribution better, with instantaneous cooling model (model C) producing a slope which is closer to the observed slope than model D, though model D does somewhat better at lower flux densities. None of the models match observed distribution below 3.5 mJy, though this portion is subject

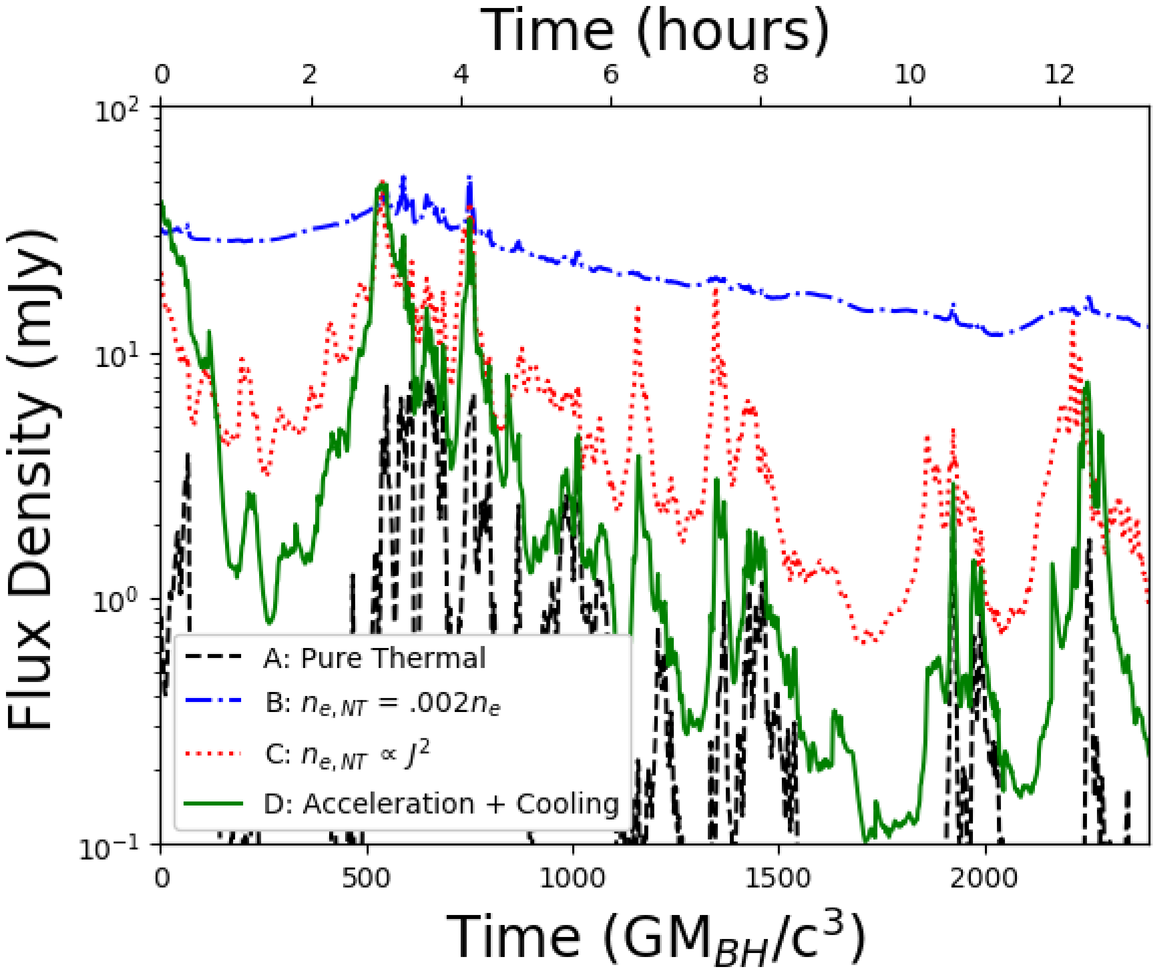

Figure 3.8: 2.2μm light curves for two dimensional models A–D. The purely thermal model (dashed black line, model A) produces too little flux density or variability to match NIR observations. The constant nonthermal number density fraction model (dashed-dotted blue line; model B) can be made to match the flaring flux density, but not the variability. The nonthermal injection models, both with instantaneous cooling (dotted red line; C) and with finite cooling (solid green line; D), do show substantial variability. The flare can be made to match or exceed the observed flare amplitude.

to large observational uncertainties (Dodds-Eden et al., 2011). It should be noted that the statistics for the observations are compiled from many flares while the simulations only have data for a single flare.

Figure 3.10 shows NIR images, for models A and D, during a flare ($t=550GM_{BH}/c^3$). Flaring images are highly variable, but they all show substantial emission from near the midplane within the innermost stable circular orbit (ISCO); this is true for all models that show flares. A similar set of NIR images is shown in figure 3.11, but these images are during quiescence ($t=1700GM_{BH}/c^3$). All nonthermal models show similar behavior, with nearly all of the emission coming from near mid-plane and around or within the ISCO.

Figure 3.12 shows the motion of the NIR image centroid over the course of the axisymmetric simulation. The background image is the same as the central portion of the right image in figure 3.10. The image centroids, calculated for every point with a flux density of more than 5 mJy on the NIR light curve of model D in figure 3.8, are represented by white dots. The centroid location is independent of the 2.2 μm flux density and all but four of the centroids (about 0.3%) lie within 10 μas of the mean position. The centroid has a root mean square deviation of 4.9 μas from its average position. Models B and C have no centroid deviations of more than 5 μas.

In all of the results so far, the disk has been assumed to be viewed nearly edge on (with an inclination angle of 84°). However, GRAVITY finds an inclination angle of $160^\circ \pm 10^\circ$ (Gravity Collaboration et al., 2018). Figure 3.13 shows that the NIR light curve and centroid motion are not strongly dependent on inclination angle (keeping all other parameters constant). The root mean square (RMS) centroid deviation is found by first calculating the mean location of the centroid from each frame of the light curve and then finding the RMS between that mean location and each frame's centroid. This RMS separation is less than the minimum detectable separation for GRAVITY (10 μas) for all inclinations. Further, all inclination angles show similar NIR variability.

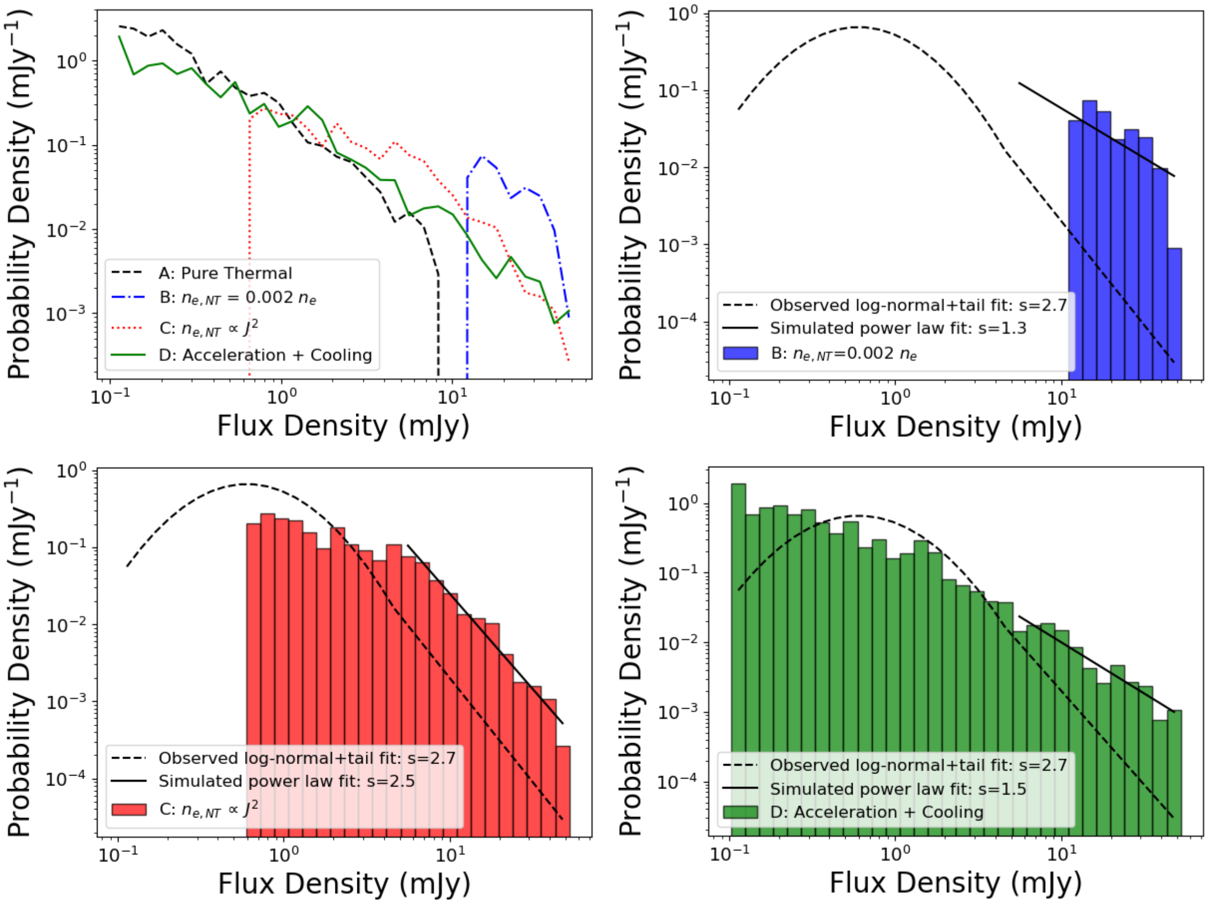

Figure 3.9: *top left:* Line plots of the flux density histograms (representing the fraction of images within each flux density bin) for models A–D. *top right:* Histogram for model B only along with the log-normal+tail fit (dashed line) reported in Dodds-Eden et al. (2011) and a power law fit (solid line) to the simulated tail section (defined as fluxes greater than 5 mJy). *bottom left:* Histogram for model C with the same fit lines. *bottom right:* Histogram for model D with the same fit lines.

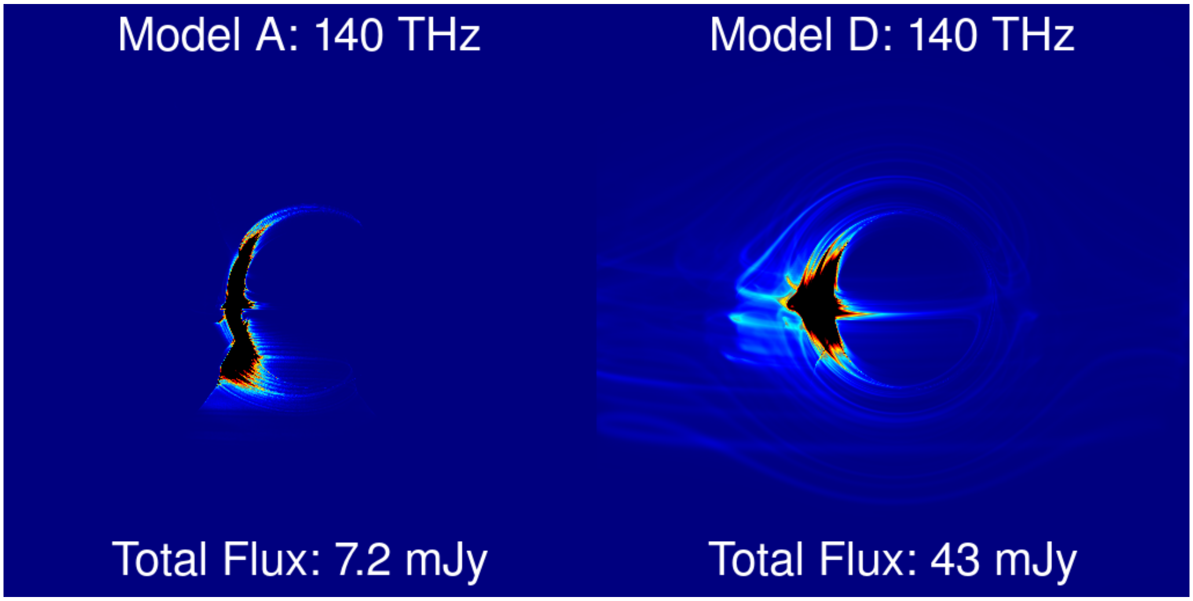

Figure 3.10: 2.2 μm images during a flare (t=550GM$_{\rm BH}$/c^3). *left:* Model A. *right:* Model D. Each image has a separate, linear colormap.

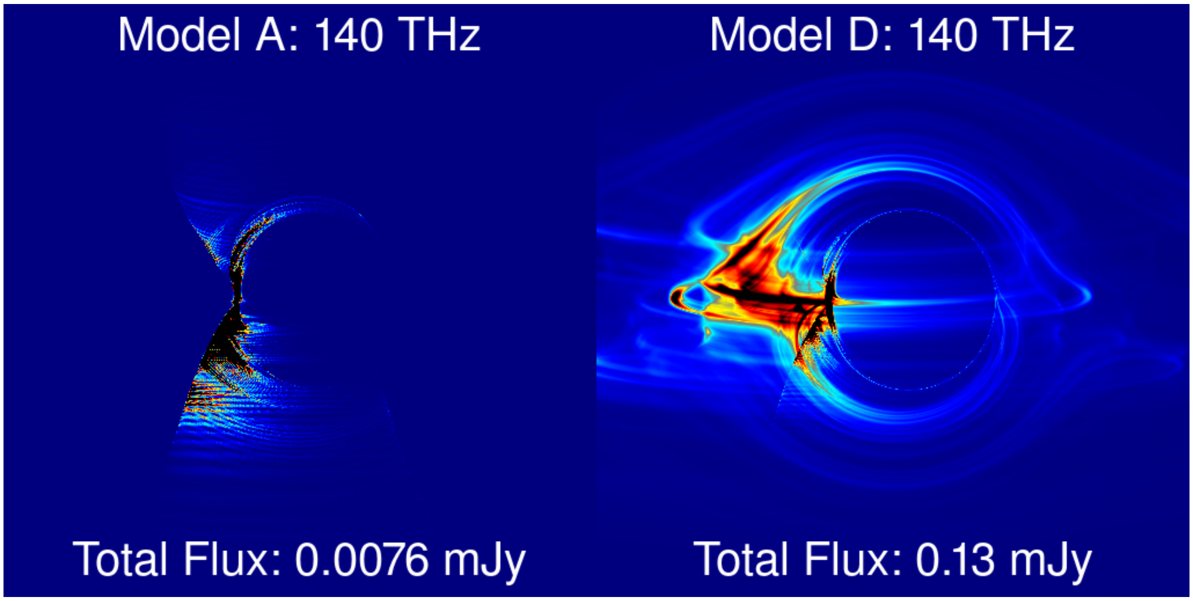

Figure 3.11: 2.2 μm images during quiescence (t=1700GM$_{\rm BH}$/c^3). *left:* Model A. *right:* Model D. Each image has a separate, linear colormap.

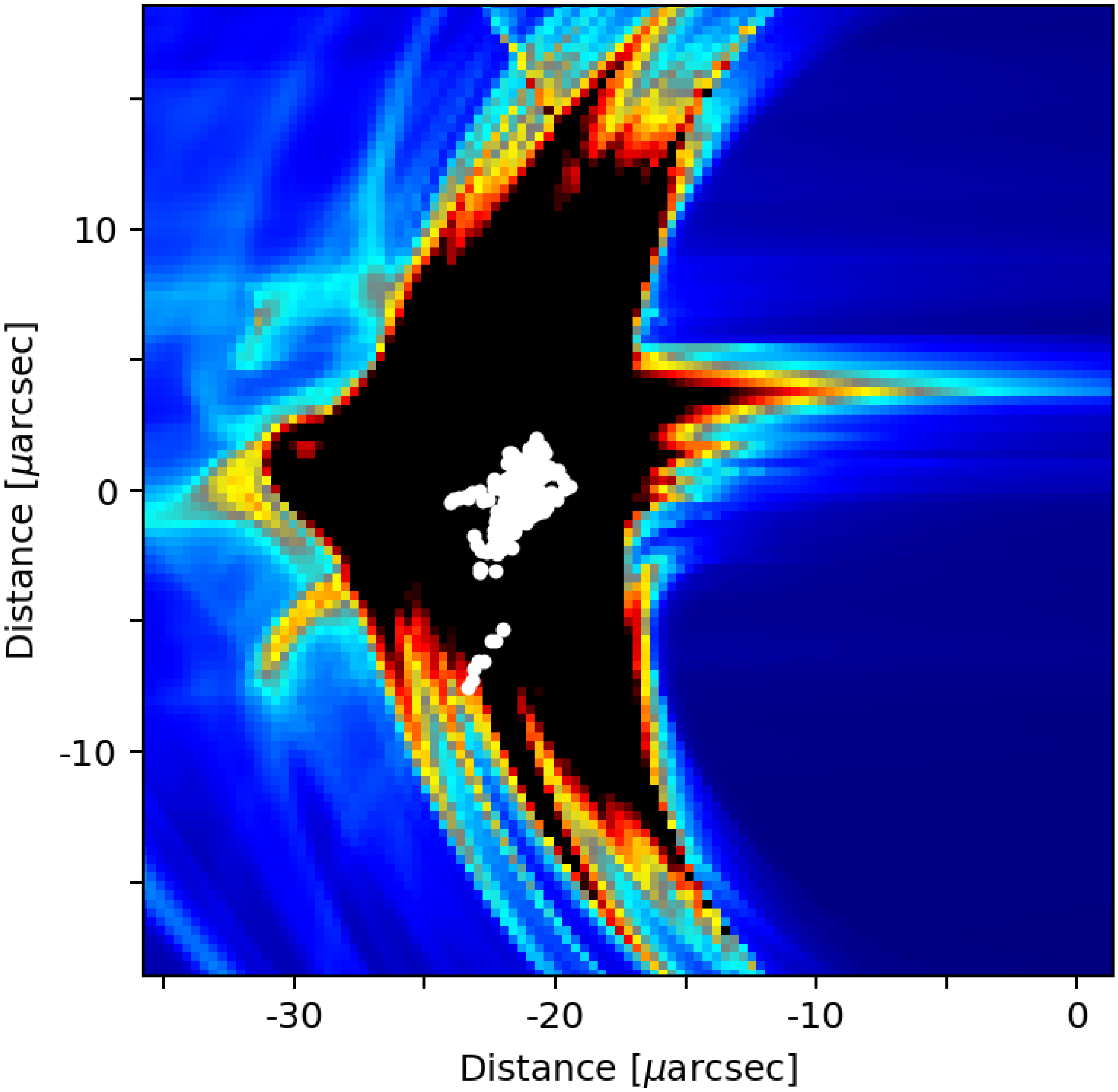

Figure 3.12: The trail of the centroid of 2.2 μm emission overplotted on a background of the central portion of the 2.2 μm image from t=550GM$_{\mathrm{BH}}$/c^3 (see figure 3.10). The white dots correspond to centroid locations when the total flux density was over 5 mJy.

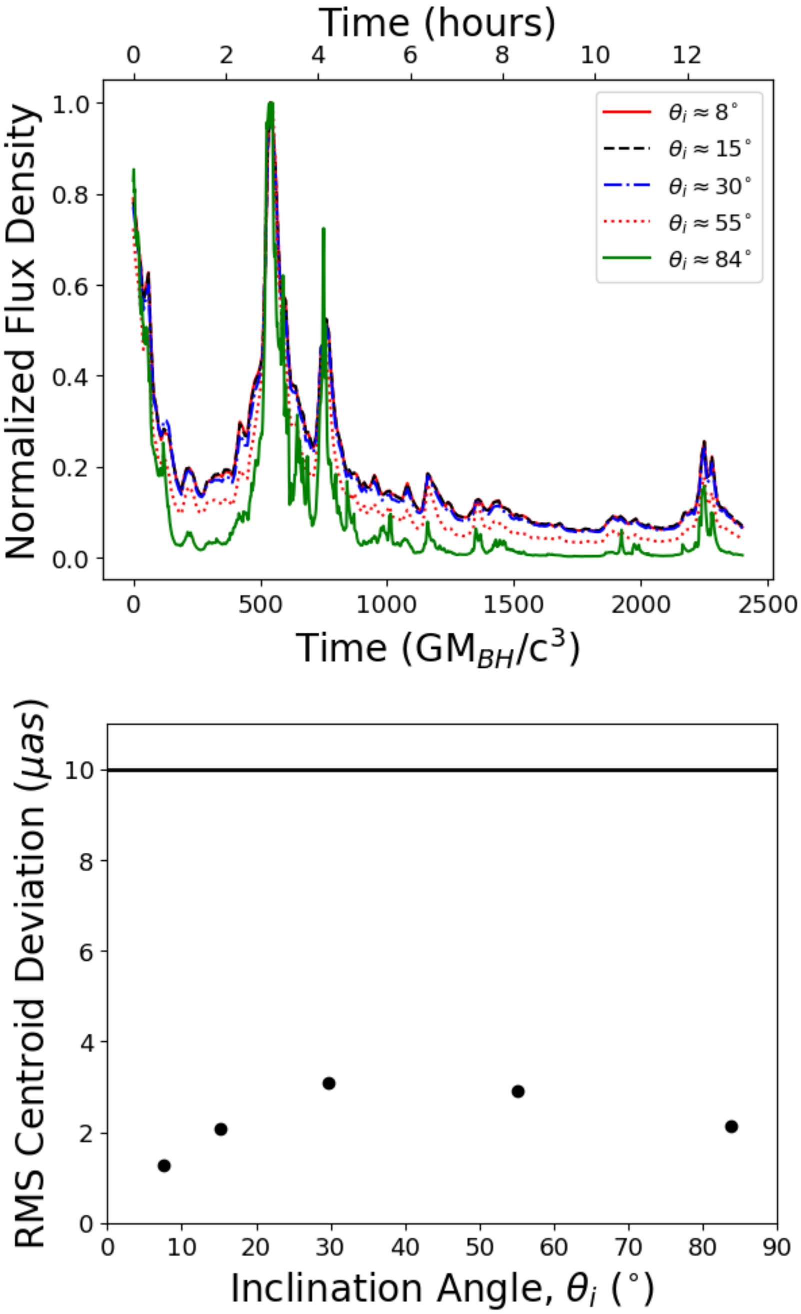

Figure 3.13: *top:* Normalized light curves for various inclination angles (with all other parameters constant). *bottom:* RMS centroid deviation at various inclination angles (points) compared to the precision of GRAVITY astrometry (solid line).

3.6 Summary and Discussion

All models agree with 230GHz observations of Sgr A*'s size and average flux, by construction. The variability of the light curve for all four models is close to the observed variability. The addition of a κ-law component to the electron distribution function in models B,C, and D does not change the SED at $\lambda \approx$1.3 mm.

The fraction of electrons in the nonthermal distribution can be estimated by assuming that the spectral index of α=0.4 is valid for the nonthermal electrons from 230GHz to 140THz and comparing the mean mm flux density to the flaring NIR flux density. In this approximation, a small fraction of nonthermal electrons can account for the nonthermal NIR emission. In model B the nonthermal fraction is <1% and uniform across the model; in models C and D around 10% of the electrons are in the κ distribution in regions of high current density with the rest of the plasma being almost purely thermal.

The nonthermal models (B, C, and D) were able to replicate the 2.2 μm flux during a flare while the purely thermal model (A), predictably, failed to do so. The model with the nonthermal component representing a constant fraction of the total electron number density (model B) showed more NIR emission, but little variability. This is a similar result to the that produced by another constant nonthermal fraction model (Yuan et al., 2003b). The models that inject nonthermal electrons in reconnecting current sheets (C and D) were also able to reproduce the observed variability with one large flaring event of about an hour ($\sim$10 orbital periods at the ISCO) in duration and with a power law tail in the flux distribution at large flux. The power law slopes for models C and D are roughly consistent with the observed flux distribution. The centroid motion of the 2.2 μm images shows no correlation with the 2.2 μm flux density and is too small to be measured by GRAVITY. However, GRAVITY has measured centroid motion of around 150 μas (Gravity Collaboration et al., 2018).

While interesting, these results are of limited value as axisymmetric models can behave differently than three dimensional simulations and there is only one flare being examined, compared to the observed data taken over many years. Further, there is tension with observations regarding the motion of the NIR centroid. An axisymmetric simulation cannot show the azimuthal motion of a fluid element (e.g., one with electrons accelerated by a current sheet) orbiting the black hole. Thus, a major source of motion in the image is absent from two dimensional models. This indicates a need to use much more expensive three dimensional simulations. The cost can be somewhat mitigated by using a version of model C (as opposed to model D), which allows for the use of extant 3D simulations with the nonthermal portion done in post-processing.

	Model A	Model B	Model C	Model D
a	15/16	15/16	15/16	15/16
T_p/T_e	3.0	3.0	3.0	3.0
$\mathcal{M}(10^{19}$ grams)	2.0	2.0	2.0	2.0
i (degrees)	83.8	83.8	83.8	83.8
κ	N/A	3.2	3.2	3.2
NT_{frac}	N/A	2.0×10^{-3}	N/A	N/A
C	N/A	N/A	3.0×10^{-3}	N/A
η	N/A	N/A	N/A	$1/3 \times 10^{-6}$
τ_{cool} (seconds)	N/A	N/A	N/A	200
$\dot{M}$ (10^{-9} $M_\odot yr^{-1}$)	2.3	2.3	2.3	2.3
mean mm flux (Jy)	3.2	3.2	3.2	3.2
s.d. of mm flux (Jy)	0.72	0.74	0.72	0.74
mm image size (μas)	35	36	35	36
quiescent NIR flux (mJy)	0.010	15	0.69	0.12
flaring NIR flux (mJy)	4.5	40	22	25
NIR center max dev. (μas)	16.1	2.13	4.29	22.0
NIR center rms dev. (μas)	3.8	1.0	1.3	2.4
NIR center dev. $>10\mu$as	3.7%	0.0%	0.0%	0.3%
flaring spectral slope	-1.6	0.32	0.37	0.38
quiescent spectral slope	-2.3	0.41	0.42	0.38

Table 3.2: Summary of the parameters and output for axisymmetric models A–D. See chapter 3.1 for an explanation of each model, see table 3.1 for a summary of the model parameters, and see chapters 3.2-3.5 for a description of the results.

4 3D SANE Results

After the previous chapter, the next step is to move on to fully three dimensional simulations. That is what is done here and in chapter 5. This chapter is the most similar to chapter 3, in that the magnetic field is relatively weak; this chapter will continue to describe standard and normal evolution (SANE) models, while chapter 5 covers magnetically arrested disk (MAD) models. SANE models have relatively weak magnetic flux and rapid accretion. The magnetic flux is defined as the surface integral of the magnetic field over a hemisphere of the black hole horizon ($\Phi_{BH} \equiv \int_\theta \int_\phi B^r dA_{\theta\phi}$). For SANE models, the dimensionless flux ($\phi_{BH} \equiv \Phi_{BH}/\sqrt{\dot{M} r_g^2 c}$, where r_g=GM$_{\rm BH}$/c^2) is usually less than 10 (see Tchekhovskoy et al., 2011b; Narayan et al., 2012). They tend to show less short-timescale variability but simulations can show long-term changes as matter from the disk is accreted or carried away in an outflow. This can make long simulations of a steady-state challenging.

Three dimensional models are more expensive than two dimensional models not only because of the greatly increased number of computational zones but also because they can be run to much greater time (t). For models used here, 3D models require two to three orders of magnitude more core-hours to compute than 2D models. In order to cut down on computational expense (without greatly affecting accuracy, see 3), only J^2 injection and instantaneous cooling models (analogous to model C, in chapter 3) will be considered in this chapter. For all models, an adiabatic index of γ=4/3 is used and the accretion rate (controlled by $\mathcal{M}$) is set so that the mean mm flux is close to the observed value; the procedure for this is the same as in chapter 3.

One difference between this chapter and the last chapter is that this chapter will not only examine high spin (a=15/16, as in chapter 3), but also lower spin (a=1/2), non-spinning (a=0), and retrograde (a=-1/2, -15/16) models. Prograde (positive spin) models have the angular momentum of the disk is perfectly aligned with the spin axis of the black hole while retrograde (negative spin) models have them anti-aligned (at large radius; frame dragging ensures that plasma near the event horizon orbits in the spin direction). Misaligned (tilted disk) models are not considered here. All fluid (`iharm3d`) models presented here are run with a resolution of 288×128×128 (for the radial, polar, and azimuthal directions, respectively). Each of these five GRMHD models are coupled with five electron thermodynamics models: a purely thermal electron heating model (with the portion of the turbulent heating assigned to ions/electrons dependent on plasma β, see Kawazura et al. (2019)), and $\mathrm{r_{high}}$ models (see equation 2.23) with nonthermal injection proportional to J^2 and instantaneous cooling and $\mathrm{r_{high}}$ set to 1, 10, 40, or 160. Images are produced for inclination angles of 10°, 30°, 50°, 70°, or 90°, bringing the total number of models examined here to 125. Unless otherwise specified, all images are 80×80 resolution and a field of view of 176μas (or $35\mathrm{GM_{BH}/c^2}$).

4.1 J^2 Distribution

With the dissipation, and the nonthermal contribution to the emission, proportional to J^2 in these models, it is important to know when large currents form within the computational domain. Figure 4.1 shows the evolution of J^2 integrated over the entire computational domain and integrated over only the inner region with $2\mathrm{GM_{BH}/c^2} < \mathrm{r} < 5\mathrm{GM_{BH}/c^2}$ (which produces the majority of the NIR radiation). As dissipation is directly proportional to J^2, this will show when there are the most electrons in the κ distribution and, in principle, when the NIR emission should be greatest.

Large, positive spin models produce both more current and more variability; however, the integrated current never varies by as much as a factor of two — less than the magnitude of the observed NIR flares. Models with no or negative spin will certainly not be able to produce flares by resistive dissipation at the 288×128×128 resolution used here. By focusing on a single constant azimuth slice for the a=15/16 model, as in figure 4.2, a larger range of

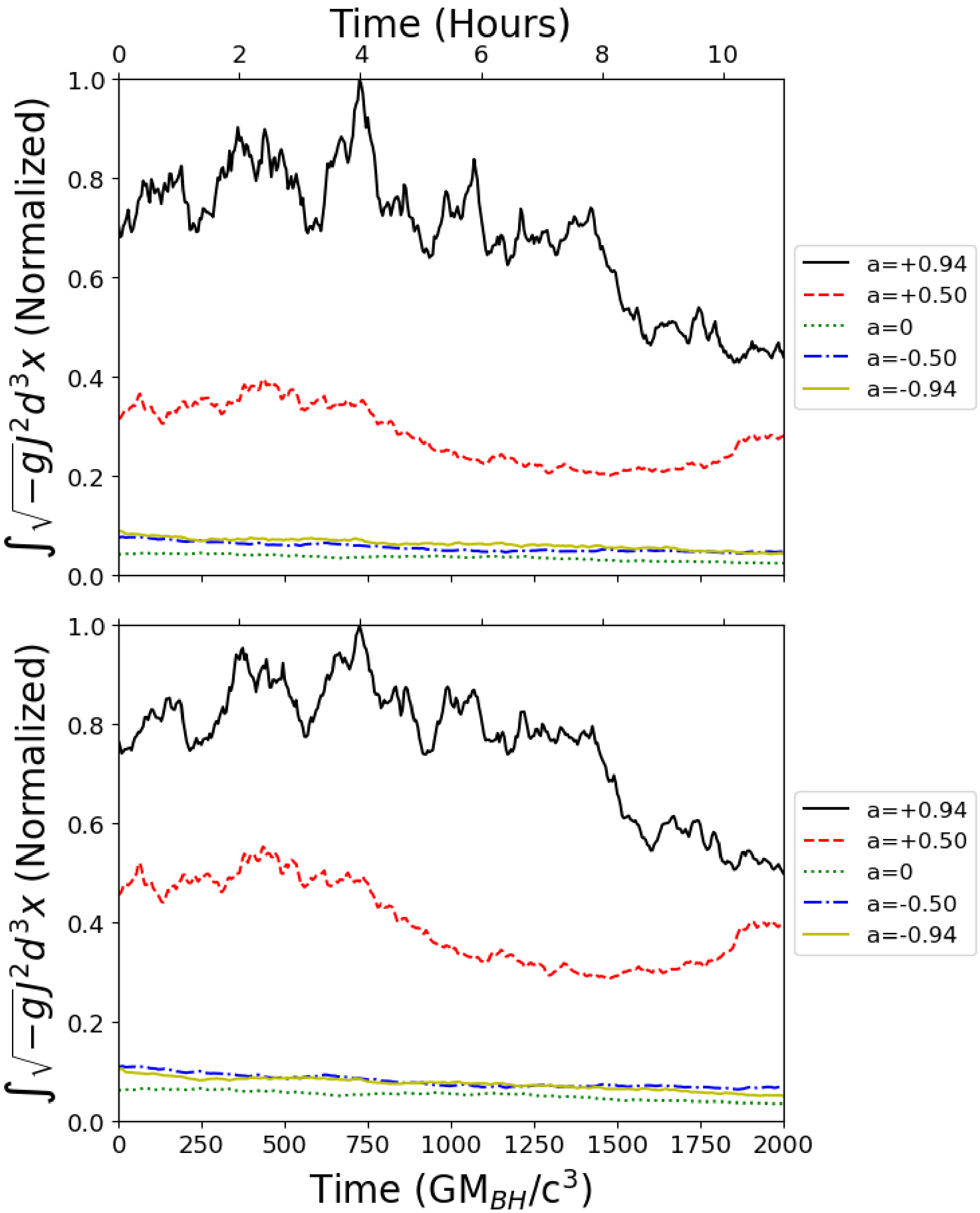

Figure 4.1: The normalized integral of J^2 integrated over the entire computational domain (top) or in the innermost region with $2GM_{BH}/c^2 < r < 5GM_{BH}/c^2$, i.e., removing the region least likely to produce NIR radiation (bottom), for all five spins.

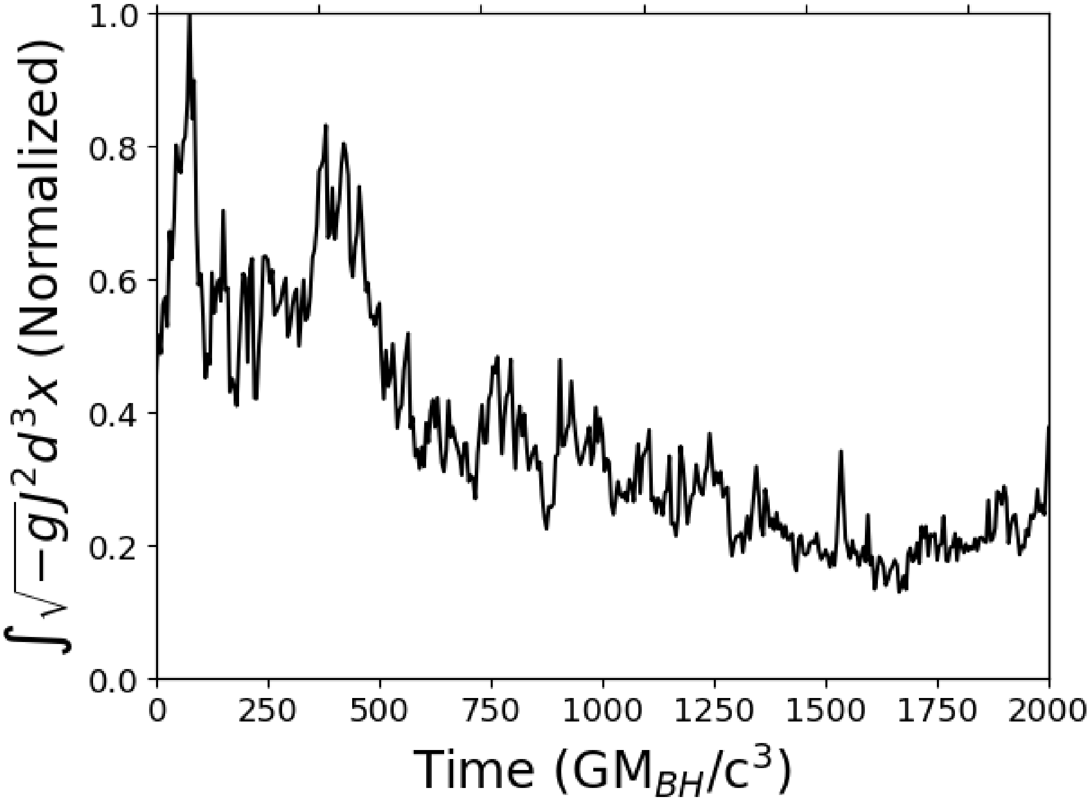

Figure 4.2: The normalized integral of J^2 integrated over a single azimuthal slice of the computational domain for the a=15/16 model. Variability is higher here than when integrating over azimuth as well as radius and polar angle.

integrated currents (integrated over the entire computational domain) can be seen; this is more in line with the variability seen in the 2D simulation (see chapter 3.5) and the observed NIR light curves.

Because NIR emission does not originate uniformly around the black hole (instead coming predominantly from the inner region of the disk) it is important to ascertain where current sheets form and, hence, where the nonthermal contribution to the 2.2 μm flux originates. The following plots (figures 4.3, 4.4, and 4.5) show how J^2 varies with radius and polar angle (averaging over time and azimuthal angle) for the SANE disk model with a=15/16.

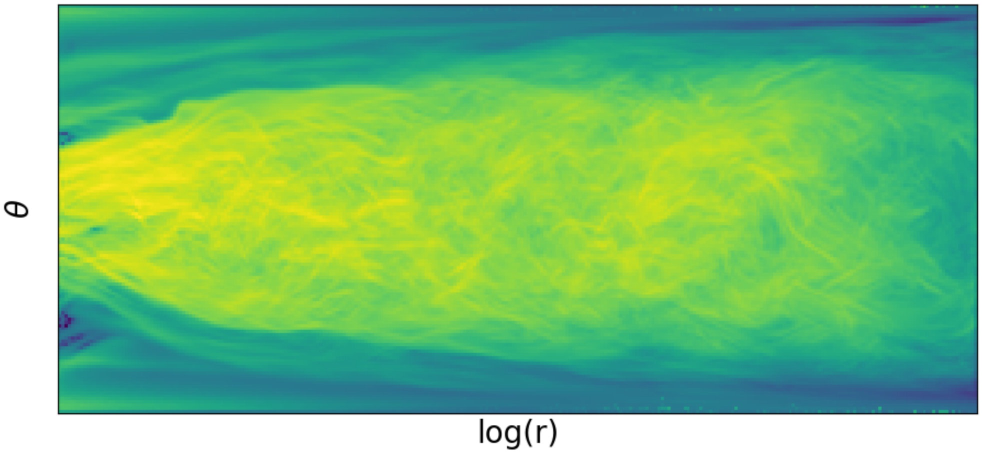

Figure 4.3: Log of <J^2> averaged over time and azimuthal angle as a function of radius and polar angle.

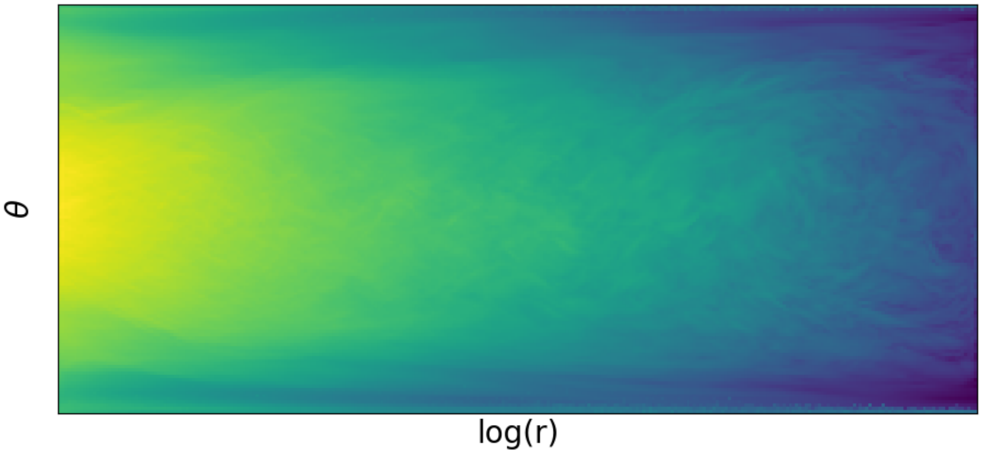

Figure 4.4: Log of standard deviation of J^2 over time and azimuthal angle as a function of radius and polar angle.

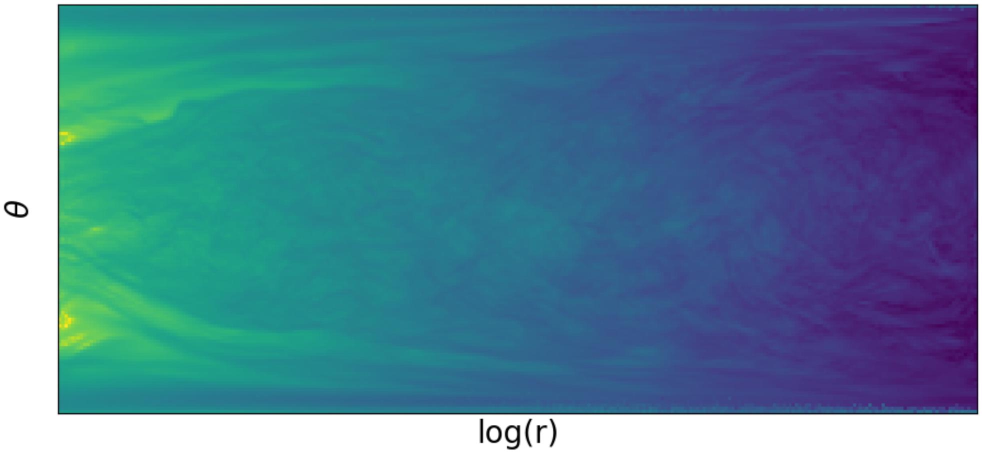

Figure 4.5: Log of standard deviation of J^2 divided by mean of J^2 over time and azimuthal angle as a function of radius and polar angle.

Figure 4.3 shows currents largely in the same region (the inner portion of the disk) as seen in figures 3.1 and 3.2 for the two dimensional case. The features are less sharp in figure 4.3 due to averaging. Figures 4.4 and 4.5 show that, while the largest variations in J^2 also occur in this region, the variations are small compared to the mean current.

4.2 2.2μm Light Curves and Images

The current distributions, along with other fluid variables from `iharm3d`, were used to perform radiative transport calculations with `ipole`. $\mathcal{M}$ was set by fitting the 230GHz flux density to the observed flux density of Sgr A*. The electron acceleration efficiency (C from table 3.1) for the r_{high} models was adjusted such that, if a flare were present, the flare would be as large as possible without overproducing (relative to Sgr A* observations) for the quiescent state. If no flare was present, the acceleration efficiency was adjusted to show overproduction for the quiescent state but no observable flare. The other thermodynamic

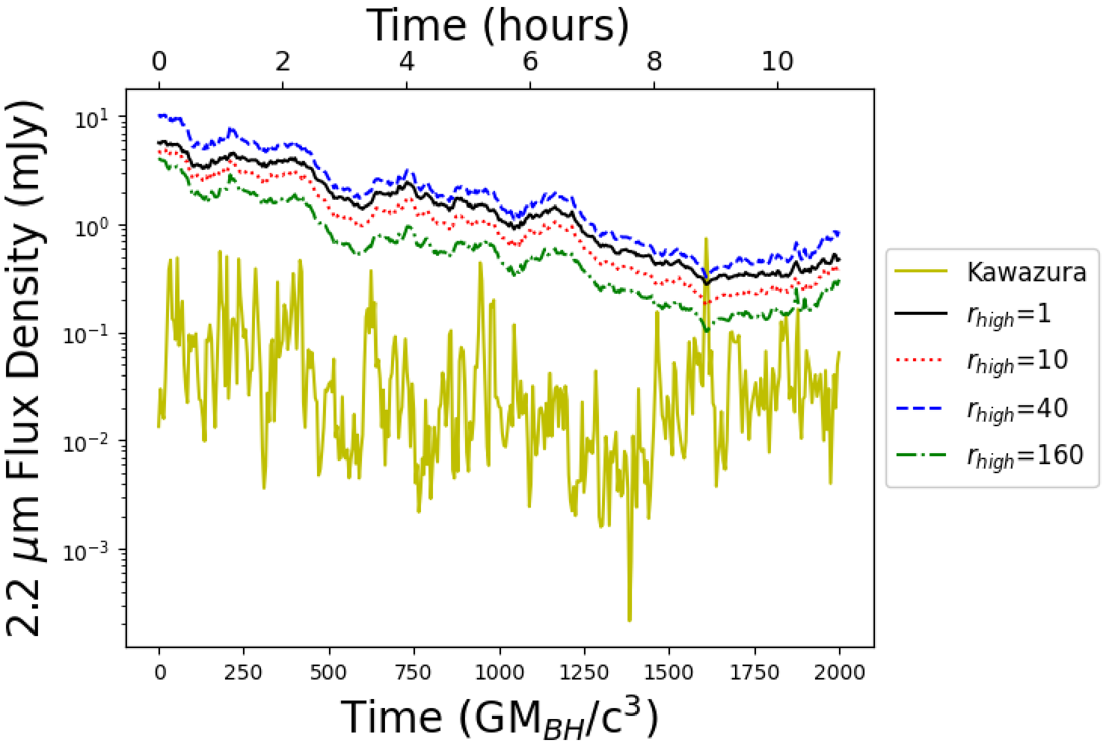

Figure 4.6: NIR light curves with inclination angle 10°. All r_{high} models include nonthermal components calculated by J^2 as described above. The light curve labelled "Kawazura" is purely thermal and uses the electron heating prescription from Kawazura et al. (2019).

model, the one with the electron temperature calculated with viscous heating, had no free parameters to adjust. No flare was produced for any model. Figures 4.6 – 4.10 each show the light curves for all five thermodynamic models for a given inclination angle. Only models with spin a=15/16 are shown here.

At high inclination, the Kawazura models overproduce NIR flux density for the entire duration of the calculation. No Kawazura model produces any large increase in emission, regardless of whether the baseline flux density would be consistent with 2.2μm observations of Sgr A*. Several combinations of spin, inclination angle, and r_{high} models also overproduce at 140THz. In these cases, no nonthermal contribution was included. Figure 4.11 summa-

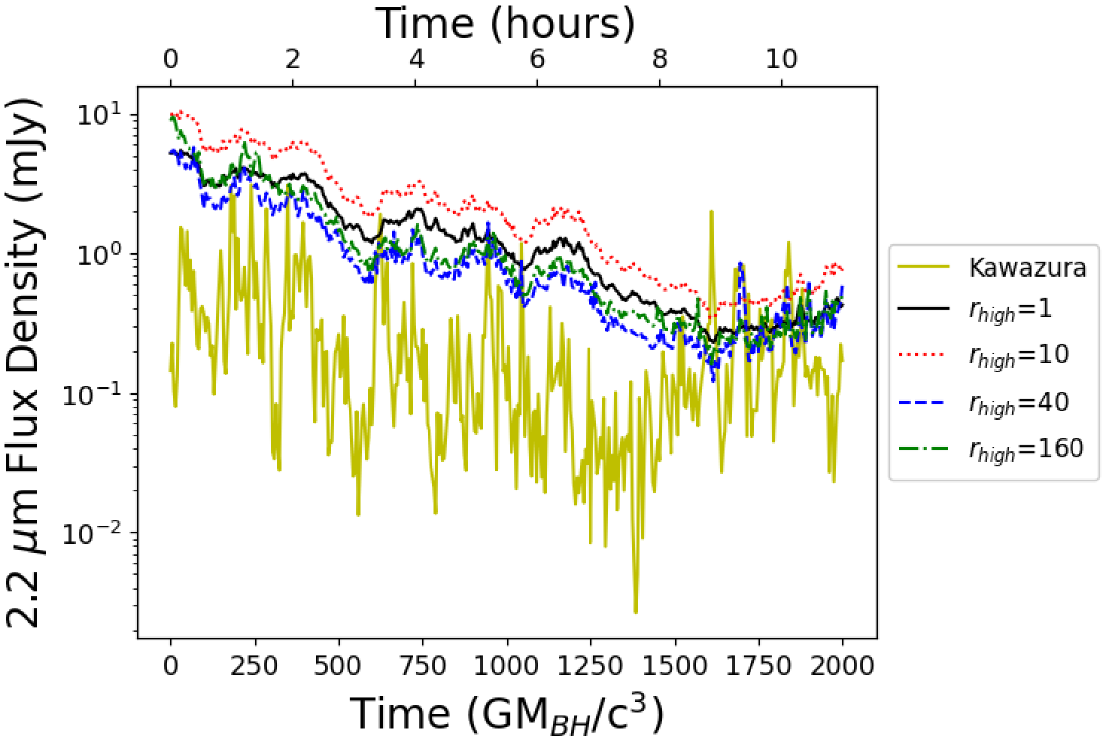

Figure 4.7: NIR light curves with inclination angle 30°. All r_{high} models include nonthermal components calculated by J^2 as described above. The light curve labelled "Kawazura" is purely thermal and uses the electron heating prescription from Kawazura et al. (2019).

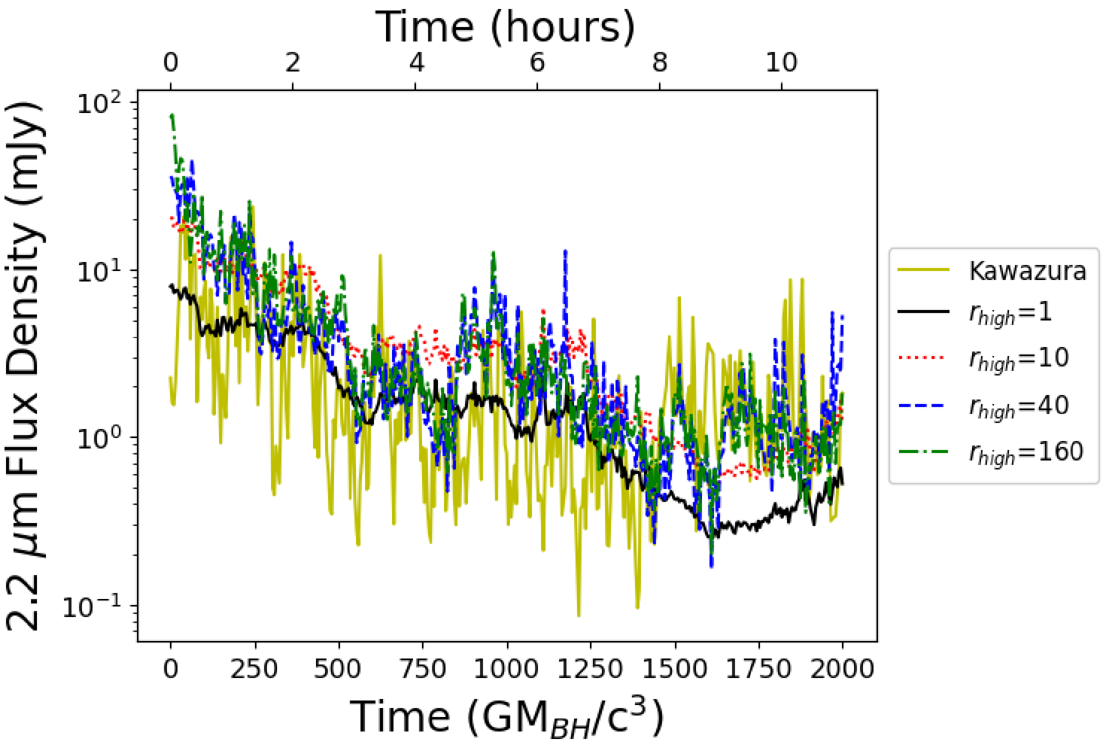

Figure 4.8: NIR light curves with inclination angle 50°. The r_{high}=1, 40, 160 models include nonthermal components calculated by J^2 as described above; the r_{high}=10 model includes only a thermal component and produces more NIR flux density than the observed quiescent state of Sgr A*. The light curve labelled "Kawazura" is purely thermal and uses the electron heating prescription from Kawazura et al. (2019).

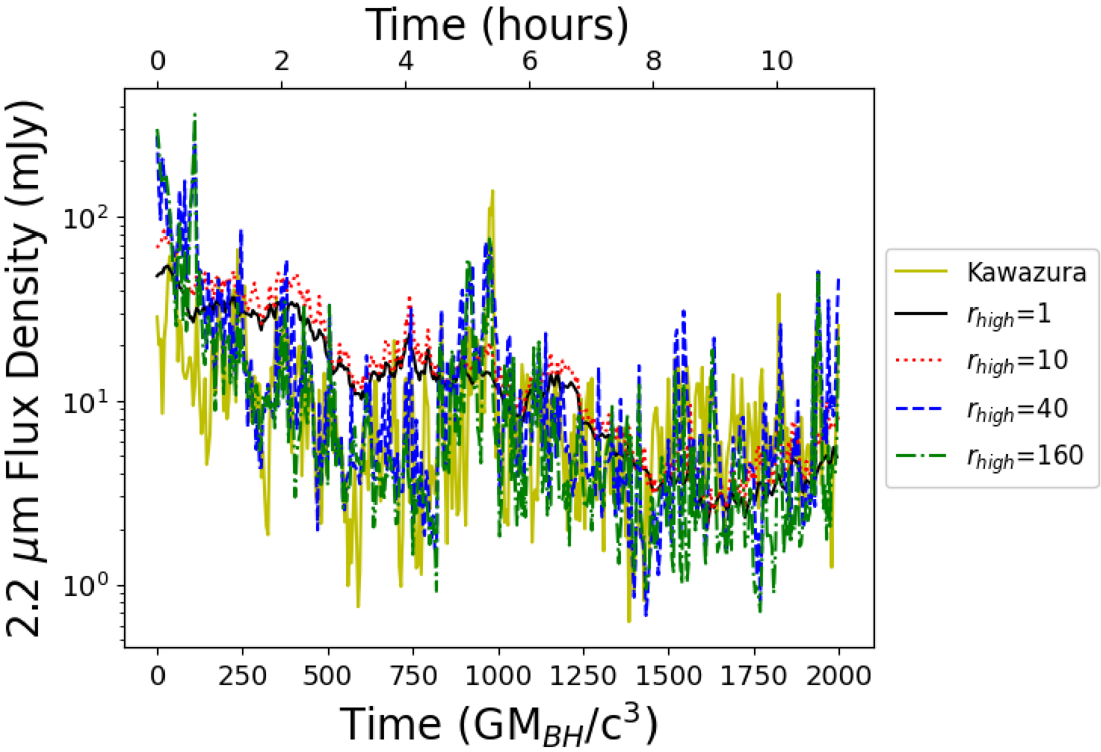

Figure 4.9: NIR light curves with inclination angle 70°. The r_{high}=1, 40, 160 models include nonthermal components calculated by J^2 as described above; the r_{high}=10 model includes only a thermal component and produces more NIR flux density than the observed quiescent state of Sgr A*. The light curve labelled "Kawazura" is purely thermal and uses the electron heating prescription from Kawazura et al. (2019).

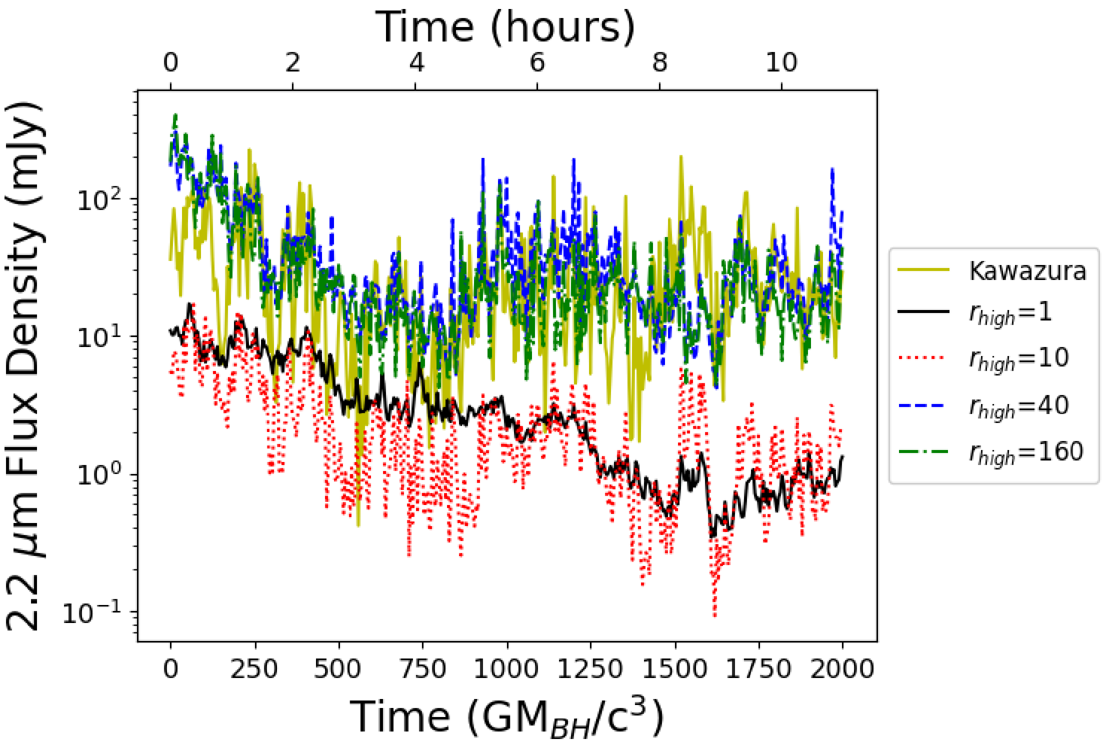

Figure 4.10: NIR light curves with inclination angle 90°. The r_{high}=1, 40, 160 models include nonthermal components calculated by J^2 as described above; the r_{high}=10 model includes only a thermal component and produces more NIR flux density than the observed quiescent state of Sgr A*. The light curve labelled "Kawazura" is purely thermal and uses the electron heating prescription from Kawazura et al. (2019).

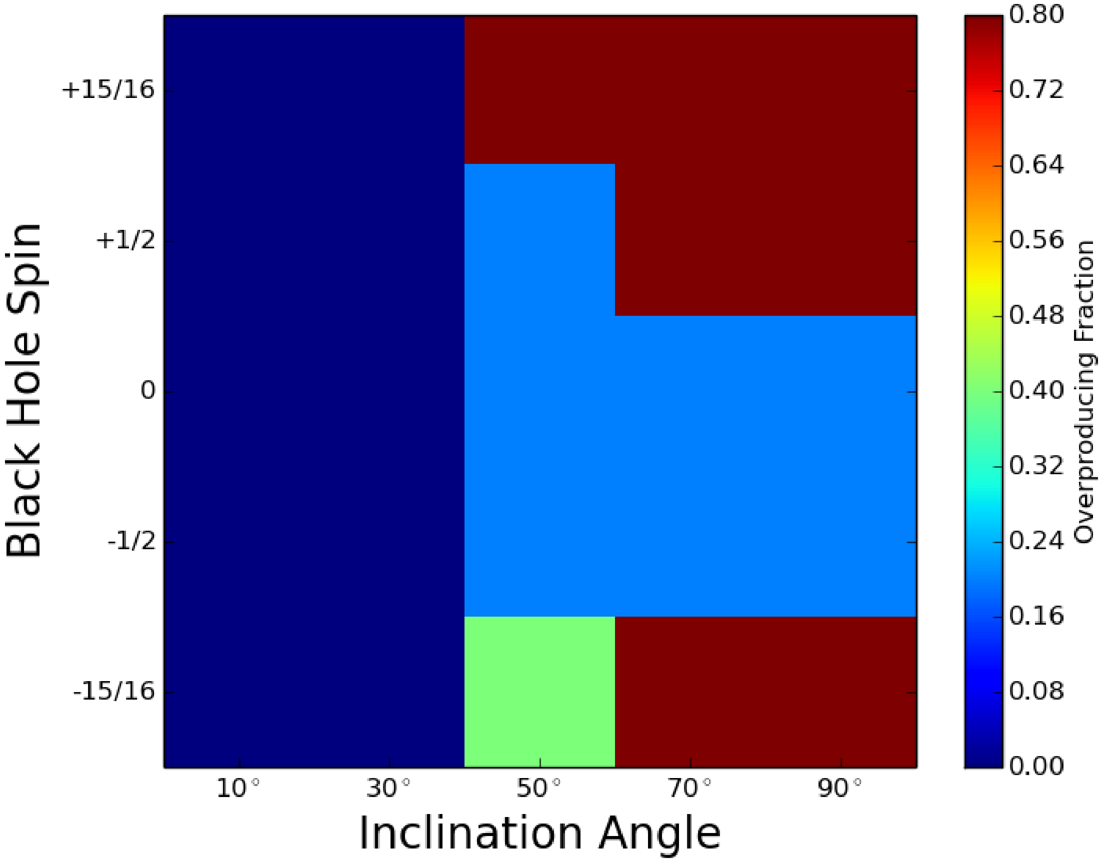

Figure 4.11: Overproduction for thermal SANE models. Thermal models tend to produce excess 2.2μm emission when viewed from nearly edge-on, especially around a rapidly spinning black hole.

rized the conditions under which thermal electrons alone produced too much NIR emission. Thermal r_{high} models also tend to overproduce for high inclination angles and large magnitude spins. This can be seen in figure 4.11, which summarizes the overproduction of NIR radiation for SANE models in all models examined here.

Nonthermal and thermal with viscous heating images (figure 4.12) are shown below for the SANE, a=15/16 model with an inclination angle of 30° and r_{high}=10 at the time with the greatest nonthermal flux (t=0). Instead of the usual 80×80 resolution, these images have 320×320 resolution. The nonthermal version produces 10mJy of total flux density and includes emission from an extended region close to the black hole shadow. Figure 4.13 shows the same image calculated with the Kawazura model, which shows emission in a much narrower region. Both models are brighter on the left because the sense of the disk rotation means that is the side where radiation is relativistically beamed and blueshifted toward the observer. The Kawazura model is dominated by this beamed emission while the nonthermal model is able to produce NIR photons from a larger region due to the higher energy electrons.

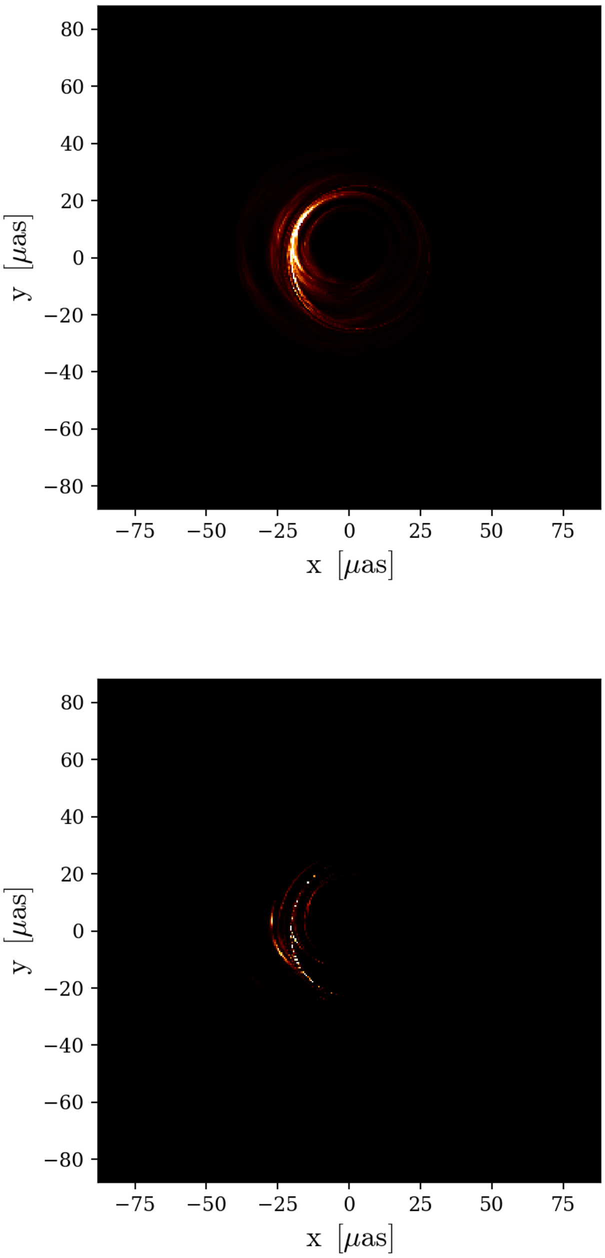

Figure 4.12: A nonthermal image (top) at 2.2μm for a SANE model with a=15/16, inclination angle 30° and r_{high}=10 corresponding to t=0 in figure 4.7 and a thermal image using the viscous electron heating prescription (bottom) with same parameters. The field of view for each image is 176μas (corresponding to 35$\mathrm{GM_{BH}/c^2}$).

4.3 Spectral Energy Densities

Figure 4.14 shows spectral energy densities for several SANE models with a=15/16. The observed spectral index of α ~0.6 (see 1.2.3) is obtained by the nonthermal model. The nonthermal model reaches a peak luminosity at frequencies slightly higher than 230GHz, follows a thermal decline until nearly the 140THz, at which point the nonthermal electrons begin to dominate the emission and produce the observed slope. The Kawazura model peaks at slightly higher frequency and shows a thermal drop in emission throughout the IR, leading to a flux density closer to the quiescent observations of Sgr A*. The thermal portion of the nonthermal model and the pure thermal model both have far too negative slopes compared to observations. The pure thermal model also produces too little radio flux at wavelengths longer than 1mm.

Both the pure thermal r_{high} and Kawazura models use only thermal electrons and the fluid parameters used to calculate the emission from each are the same except for the electron temperature. To understand the cause of the difference in light curves and spectra produced by these models, it is important to understand the temperatures produced by each model. Figure 4.15 shows electron temperatures for the r_{high}=10 and Kawazura heating models with a=15/16; all SANE models produce qualitatively similar results for all values of spin or r_{high}. The r_{high} model has a relatively diffuse region with high temperature, including in the inner portions of the disk. In contrast, the Kawazura heating prescription puts most of the hot electrons on the funnel wall.

4.4 Summary and Discussion

Three dimensional GRMHD simulations have been done with low magnetic flux and five black hole spins. These simulations show modest variability in the total current integrated over the computational domain, with more dramatic variability occurring in a single az-

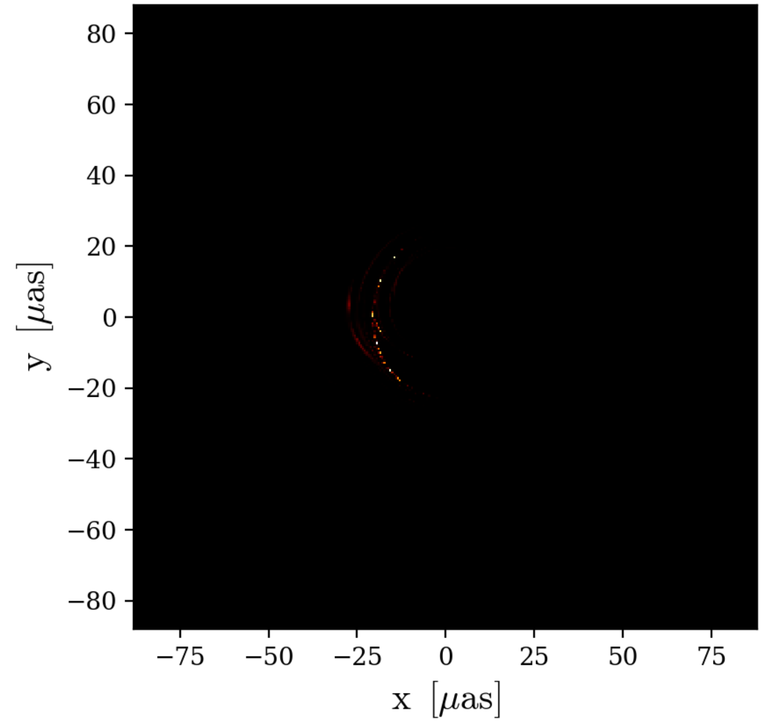

Figure 4.13: A thermal image at 2.2μm for a SANE model with a=15/16 and inclination angle 30° using the viscous electron heating prescription. This image corresponds to the time t=0 in figure 4.7. The field of view is 176μas (corresponding to 35GM$_{\mathrm{BH}}$/c^2). The dim emission comes from a narrow area, similar to the thermal r_{high}=10 model.

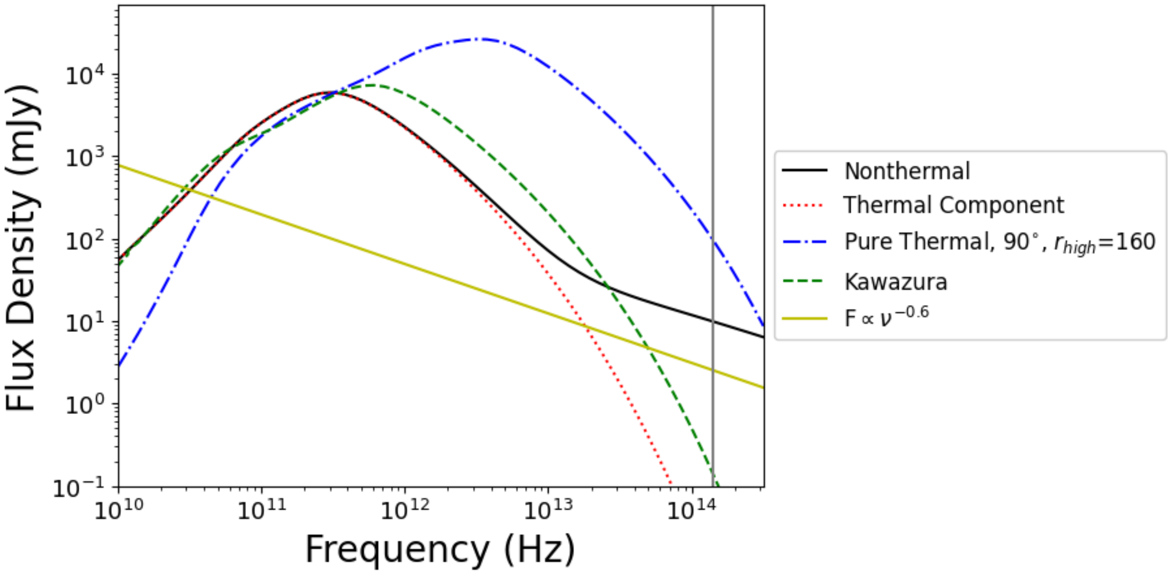

Figure 4.14: Spectral energy densities for several models with a=15/16. The vertical grey line is at 140THz. The nonthermal reproduces the expected slope (see 1.2.3) of -0.6. The thermal portion of that model contributes very little at high frequency. A purely thermal r_{high} model overproduces at 2.2μm, and has a slope that is far too negative. The Kawazura electron heating model has a similar slope as the thermal r_{high} models and has an intermediate flux density at 2.2μm.

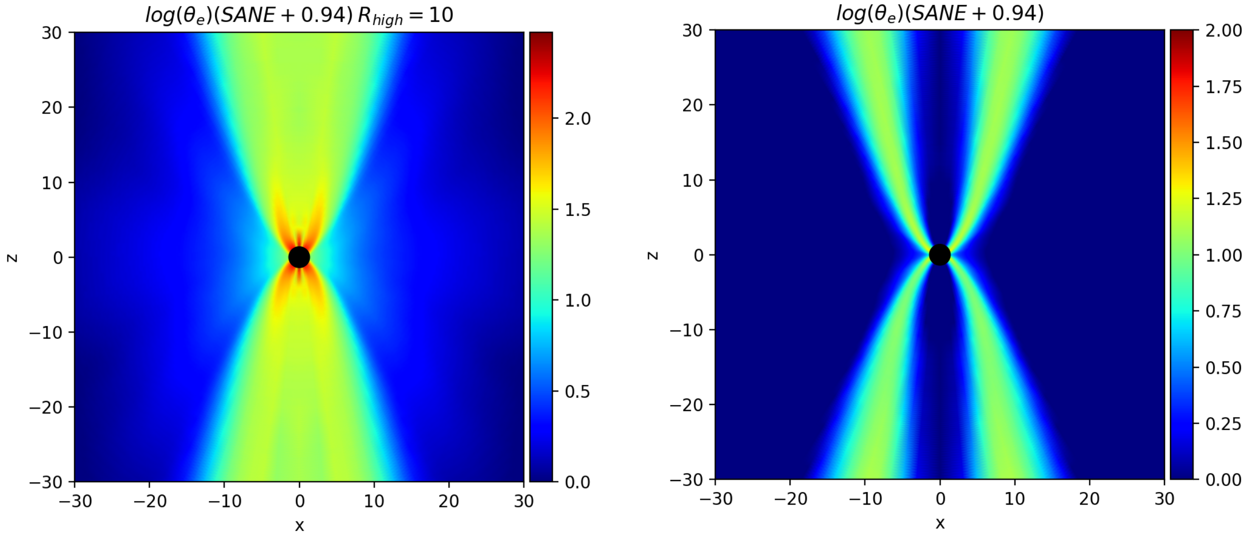

Figure 4.15: Electron temperatures for r_{high}=10 (left) and Kawazura heating (right) models with a=15/16. The r_{high} model includes warm regions in the funnel and the inner portion of the disk. In contrast, the model with Kawazura heating only has hot electrons along the funnel wall.

imuthal slice. Most of the current came from near the midplane of the disk at low radius, but the variability in this region was small. In axisymmetry, there is no azimuthal averaging so this could explain the higher variability seen with axisymmetric simulations. The variability was particularly small when the black hole had low spin or when the spin was opposed to the angular momentum of the disk.

Radiative transfer calculations were performed with each of the five fluid models at five inclination angles and using five thermodynamic models. Nonthermal images show a large emitting region while thermal models only emit NIR radiation from a very confined region near the black hole. No combination of spin, inclination, and electron thermodynamics model was able to produce a flare; some resulted in a persistent 2.2μm flux higher than the observed quiescent state of Sgr A* regardless of the nonthermal contribution. Models with a rapidly spinning black hole and an edge-on view of the disk were likely to overproduce in the

NIR. More dramatically, the models with an electron heating prescription from Kawazura et al. (2019) always overproduced at 2.2μm.

5 3D MAD Results

With the lack of flares seen in the 3D standard and normal evolution (SANE) models, a reasonable next step would be to repeat the process with a more variable magnetically arrested disk (MAD) model. MAD models are characterized by their large magnetic flux, which is defined as the surface integral of the magnetic field over one half of the horizon ($\Phi_{BH} \equiv \int_\theta \int_\phi B^r dA_{\theta\phi}$). In a MAD model, net magnetic flux is brought in with accreting matter until the dimensionless flux ($\phi_{BH} \equiv \Phi_{BH}/\sqrt{\dot{M} r_g^2 c}$, where r_g=$\mathrm{GM_{BH}/c^2}$) reaches a plateau at which the magnetic field is strong enough to slow further accretion.

The strong magnetic fields in these models come with stronger currents than the SANE models examined in chapter chapter 4. These strong currents come with increased resistive dissipation and, with the electron acceleration prescription described in chapter 3.1, possibly a strong, variable, nonthermal component to the 2.2μm emission. These MAD models also benefit from spending a longer duration in quasi-equilibrium due to the disk being drained at a slower rate. This greatly extends the length of the light curves. Encouragingly, MAD models have been reported by Gravity Collaboration et al. (2020) to produce substantial NIR variability in thermal models.

The procedure used here will largely follow chapter 4. The GRMHD calculations will be done for five black hole spins (a= 0, ±1/2, and ±15/16) and an adiabatic index of γ=13/9. All GRMHD simulations use a resolution of 384×192×192 (for the radial, polar, and azimuthal angles, respectively). The radiative transfer for the 5 GRMHD models is done using `ipole`. As in chapter 4, each model is examined with an inclination angle of 10°, 30°, 50°, 70°, or 90°. In turn, the flux density for each of these inclination angles is determined using a series of electron temperature models. The first (the Kawazura model, see Kawazura et al. (2019)) is calculated by `iharm3d` and evolves the electron temperature along with the rest of the fluid variables by assigning a fraction (this fraction being strongly dependent on plasma β) of the turbulent heating to the electrons. The remaining models (called r_{high} models) set the electron temperature by multiplying the ion temperature by a ratio (dependent on a constant, r_{high}, and plasma β, see equation 2.23). The four r_{high} models set r_{high}=1, 10, 40, or 160; an r_{high} of 1 means that the electrons and ions have the same temperature. A higher value for r_{high} would indicate a (physically more realistic; see, e.g., Sharma et al., 2007) scenario where the electrons are cooler than the ions (due to the poor coupling between ions and electrons and electrons radiating far more rapidly than heavy ions). Including the spin, inclination angle, and electron temperature prescription, this leads to 125 models to be examined. All images (e.g., those used in the calculation of light curves or spectral energy densities) have a resolution of 80×80 and a field of view of 176μas (or 35$\mathrm{GM_{BH}/c^2}$), unless otherwise stated.

5.1 J^2 Distribution

With the larger magnetic fields inherent to MAD models come larger currents. As that current is the cause of the dissipative heating and, ultimately, the nonthermal emission that is the goal of this thesis, it is important to describe these currents before continuing on to look at the nonthermal radiation caused by them. Figure 5.1 shows the total resistive dissipation, calculated by integrating J^2 over the entire computational domain, as a function of time for the a=15/16 model. Other spin models follow a similar pattern, but only one is shown here as the rapid variability would make the interpretation of multiple data sets difficult. A similar plot calculated for a reduced volume (the region bright in the NIR: the innermost region with radius between 2$\mathrm{GM_{BH}/c^2}$ and 5$\mathrm{GM_{BH}/c^2}$).

The very rapid variability, seen in the above plots as “spikes” represent short excursions from the standard, lower value for the integrated current. These spikes usually last for a few $\mathrm{GM_{BH}/c^3}$ (less than about ten minutes): much shorter than the observed flare duration of

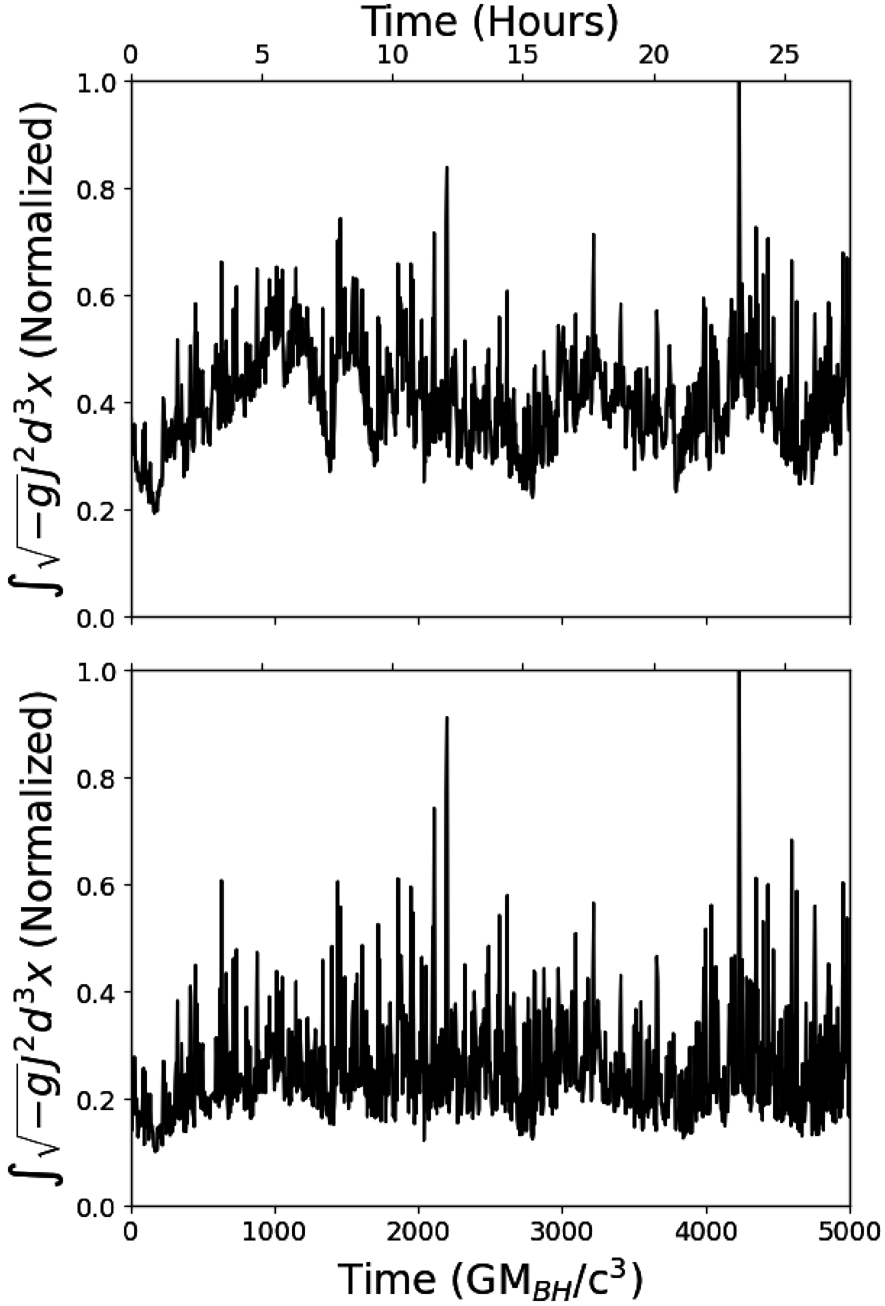

Figure 5.1: The normalized integral of J^2 integrated over the entire computational domain (top) or in the inner region with $2GM_{BH}/c^2 < r < 5GM_{BH}/c^2$, i.e., removing the region least likely to produce NIR radiation (bottom), for the a=15/16 spin model.

about an hour. While the spikes do tend to occur in clusters, the time average value for the integral rarely reaches a factor of two higher than the surrounding region. With a version of model D from chapter 3.1 the clusters of spikes might be able to provide a source of high energy electrons that produce a flare as they cool. However, the cooling time would need to be much longer than the several minutes calculated in chapter 3.1 (and much longer than the instantaneous cooling used here).

As a comparison to the 2D results of chapter 3, figure 5.2 shows the integrated current for a single azimuthal slice. Long time scale variability (on the timescale of hours) is higher here than in figure 5.1.

Figures 5.1 and 5.2 show the variation of current over time; figures 5.3, 5.4, and 5.5 show the current and its variation in the two other spatial coordinates, radius and polar angle. This is important as currents in the inner region of the disk will produce more NIR radiation than currents in exterior regions or near the poles.

As expected, the largest currents occur close to the hole and are concentrated around the relatively dense midplane. Unfortunately, this region does not see much variation, when compared to the mean value. Instead, the most variable regions are the exterior region of the disk and the area around each pole.

5.2 2.2μm Light Curves and Images

The fluid data from the `iharm3d` runs was used to perform radiative transfer calculations with `ipole`. As in chapters chapter 3 and chapter 4, the mm (230GHz) flux density is fixed to the observed flux density (see chapter 1.2.2) of ≈3.7Jy by scaling the mass of the simulated disk ($\mathcal{M}$). This leaves only the nonthermal efficiency, C (as in chapter 4, the less expensive model C from chapter 3.1 is used in place of the more meticulous model D), to be adjusted for the nonthermal models and no parameters at all to be adjusted for the

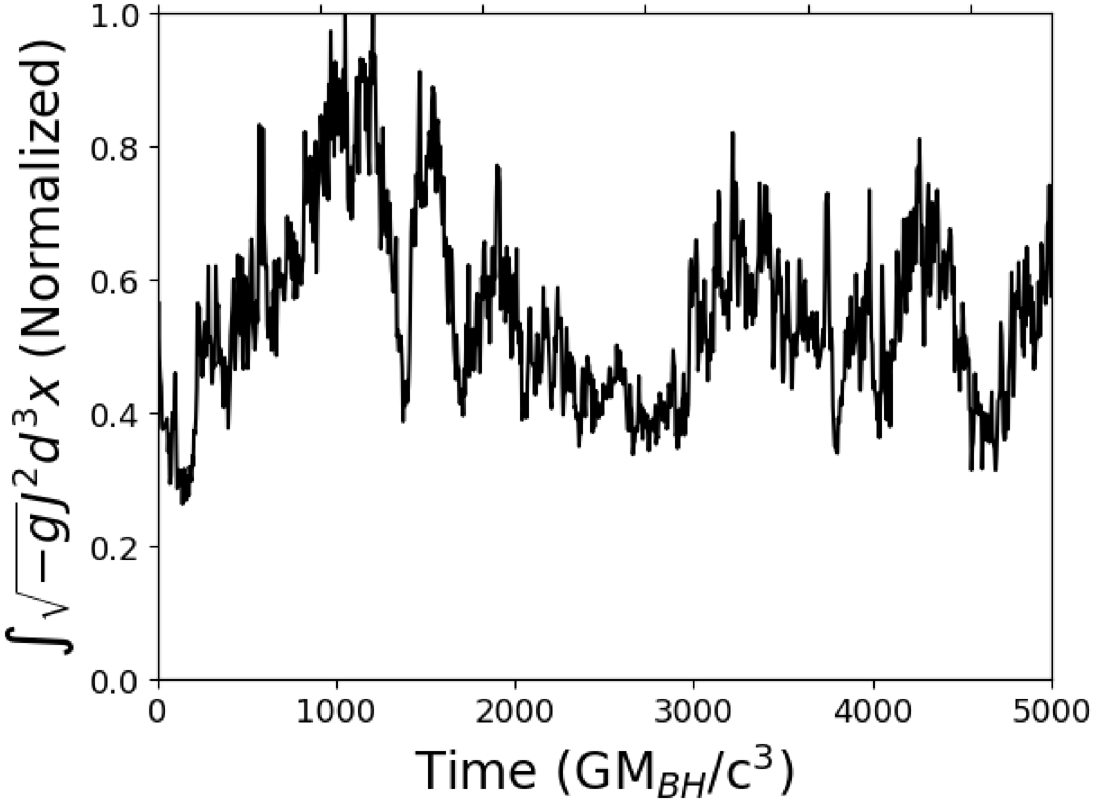

Figure 5.2: The normalized integral of the integral J^2 over a single azimuthal slice of the computational domain for the a=15/16 model.

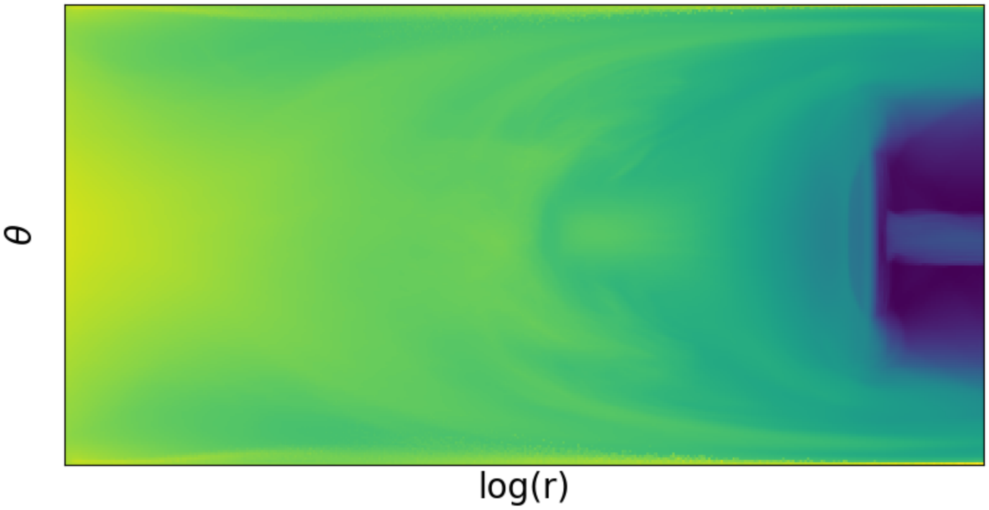

Figure 5.3: Log of $\langle J^2 \rangle$ averaged over time and azimuthal angle as a function of radius and polar angle.

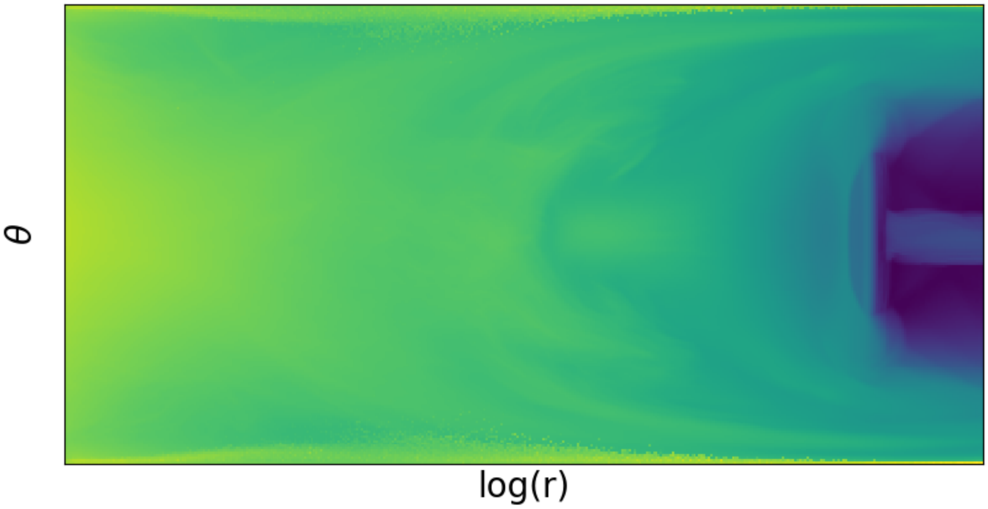

Figure 5.4: Log of the standard deviation of J^2 as a function of radius and polar angle.

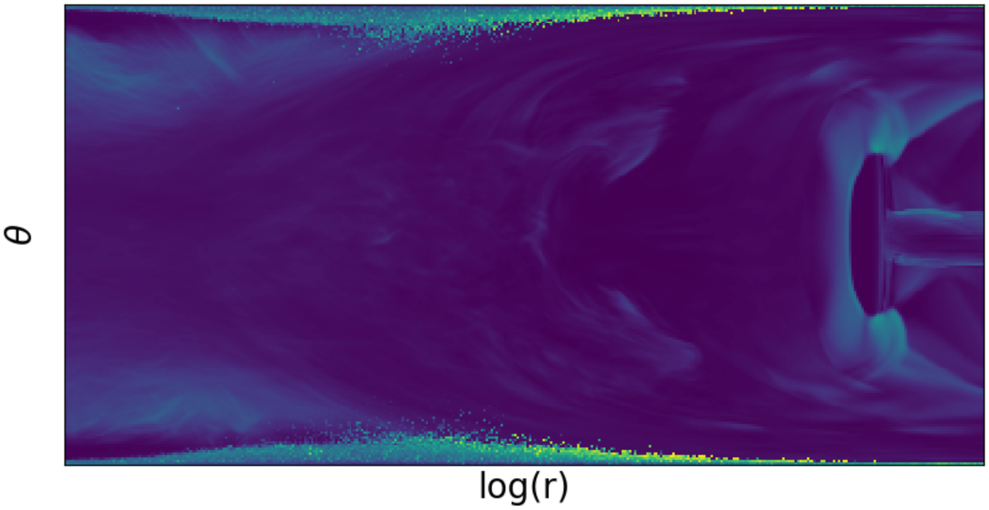

Figure 5.5: Log of standard deviation of J^2 (as in figure 5.4) divided by mean of J^2 (as in 5.3) over time and azimuthal angle as a function of radius and polar angle.

pure thermal models. The following light curves (figures 5.6 – 5.10) are the result. In many cases, moreso with the MAD models than with the SANE models, the Kawazura or pure thermal r_{high} models produced more 2.2μm emission than observed in the quiescent state for Sgr A* ($\lesssim$2mJy, see chapter 1.2.3). In these cases, the addition of a nonzero nonthermal component could only make the simulated light curve differ more from the observations, so the nonthermal component is set to zero. If the thermal flux is not too high, but no flare is present, the efficiency is adjusted to produce the largest quiescent flux possible to show that a flare cannot be created without violating the quiescent flux constraint. There are no models which have sufficiently low quiescent emission and flares of the expected magnitude and duration.

Many of the above light curves are too bright for most of the run. This is especially true for the low r_{high} models, which always produce too much NIR radiation. This is not altogether unexpected as these models likely underestimate the effect of cooling on the

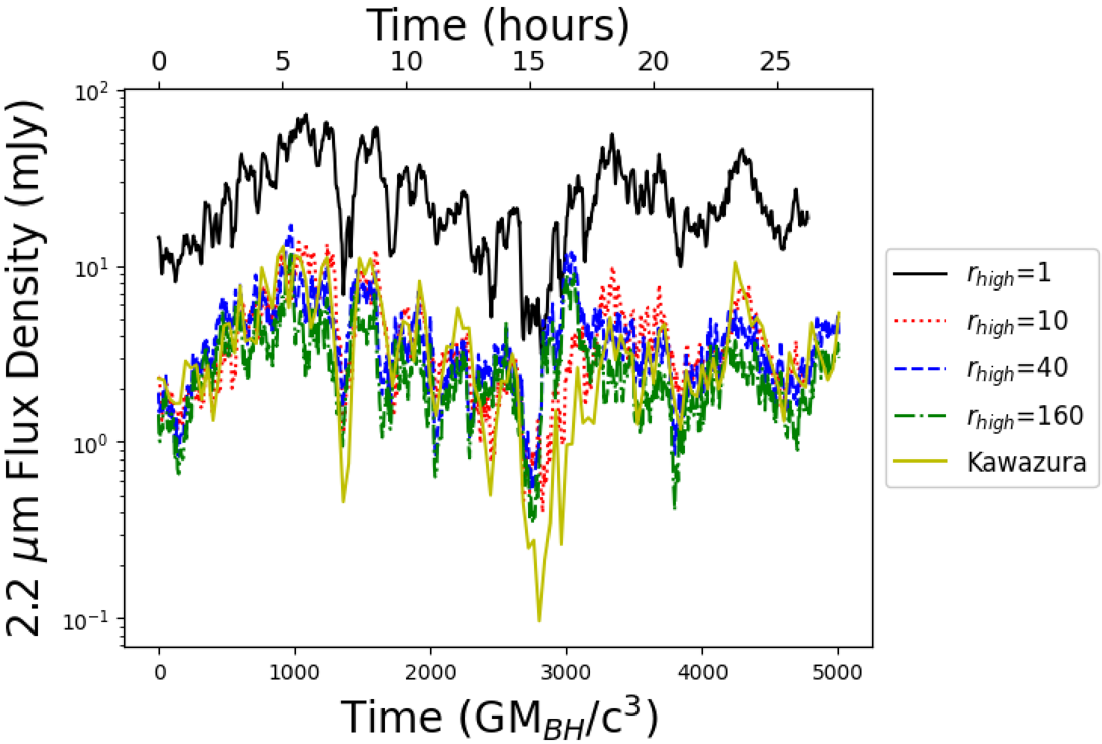

Figure 5.6: 2.2μm light curves with inclination angle 10°. The r_{high}=40, 160 models include nonthermal components calculated by J^2 as described above; the r_{high}=1, 10 models are purely thermal. The light curve labelled "Kawazura" uses the electron heating prescription from Kawazura et al. (2019).

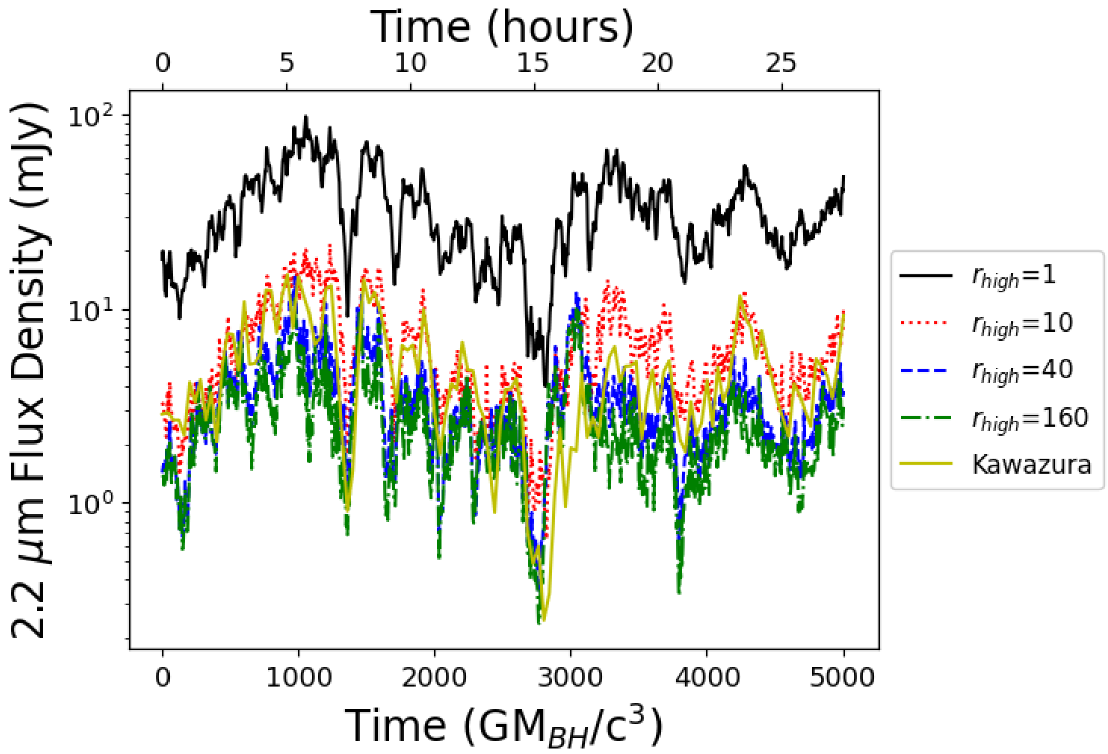

Figure 5.7: 2.2μm light curves with inclination angle 30°. The r_{high}=40, 160 models include nonthermal components calculated by J^2 as described above; the r_{high}=1, 10 models are purely thermal. The light curve labelled “Kawazura” uses the electron heating prescription from Kawazura et al. (2019).

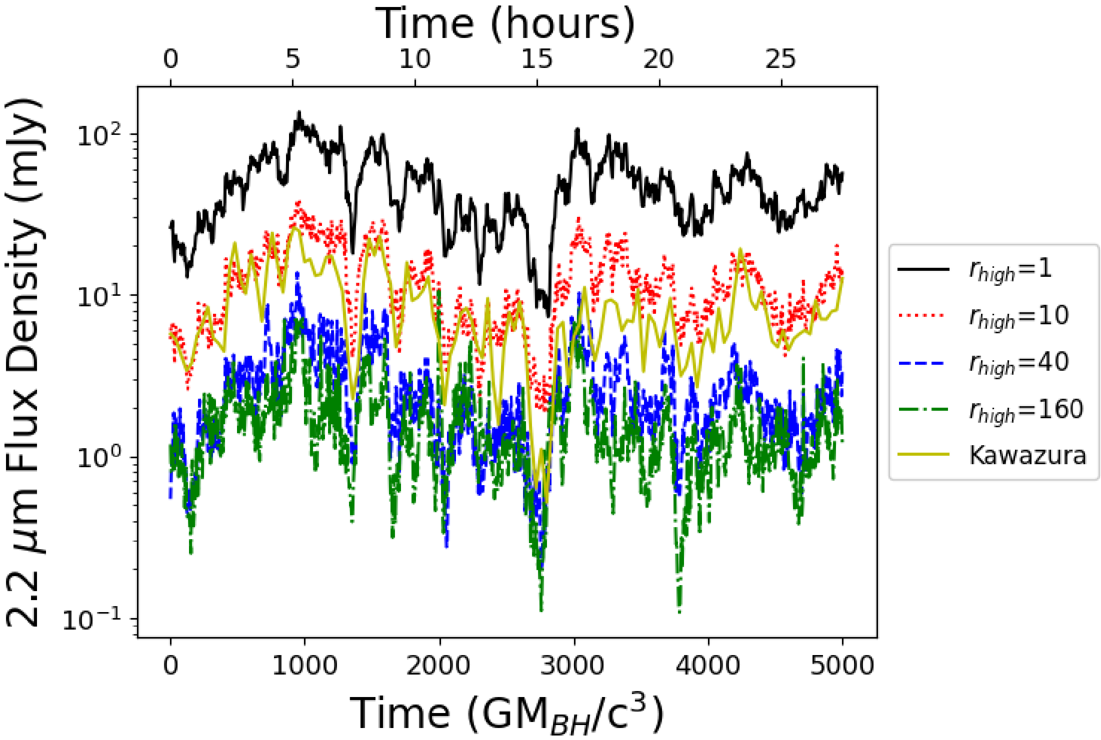

Figure 5.8: 2.2μm light curves with inclination angle 50°. The r_{high}=160 model includes nonthermal components calculated by J^2 as described above; the r_{high}=1, 10, 40 models are purely thermal. The light curve labelled “Kawazura” uses the electron heating prescription from Kawazura et al. (2019).

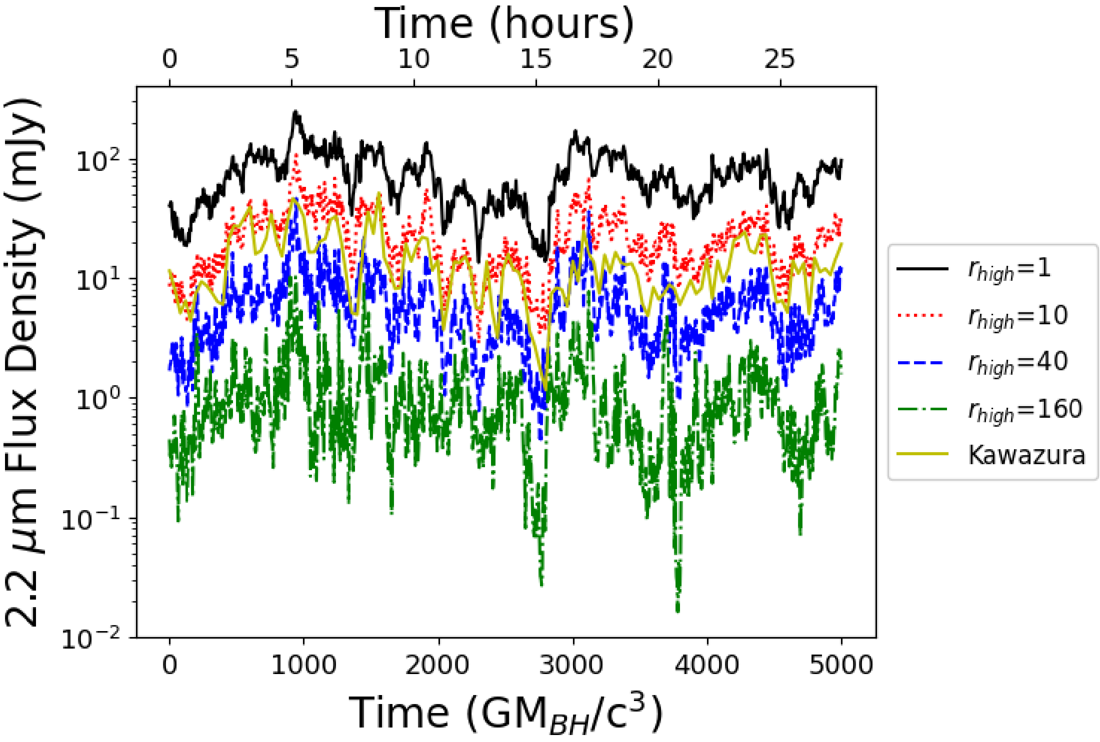

Figure 5.9: 2.2μm light curves with inclination angle 70°. All models are purely thermal. The light curve labelled "Kawazura" uses the electron heating prescription from Kawazura et al. (2019).

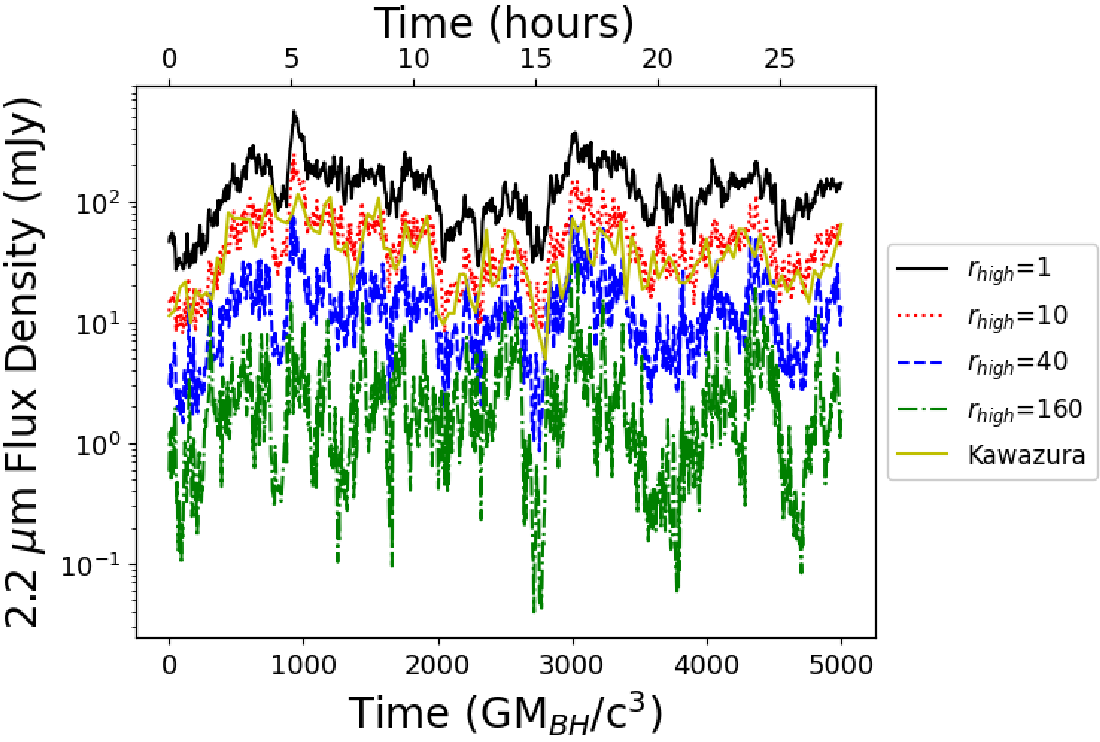

Figure 5.10: 2.2μm light curves with inclination angle 90°. All models are purely thermal. The light curve labelled "Kawazura" uses the electron heating prescription from Kawazura et al. (2019).

electrons by setting the electron temperature at or near the ion temperature. This effect is true for all models examined, as is summarized by figure 5.11. This plot, along with the above light curves, also shows that the Kawazura heating model also often leads to persistent high NIR flux. While the Kawazura light curves do not always match the r_{high}=10 model as well as shown above, they are usually reasonably close.

Another effect which can be seen by the above series of light curves is the increased excess flux produced at high inclinations (observing the disk nearly edge-on). One contributing factor to this trend is the rotation of the disk. With the steep drop in luminosity at the high frequencies examined here (see figure 5.14), the blue-shift and relativistic beaming add more to the emission on the approaching side of the disk than is lost from the receding side. Compounding this is the fact that, when viewed edge-on, the disk is optically thick at 230GHz but not 140THz. At 230GHz, much of the disk is hidden from view for an edge-on view, meaning that the total mass of the disk ($\mathcal{M}$) must be higher than for a face-on view in order to match the observed flux density. As the absorption for 2.2μm radiation is very small through the disk, this effectively means that more electrons are visible to a distant observer observing at a wavelength of 2.2μm than for a distant observer observing at wavelength 1.3mm.

Images of several models at 2.2μm for t=1000$\mathrm{GM_{BH}/c^3}$ can be seen in figure 5.13 NIR light curves with inclination angle 90°. The r_{high}=1, 40, 160 models include nonthermal components calculated by J^2 as described above; the r_{high}=10 model includes only a thermal component and produces more NIR flux density than the observed quiescent state of Sgr A*. The light curve labelled “Kawazura” is purely thermal and uses the electron heating model. The nonthermal model shows a pair of rings of fairly consistent brightness. This does not match with results from Gravity Collaboration et al. (2018), which show a hotspot orbiting the hole, as this model does not show any hotspot. The Kawazura heating model also shows a ring-like structure.

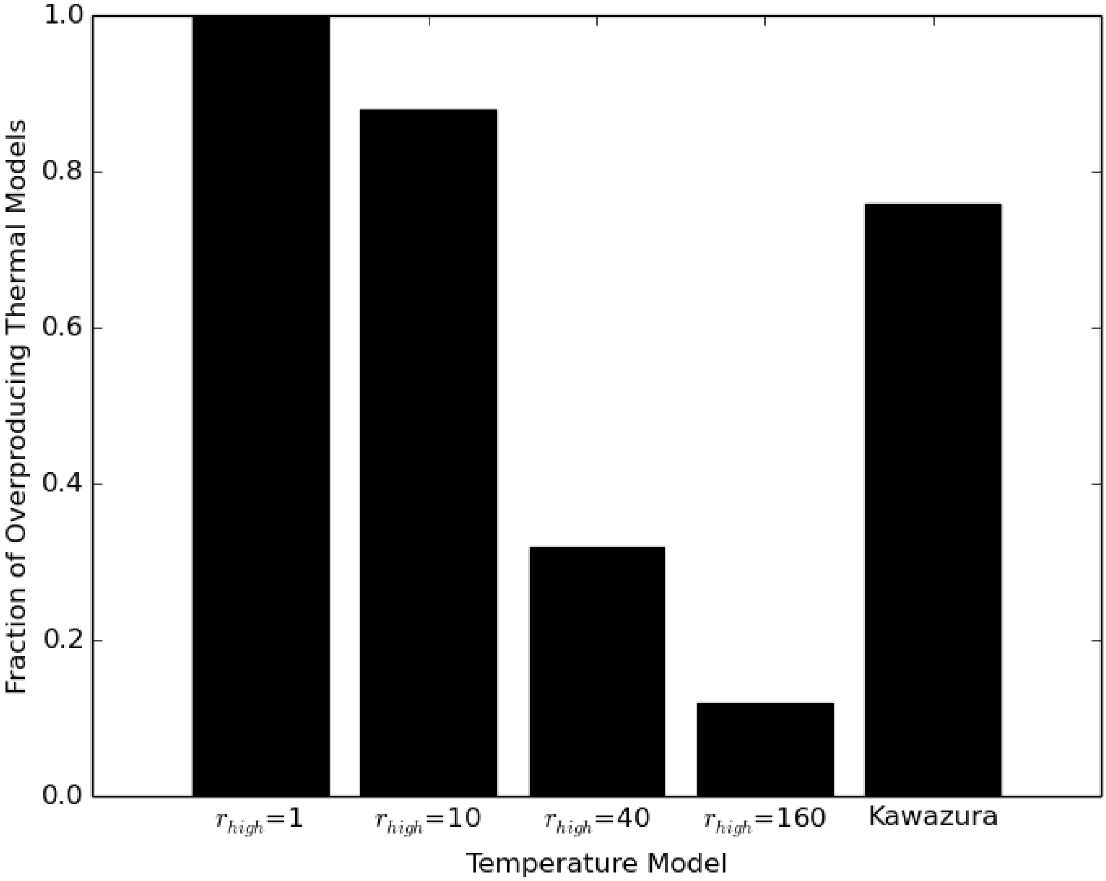

Figure 5.11: Overproduction for thermal MAD models binned by electron temperature model. Models using a larger value of r_{high} are less likely to produce excess quiescent 140THz emission than models with smaller values of r_{high}.

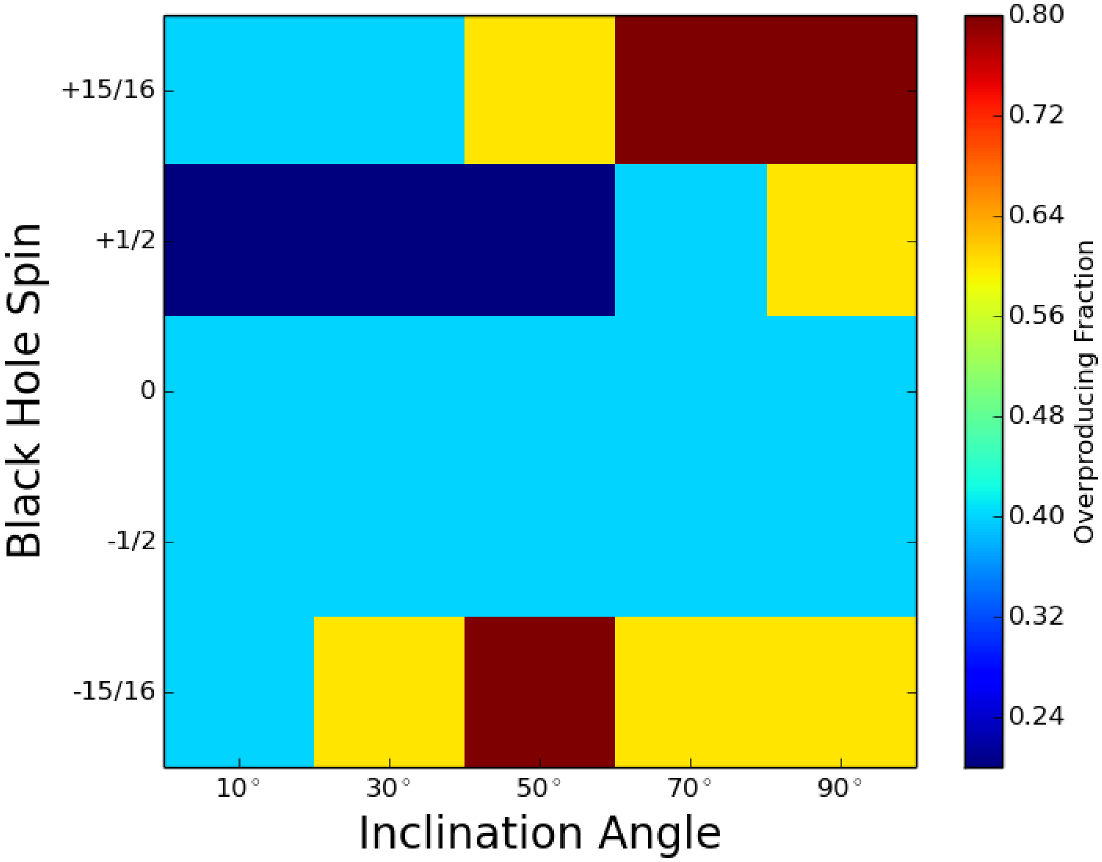

Figure 5.12: Overproduction for thermal MAD models. Thermal models tend to produce excess 2.2μm emission when using Kawazura electron heating models (Kawazura et al., 2019) or r_{high} models when viewed from nearly edge-on, especially around a rapidly spinning black hole.

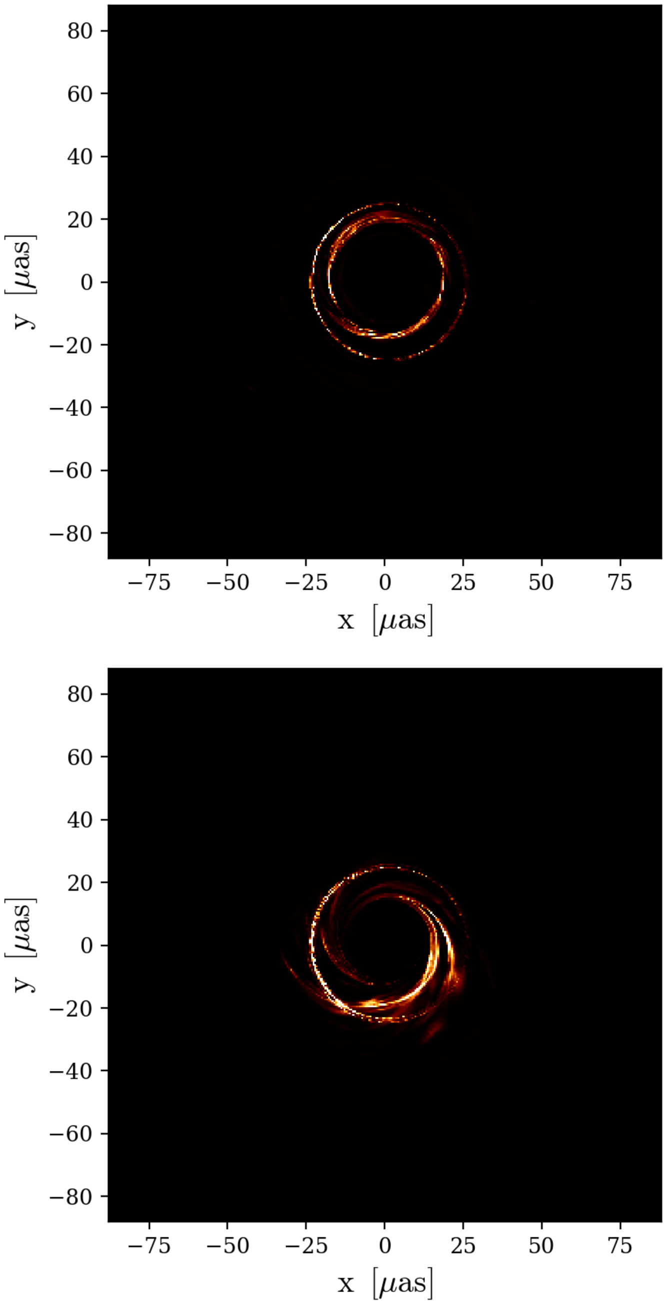

Figure 5.13: Images from MAD models with a=15/16 and inclination angle 10° (nearly face-on) corresponding to t=1000GM_{BH}/c^3 in figure 5.6. The field of view for each image is 176μas (corresponding to 35GM_{BH}/c^2). Each image has its own scale; the nonthermal image (top) has more total emission than the Kawazura heating model image (bottom).

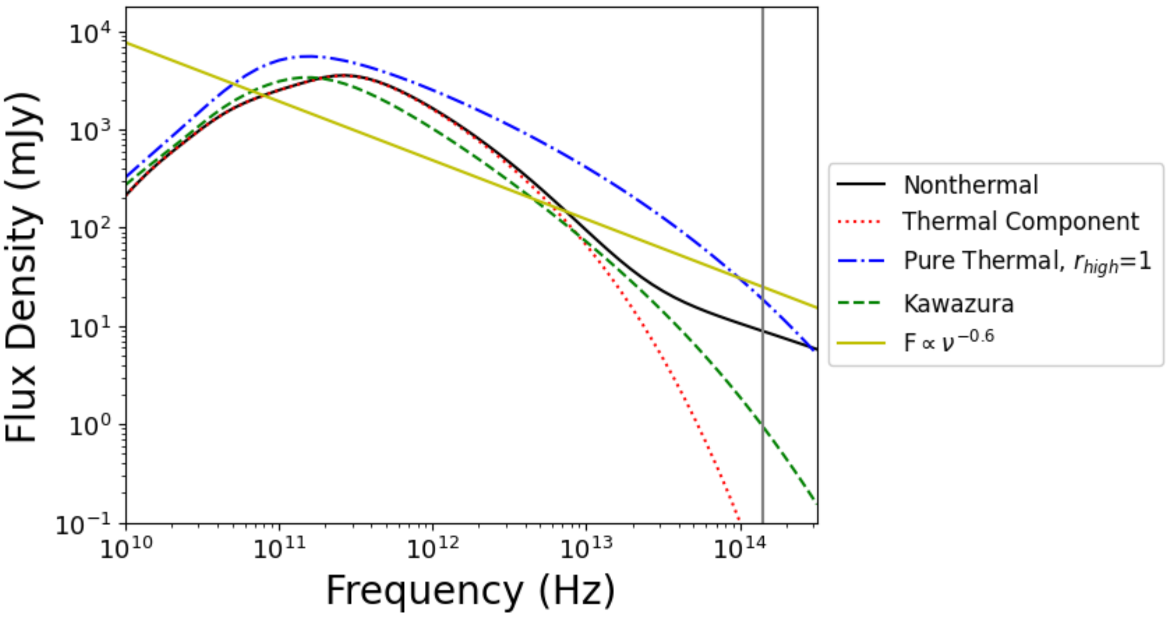

Figure 5.14: Spectral energy densities for several models with a=15/16 and inclination of 10°. The vertical grey line is at 140THz. The nonthermal (r_{high}=160) model reproduces the expected slope (see 1.2.3) of -0.6. The thermal portion of that model contributes very little at high frequency. A purely thermal r_{high}=1 model overproduces at 2.2μm, but has a slope that is too negative to match observations. The Kawazura model produces a reasonable flux density at 2.2μm, but the spectral slope is also too negative.

5.3 Spectral Energy Densities

While no model light curves have been able to match observed flares, one success of this nonthermal model is the ability to match the spectral slope observed for Sgr A* in the NIR (simply determined by the choice of κ in the κ distribution function though it may be). The thermal contribution to the nonthermal emission is clearly negligible at 2.2μm but is also dominant at 1.3mm. The extremely high temperature of the r_{high}=1 is seen by the slope barely steepening at 140THz. The Kawazura model, being thermal, is also unable to recreate the observed spectral slope.

The light curves in figures 5.6–5.10 seem to imply that there is some connection between

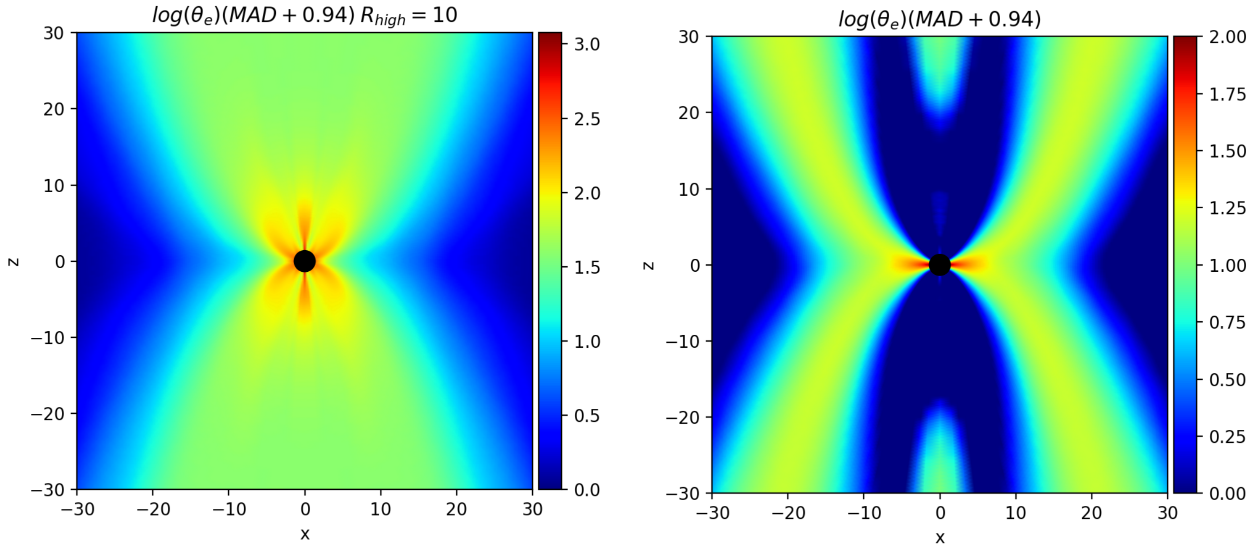

Figure 5.15: Electron temperatures for r_{high}=10 (left) and Kawazura heating (right) models with a=15/16.

the r_{high}=10 and Kawazura heating models. This is purely coincidental, however; figure 5.15 shows that the Kawazura models are much hotter (and, thus, brighter) near the midplane than the r_{high} models. Interestingly, the SANE models show the reverse trend, though in both SANE and MAD models the r_{high} prescription places warm electrons in the entire funnel region while the Kawazura prescription keeps hot electrons near the funnel wall.

5.4 Summary and Discussion

3D MAD models do produce more NIR variability than 3D SANE models, but not enough to explain the observations listed in chapter 1.2.3. For the nonthermal models, this variability is largely due to changes in the electric current in the inner portion of the disk. However, the current in the NIR emitting region varies on timescales much shorter than the flare timescale and the magnitude of the variance is smaller than the flare magnitude. This results in light curves which have rapid, small-scale variation, but no major flaring events.

Some models do not just fail to produce flares, but, even without a nonthermal contribution, they fail to produce sufficiently low emission for extended periods of time to match the observed quiescent state. This property is especially prevalent among models with a low value of r_{high}, Kawazura heating models, nearly edge-on models, and models with a rapidly spinning black hole. All of the models match observations in the mm region, so, despite not producing flares, these models can be useful in constraining the parameter space needed for further simulations of Sgr A*.

Finally, the spectral slope of the nonthermal models was able to match observations. This is the strength of a nonthermal model as the high energy tail of the distribution function can be made to naturally reproduce the observed slope while thermal models must rely on the Maxwell-Jüttner distribution function, which is steeply dropping at high energy. The effect of that steep distribution function was seen in the very negative slope in the NIR region of all of the thermal models studied here.

6 Conclusion

The supermassive black hole at the center of the Milky Way galaxy, Sgr A*, exhibits flaring behavior in the near infrared (NIR). When not flaring, Sgr A* produces very little NIR emission (around 1mJy). The flares increase the observed flux density by an order of magnitude or more, last for around an hour, and occur once or a few times per day. A peculiar feature of their flares is the spectrum, which does not appear to drop off as rapidly as would be expected of a thermal source at high frequency.

A more well-studied aspect of the emission from Sgr A* is the mm wavelength radiation. Here, Sgr A* is much more steady — the flux density rarely straying more than a factor of two away from the mean of 3.7Jy. The Event Horizon Telescope (EHT) collaboration has not only measured light curves, but, using interferometry, is actually able to image the accretion with appreciable resolution.

Due to the extreme conditions around the black hole (strong gravity, large magnetic fields, and high temperatures) simulations of the accretion flow must make use of general relativistic magnetohydrodynamics (GRMHD). Using GRMHD, it is possible to calculate the magnetic field as well as the density, internal energy, and velocity of the plasma around the black hole. In order to use these data to compare to the observed behavior of Sgr A*, one must use some form of radiative transfer to calculate an electromagnetic signal. Doing so involves a calculation of the emissivity and absorptivity of the electrons; the main mechanism relevant here is synchrotron emission/absorption as ions are too heavy to contribute much due to their lower accelerations. This involves modeling a temperature for the electrons, but, as the NIR spectrum drops much less sharply at high frequency than would be expected from thermal synchrotron emission, a nonthermal component may be necessary.

One nonthermal distribution function that could be used, called the κ distribution function, has been observed for electrons in the solar corona. This distribution can be approximated as a thermal core smoothly transitioning to a power-law tail. Particle-in-cell (PIC) simulations suggest that electrons in a magnetized plasma can be accelerated into such a distribution by resistive heating in reconnecting current sheets. Reconnection occurs when colliding streams of plasma bring oppositely aligned magnetic field lines into contact with each other, breaking the field lines, and then reconnecting them as they leave with the outflow. This process generates large currents which can rapidly heat the surrounding material.

6.1 Review

While many others have attempted to model the NIR flares of Sgr A* (with varying degrees of success), this work describes the first attempt to do so using electrons accelerated by resistive heating into a κ distribution function. This is done using GRMHD to solve for the fluid variables and radiative transfer to calculate the output flux density. This involves setting a value for κ, which is achieved by using a simple relation between the slope of the tail of the distribution and the slope of the spectrum.

Various models were tested for the acceleration of electrons using computationally inexpensive 2D GRMHD simulations. Pure thermal models suffered from the expected problems of low emission and very negative spectral index and models with a constant fraction of the electrons in the nonthermal component of the total distribution function showed insufficient variability. Two acceleration models were also tried. One heated the electrons in each zone of the simulation according to the square of the local current density (Joule heating) and cooled the distribution back to a thermal one as energy was lost to synchrotron radiation. This worked well (providing reasonable agreement with the observed flare magnitude, spectral index, and flux distribution), but a simpler model also performed adequately. As the cooling times were faster than the dynamical timescale of the fluid, this model simply set the nonthermal component of the distribution function proportionally to the square of the current density (effectively assuming instantaneous cooling). This approach has the benefit of separating the fluid run from nonthermal emission, allowing multiple iterations of the radiative transfer to be done using a single (computationally expensive) GRMHD run.

Knowing that the cheaper method worked, many iterations of it were performed with 3D simulations (where each model can be approximately three orders of magnitude more expensive than a 2D simulation) of both standard and normal evolution (SANE) and magnetically arrested disk (MAD) models. The SANE models did not produce the rapidly changing current sheets which would allow this model to match the observations of Sgr A*. While individual azimuthal slices did show variability closer to that observed in the axisymmetric case, averaging over azimuth substantially reduced the total variability. None of the models were able to produce flares and certain combinations of parameters (such as a rapidly spinning black hole and a nearly edge-on view of the disk) result in various electron temperature models that produce more NIR emission throughout the entire run than is observed in the quiescent state of Sgr A*. The nonthermal models were able to reproduce the spectral slope of Sgr A*, as expected given the choice of κ.

The MAD models fared little better. Many parameter choices for these models do not reproduce the quiescent state of Sgr A*, sometimes being off by well over an order of magnitude. The parameters which caused these failures are similar to the ones that caused failures in SANEs, but with the extra caveat that models that allow the electron temperature to be close to the ion temperature are especially likely to overproduce in the NIR. Though these models do have substantially more variable currents than the SANE models, the variability is only around a factor of two and the timescale for this variability is much less than the $\sim$1 hour timescale of the observed flares. This results in light curves with rapid variations too small and too fast to be considered flares. MAD models, too, were able to recreate the observed spectral slope.

6.2 Future Work

Future work will likely focus on the insufficient variability, as the choice of a κ distribution is physically well motivated, has led to consistent matches with the observed spectral slope, and does not produce any sharp features in the spectrum as might be expected of simpler nonthermal distribution functions.

Possible methods to achieve the requisite variability in the nonaxisymmetric simulations range from simple to complicated. The simplest method is to simply redo the SANE models with a larger initial torus. While this is more computationally expensive, it will allow for a longer time in the nearly steady state before the disk is drained of its initial matter. Another approach would allow the short duration spikes in current for the MAD models to produce longer lasting flares. By getting away from the "fast light" approximation (performing radiative transfer under the assumption that the light crossing time is much shorter than the timescale for changes in the fluid), a "slow light" model might spread out the increase in flux over a more reasonable timescale.

Most likely, a more fundamental of change to the acceleration mechanism will be required. This could be a refinement of the presently used technique, such as only heating the electrons in the current sheets under certain conditions. Another possible change to the model would be to vary the fraction of resistive heating that goes to the electrons in accordance with recent PIC simulations (see Rowan et al., 2017). Alternatively, a new approach could involve a more radical shift from an implicit resistive heating method to viscous heating; some authors (e.g., Gravity Collaboration et al., 2020) have already successfully produced substantial NIR variability using this method.

Finally, if flares are found in the simulations, there are some clear avenues to further expand the model. If flares are reproduced, then including the nonthermal distribution function with existing polarized radiative transfer codes (as opposed to simply using the unpolarized emissivity and absorptivity as is done throughout this work) would be important. Observations have already been made of the polarization of the NIR flares, so computations involving polarization would be excellent further tests of the model. In this work, no attempt was made to explain the X-ray variability, which is observed to be linked to the NIR variability. Explaining that connection would require two main additions. First, a cutoff to the κ distribution would be needed, as the electrons further down the tail of the distribution (those producing X-rays) cool much faster than those producing NIR radiation. Second, another radiative transfer method would be needed to incorporate bremsstrahlung and inverse Compton scattering (far more important sources of X-ray radiation than synchrotron emission). Monte Carlo schemes already exist to do this, but they would have to be modified to include the nonthermal distribution function.

Appendices

A Dissipation in Relativistic MHD

This appendix will show that the heating rate per unit volume caused by resistive dissipation is J^2/σ when using the simplest covariant model of Ohm's law.

By Maxwell's equations,

$$j^\mu = F^{\mu\nu}{}_{;\nu}. \tag{A.1}$$

This can be projected into the space normal to the plasma four-velocity, u^μ, using the projection tensor,

$$h^\mu_\nu \equiv g^\mu_\nu + u^\mu u_\nu. \tag{A.2}$$

We can then define the projected current,

$$J^\mu \equiv h^\mu_\nu j^\nu. \tag{A.3}$$

A simple model for Ohm's law can then be written as

$$J^\mu = \sigma F^\mu{}_\nu u^\nu, \tag{A.4}$$

where σ is the conductivity. It is easy to show that this reduces to the familiar form of Ohm's law for a scalar conductivity.

Next, observe that

$$T^{\mu\nu}{}_{;\nu} = 0, \qquad (\rho u^\mu)_{;\mu} = 0 \tag{A.5}$$

and so,

$$u_\mu T^{\mu\nu}{}_{;\nu} + (\rho u^\mu)_{;\mu} = 0. \tag{A.6}$$

For an ideal fluid stress-energy tensor, it follows that

$$u^{\nu} u_{;\nu} + (u+p) u^{\nu}{}_{;\nu} = 0. \tag{A.7}$$

where u is the internal energy and p is the pressure. This is the internal energy equation as derived from the first law of thermodynamics assuming that the dissipation function is $\rho \mathrm{T} \mathrm{ds}/\mathrm{d}\tau = \rho \mathrm{T} \mathrm{u}^{\mu} \mathrm{s}_{;\mu} = 0$, where τ is proper time. The scalars s and T are the entropy and temperature, respectively.

Consider a magnetized fluid with electromagnetic and ideal fluid portions of the stress-energy tensor: $\mathrm{T}^{\mu\nu} = \mathrm{T}^{\mu\nu}_{\mathrm{FL}} + \mathrm{T}^{\mu\nu}_{\mathrm{EM}}$. Then

$$u_{\mu} T^{\mu\nu}_{;\nu} + (\rho u^{\mu})_{;\mu} = 0 = -\rho T u^{\mu} s_{;\mu} - u_{\mu} T^{\mu\nu}_{EM;\nu}. \tag{A.8}$$

From Misner et al. (1973) (MTW), exercise 22.10 (which uses a symmetry argument and Maxwell's equations)

$$T^{\beta}_{EM\alpha;\beta} = -F_{\alpha\mu} j^{\mu}. \tag{A.9}$$

Combining this with equation A.8 results in

$$\rho T u^{\mu} s_{;\mu} = -u^{\alpha} \left(-F_{\alpha\mu} j^{\mu}\right). \tag{A.10}$$

Ohm's law then implies

$$\rho T u^{\mu} s_{;\mu} = \frac{1}{\sigma} J^{\mu} j_{\mu} = \frac{J^2}{\sigma}. \tag{A.11}$$

This quantity is positive definite because J^{μ} is spacelike by construction and, therefore, the second law of thermodynamics is satisfied.

B The Effect of Nonthermal Parameters

Axisymmetric model D, described in the subsection 3.1, depends on the parameters η (the efficiency with which currents accelerate electrons into the nonthermal distribution), τ_{cool} (the modeled cooling time for the nonthermal electrons), and κ (the slope of the power law tail of the electron distribution function). This appendix is an exploration of the dependence of the simulated light curves and SEDs on these parameters.

B.1 Dependence on τ_{cool} and η

If the nonthermal electrons are in equilibrium, equation 3.1 can be set to zero. Further, if $\mathrm{n_{e,NT}}/\mathrm{n_{e,total}}$ is small (which is equivalent to small $\eta\tau_{\mathrm{cool}}$), then the nonthermal electron density (which is directly related to the NIR emission) is proportional to the product $\eta\tau_{\mathrm{cool}}$. This is shown in figure B.1, which shows the average and peak flux density for light curves of several variants of model D. The scaling of flux density with $\eta\tau_{\mathrm{cool}}$ shows that it is the product of η and τ_{cool} that determines the NIR flare amplitudes.

Figure B.2 shows the effect of changing η and τ_{cool} (with $\eta\tau_{\mathrm{cool}}$ constant) on the light curve. For large enough cooling times, increasing τ_{cool} causes the accelerated electrons to stay around for longer, thus increasing the FWHM of the flare. As τ_{cool} becomes shorter, however, this ceases to be the case. In this limit, the FWHM of the flare is determined by the duration of the reconnection event as electrons are continuously accelerated even as they cool. This justifies the use of model C, which is the short cooling time limit of model D. Thus, η only affects the amplitude of the flare while τ_{cool} affects both the amplitude and, if the cooling time is long compared to the duration of the reconnection event, the duration of the flare.

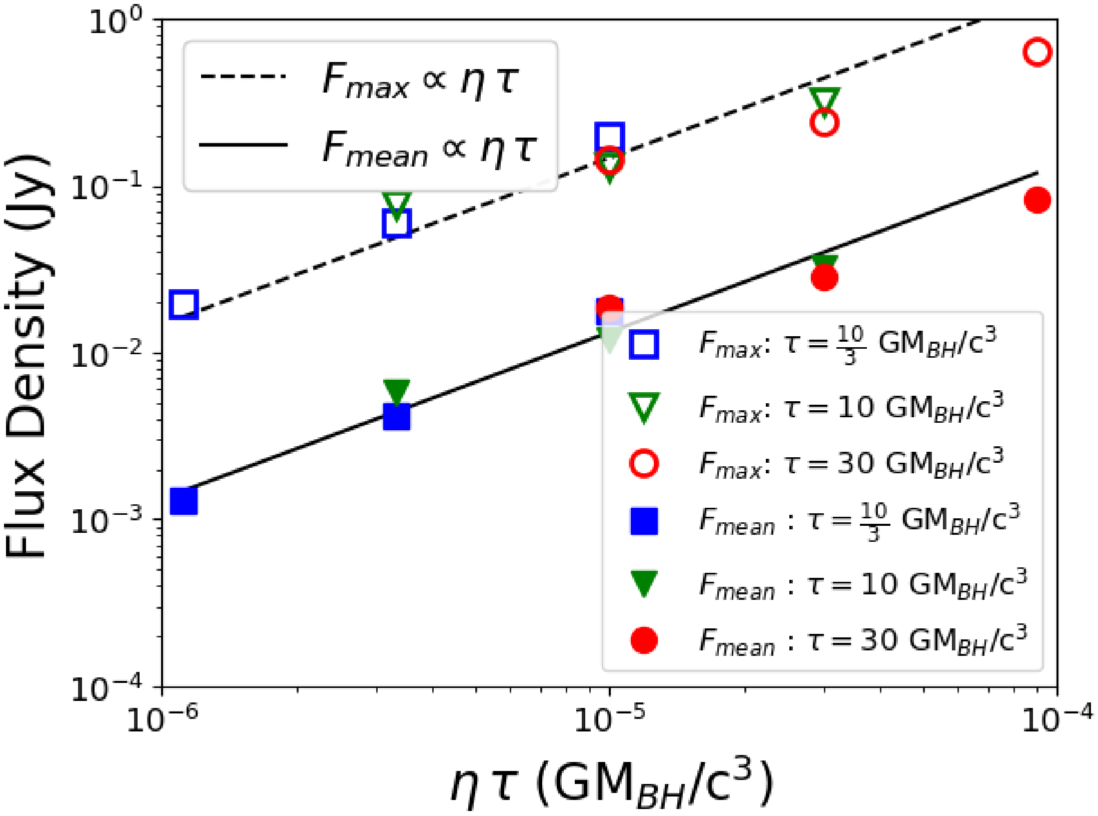

Figure B.1: Mean and peak flux density as a function of $\eta\tau_{\rm cool}$ for nine light curves based on model D with various values of η and $\tau_{\rm cool}$. Both the mean and peak flux density scale with the product $\eta\tau_{\rm cool}$.

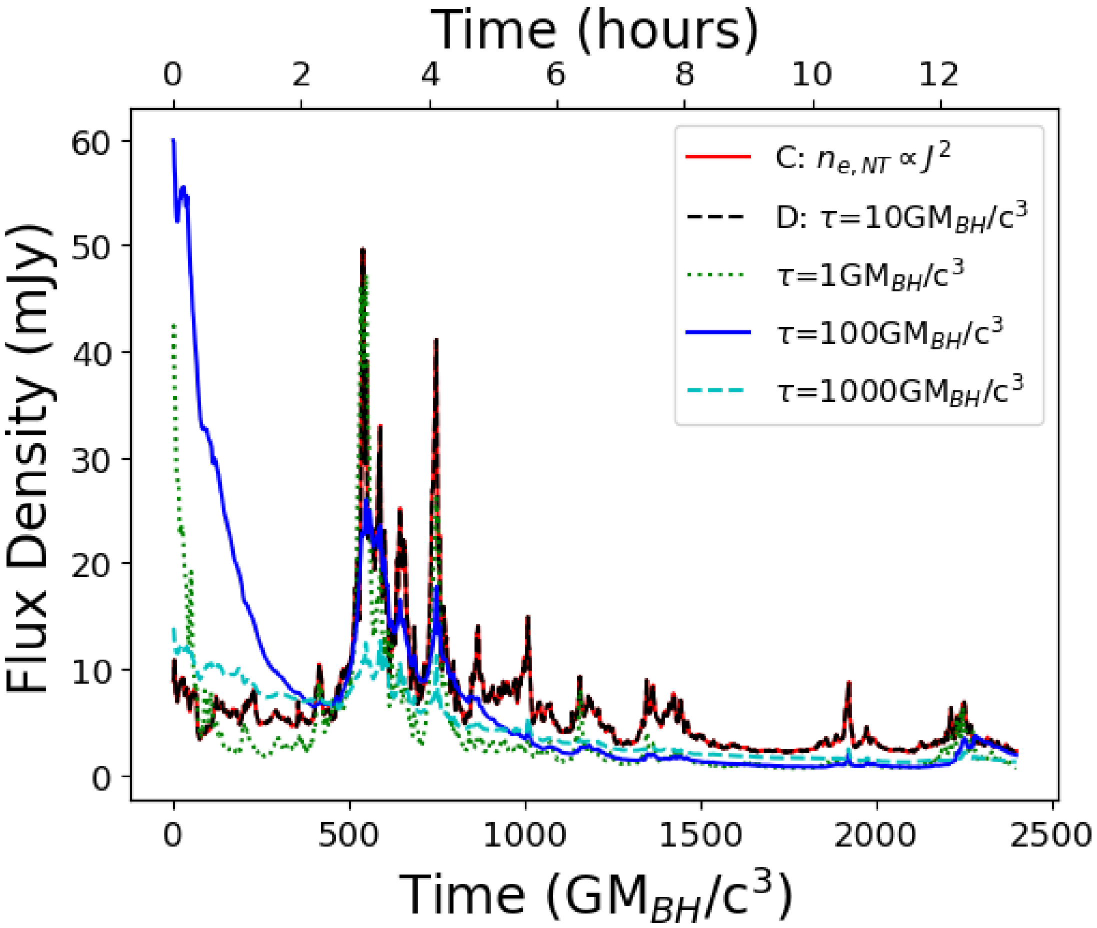

Figure B.2: NIR light curves for variations of model D with differing τ_{cool} but constant $\eta\tau_{\text{cool}}$. Long τ_{cool} flares show a larger FWHM than model D while short cooling time flares are almost identical as the FWHM for these flares is dominated by the duration of the reconnection event, not the time scale for electron cooling.

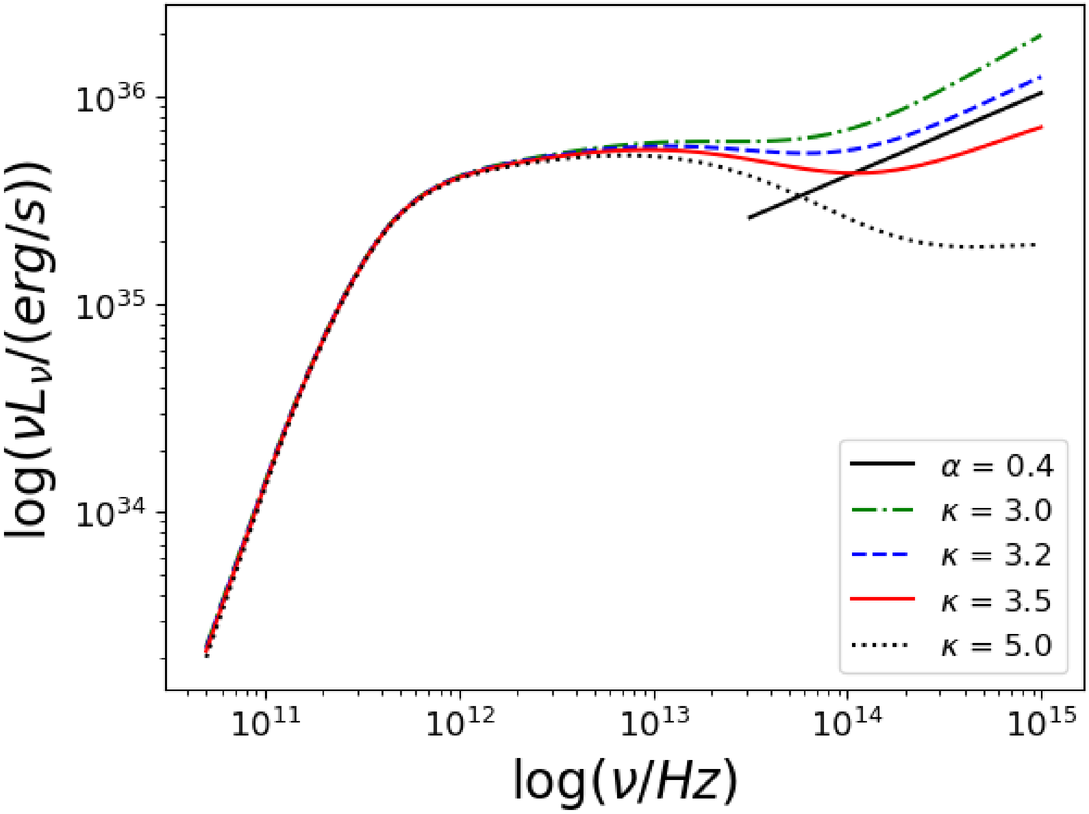

Figure B.3: SEDs from several variations of axisymmetric model D during a flare ($t=550GM_{BH}/c^3$). The expected value of κ, 3.2, reproduces the observed slope in the NIR region.

B.2 Dependence on κ

Equation 2.20 relates κ to the NIR spectral slope. However, the observed spectral slope and the κ found from PIC simulations do not match exactly. Figure B.3 shows the SEDs during a flare for several variations of axisymmetric model D with values of κ. This plot shows that equation 2.20 is valid during the flare and that κ=3.2 provides a good match to observations. Figure B.4 shows the same thing, but during quiescence.

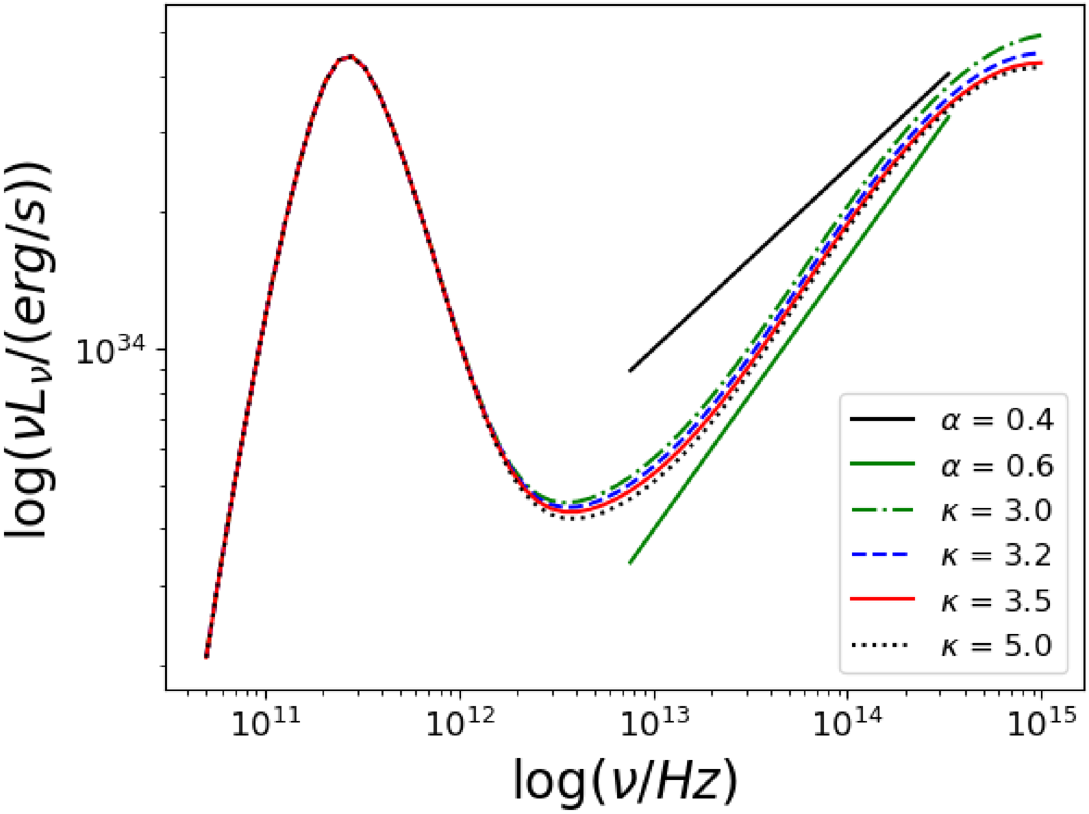

Figure B.4: SEDs from several variations of axisymmetric model D during quiescence (t=1700GM$_{\mathrm{BH}}$/c^3). The expected value of κ, 3.2, reproduces the observed slope in the NIR region.

Bibliography

Roy P. Kerr. Gravitational field of a spinning mass as an example of algebraically special metrics. *Phys. Rev. Lett.*, 11:237–238, Sep 1963. doi: 10.1103/PhysRevLett.11.237. URL `https://link.aps.org/doi/10.1103/PhysRevLett.11.237`.

Charles W. Misner, Kip S. Thorne, and John Archibald Wheeler. *Gravitation*. W. H. Freeman, 1973. ISBN 0716703440. URL `https://www.amazon.com/Gravitation-Charles-W-Misner/dp/0716703440?SubscriptionId=0JYN1NVW651KCA56C102&tag=techkie-20&linkCode=xm2&camp=2025&creative=165953&creativeASIN=0716703440`.

James M. Bardeen, William H. Press, and Saul A. Teukolsky. Rotating Black Holes: Locally Nonrotating Frames, Energy Extraction, and Scalar Synchrotron Radiation. , 178:347–370, December 1972. doi: 10.1086/151796.

P. Padmanabhan. *Theoretical astrophysics. Vol.1: Astrophysical processes*. Cambridge University Press, October 2000.

H. Netzer. Active Galactic Nuclei: Basic Physics and Main Components. In D. Alloin, editor, *Physics of Active Galactic Nuclei at all Scales*, volume 693 of *Lecture Notes in Physics, Berlin Springer Verlag*, page 1, 2006. doi: 10.1007/3-540-34621-X_1.

R. D. Blandford and R. L. Znajek. Electromagnetic extraction of energy from Kerr black holes. , 179:433–456, May 1977. doi: 10.1093/mnras/179.3.433.

Clive Tadhunter. An introduction to active galactic nuclei: Classification and unification. , 52(6):227–239, Aug 2008. doi: 10.1016/j.newar.2008.06.004.

P. Padovani. Gamma-Ray Emitting AGN and Unified Schemes. In Y. Giraud-Heraud and J. Tran Thanh van, editors, *Very High Energy Phenomena in the Universe; Moriond Workshop*, page 7, Jan 1997.

S. S. Doeleman, J. Weintroub, A. E. E. Rogers, R. Plambeck, R. Freund, R. P. J. Tilanus, P. Friberg, L. M. Ziurys, J. M. Moran, B. Corey, K. H. Young, D. L. Smythe, M. Titus, D. P. Marrone, R. J. Cappallo, D. C.-J. Bock, G. C. Bower, R. Chamberlin, G. R. Davis, T. P. Krichbaum, J. Lamb, H. Maness, A. E. Niell, A. Roy, P. Strittmatter, D. Werthimer, A. R. Whitney, and D. Woody. Event-horizon-scale structure in the supermassive black hole candidate at the Galactic Centre. , 455:78–80, September 2008. doi: 10.1038/nature07245.

Gravity Collaboration, R. Abuter, A. Amorim, M. Bauböck, J. P. Berger, H. Bonnet, W. Brand ner, Y. Clénet, V. Coudé Du Foresto, P. T. de Zeeuw, C. Deen, J. Dexter, G. Duvert, A. Eckart, F. Eisenhauer, N. M. Förster Schreiber, P. Garcia, F. Gao, E. Gendron, R. Genzel, S. Gillessen, P. Guajardo, M. Habibi, X. Haubois, Th. Henning, S. Hippler, M. Horrobin, A. Huber, A. Jiménez-Rosales, L. Jocou, P. Kervella, S. Lacour, V. Lapeyrère, B. Lazareff, J. B. Le Bouquin, P. Léna, M. Lippa, T. Ott, J. Panduro, T. Paumard, K. Perraut, G. Perrin, O. Pfuhl, P. M. Plewa, S. Rabien, G. Rodríguez-Coira, G. Rousset, A. Sternberg, O. Straub, C. Straubmeier, E. Sturm, L. J. Tacconi, F. Vincent, S. von Fellenberg, I. Waisberg, F. Widmann, E. Wieprecht, E. Wiezorrek, J. Woillez, and S. Yazici. Detection of orbital motions near the last stable circular orbit of the massive black hole SgrA*. , 618:L10, Oct 2018. doi: 10.1051/0004-6361/201834294.

R. Genzel, F. Eisenhauer, and S. Gillessen. The Galactic Center massive black hole and nuclear star cluster. *Reviews of Modern Physics*, 82:3121–3195, October 2010a. doi: 10.1103/RevModPhys.82.3121.

R. Abuter, A. Amorim, M. Bauboeck, J. P. Berger, H. Bonnet, W. Brandner, Y. Clenet, V. Coude du Foresto, P. T. de Zeeuw, J. Dexter, G. Duvert, A. Eckart, F. Eisenhauer, N. M. Foerster Schreiber, P. Garcia, F. Gao, E. Gendron, R. Genzel, O. Gerhard, S. Gillessen, M. Habibi, X. Haubois, T. Henning, S. Hippler, M. Horrobin, A. Jimenez-Rosales, L. Jocou, P. Kervella, S. Lacour, V. Lapeyrere, J. B. Le Bouquin, P. Lena, T. Ott, T. Paumard, K. Perraut, G. Perrin, O. Pfuhl, S. Rabien, G. Rodriguez Coira, G. Rousset, S. Scheithauer, A. Sternberg, O. Straub, C. Straubmeier, E. Sturm, L. J. Tacconi, F. Vincent, S. von Fellenberg, I. Waisberg, F. Widmann, E. Wieprecht, E. Wiezorrek, J. Woillez, and S. Yazici. A geometric distance measurement to the Galactic Center black hole with 0.3% uncertainty. *arXiv e-prints*, art. arXiv:1904.05721, Apr 2019.

A. M. Ghez, S. Salim, N. N. Weinberg, J. R. Lu, T. Do, J. K. Dunn, K. Matthews, M. R. Morris, S. Yelda, E. E. Becklin, T. Kremenek, M. Milosavljevic, and J. Naiman. Measuring Distance and Properties of the Milky Way's Central Supermassive Black Hole with Stellar Orbits. , 689:1044-1062, December 2008. doi: 10.1086/592738.

S. Gillessen, F. Eisenhauer, S. Trippe, T. Alexander, R. Genzel, F. Martins, and T. Ott. Monitoring Stellar Orbits Around the Massive Black Hole in the Galactic Center. , 692: 1075–1109, February 2009a. doi: 10.1088/0004-637X/692/2/1075.

S. Gillessen, F. Eisenhauer, T. K. Fritz, H. Bartko, K. Dodds-Eden, O. Pfuhl, T. Ott, and R. Genzel. The Orbit of the Star S2 Around SGR A* from Very Large Telescope and Keck Data. , 707:L114–L117, December 2009b. doi: 10.1088/0004-637X/707/2/L114.

G. C. Bower, H. Falcke, M. C. Wright, and D. C. Backer. Variable Linear Polarization from Sagittarius A*: Evidence of a Hot Turbulent Accretion Flow. , 618:L29–L32, January 2005. doi: 10.1086/427498.

D. P. Marrone, J. M. Moran, J.-H. Zhao, and R. Rao. The Submillimeter Polarization of Sgr A*. In R. Schödel, G. C. Bower, M. P. Muno, S. Nayakshin, and T. Ott, editors, *Journal of Physics Conference Series*, volume 54 of *Journal of Physics Conference Series*, pages 354–362, December 2006a. doi: 10.1088/1742-6596/54/1/056.

D. P. Marrone, J. M. Moran, J.-H. Zhao, and R. Rao. An Unambiguous Detection of Faraday Rotation in Sagittarius A*. , 654:L57–L60, January 2007. doi: 10.1086/510850.

S. Dibi, S. Drappeau, P. C. Fragile, S. Markoff, and J. Dexter. General relativistic magnetohydrodynamic simulations of accretion on to Sgr A*: how important are radiative losses? , 426:1928–1939, November 2012. doi: 10.1111/j.1365-2966.2012.21857.x.

H. Falcke, W. M. Goss, H. Matsuo, P. Teuben, J.-H. Zhao, and R. Zylka. The Simultaneous Spectrum of Sagittarius A* from 20 Centimeters to 1 Millimeter and the Nature of the Millimeter Excess. , 499:731–734, May 1998a. doi: 10.1086/305687.

D. K. Aitken, J. S. Greaves, A. Chrysostomou, W. S. Holland , J. H. Hough, D. Pierce-Price, and J. S. Richer. Detection of polarized mm and submm emission from SgrA*. *arXiv e-prints*, art. astro-ph/0003379, Mar 2000.

Fulvio Melia, Siming Liu, and Robert Coker. Polarized Millimeter and Submillimeter Emission from Sagittarius A* at the Galactic Center. , 545(2):L117–L120, Dec 2000. doi: 10.1086/317888.

Geoffrey C. Bower, Melvyn C. H. Wright, Heino Falcke, and Donald C. Backer. Interferometric Detection of Linear Polarization from Sagittarius A* at 230 GHz. , 588(1):331–337, May 2003. doi: 10.1086/373989.

Daniel P. Marrone, James M. Moran, Jun-Hui Zhao, and Ramprasad Rao. Interferometric

Measurements of Variable 340 GHz Linear Polarization in Sagittarius A*. , 640(1):308–318, Mar 2006b. doi: 10.1086/500106.

G. C. Bower, S. Markoff, J. Dexter, M. A. Gurwell, J. M. Moran, A. Brunthaler, H. Falcke, P. C. Fragile, D. Maitra, D. Marrone, A. Peck, A. Rushton, and M. C. H. Wright. Radio and Millimeter Monitoring of Sgr A*: Spectrum, Variability, and Constraints on the G2 Encounter. , 802:69, March 2015. doi: 10.1088/0004-637X/802/1/69.

V. L. Fish, S. S. Doeleman, C. Beaudoin, R. Blundell, D. E. Bolin, G. C. Bower, R. Chamberlin, R. Freund, P. Friberg, M. A. Gurwell, M. Honma, M. Inoue, T. P. Krichbaum, J. Lamb, D. P. Marrone, J. M. Moran, T. Oyama, R. Plambeck, R. Primiani, A. E. E. Rogers, D. L. Smythe, J. SooHoo, P. Strittmatter, R. P. J. Tilanus, M. Titus, J. Weintroub, M. Wright, D. Woody, K. H. Young, and L. M. Ziurys. 1.3 mm Wavelength VLBI of Sagittarius A*: Detection of Time-variable Emission on Event Horizon Scales. , 727: L36, February 2011. doi: 10.1088/2041-8205/727/2/L36.

X. Haubois, K. Dodds-Eden, A. Weiss, T. Paumard, G. Perrin, Y. Clénet, S. Gillessen, P. Kervella, F. Eisenhauer, R. Genzel, and D. Rouan. Flares and variability from Sagittarius A*: five nights of simultaneous multi-wavelength observations. , 540:A41, April 2012. doi: 10.1051/0004-6361/201117725.

G. C. Bower, D. Plambeck, and D. Marrone. 1.3mm CARMA Flux Density for Sgr A*. *The Astronomer's Telegram*, 5018, April 2013.

H. B. Liu, M. C. H. Wright, J.-H. Zhao, E. A. C. Mills, M. A. Requena-Torres, S. Matsushita, S. Martín, J. Ott, M. R. Morris, S. N. Longmore, C. D. Brinkerink, and H. Falcke. The 492 GHz emission of Sgr A* constrained by ALMA. , 593:A44, September 2016. doi: 10.1051/0004-6361/201628176.

Event Horizon Telescope Collaboration, K. Akiyama, A. Alberdi, W. Alef, K. Asada, R. Azulay, A.-K. Baczko, D. Ball, M. Baloković, J. Barrett, and et al. First M87 Event Horizon Telescope Results. I. The Shadow of the Supermassive Black Hole. , 875:L1, April 2019a. doi: 10.3847/2041-8213/ab0ec7.

Event Horizon Telescope Collaboration, K. Akiyama, A. Alberdi, W. Alef, K. Asada, R. Azulay, A.-K. Baczko, D. Ball, M. Baloković, J. Barrett, and et al. First M87 Event Horizon Telescope Results. II. Array and Instrumentation. , 875:L2, April 2019b. doi: 10.3847/2041-8213/ab0c96.

Event Horizon Telescope Collaboration, K. Akiyama, A. Alberdi, W. Alef, K. Asada, R. Azulay, A.-K. Baczko, D. Ball, M. Baloković, J. Barrett, and et al. First M87 Event Horizon Telescope Results. III. Data Processing and Calibration. , 875:L3, April 2019c. doi: 10.3847/2041-8213/ab0c57.

Event Horizon Telescope Collaboration, K. Akiyama, A. Alberdi, W. Alef, K. Asada, R. Azulay, A.-K. Baczko, D. Ball, M. Baloković, J. Barrett, and et al. First M87 Event Horizon Telescope Results. IV. Imaging the Central Supermassive Black Hole. , 875:L4, April 2019d. doi: 10.3847/2041-8213/ab0e85.

Event Horizon Telescope Collaboration, K. Akiyama, A. Alberdi, W. Alef, K. Asada, R. Azulay, A.-K. Baczko, D. Ball, M. Baloković, J. Barrett, and et al. First M87 Event Horizon Telescope Results. V. Physical Origin of the Asymmetric Ring. , 875:L5, April 2019e. doi: 10.3847/2041-8213/ab0f43.

Event Horizon Telescope Collaboration, K. Akiyama, A. Alberdi, W. Alef, K. Asada, R. Azulay, A.-K. Baczko, D. Ball, M. Baloković, J. Barrett, and et al. First M87 Event Horizon Telescope Results. VI. The Shadow and Mass of the Central Black Hole. , 875:L6, April 2019f. doi: 10.3847/2041-8213/ab1141.

Ru-Sen Lu, Thomas P. Krichbaum, Alan L. Roy, Vincent L. Fish, Sheperd S. Doeleman, Michael D. Johnson, Kazunori Akiyama, Dimitrios Psaltis, Walter Alef, and Keiichi Asada. Detection of Intrinsic Source Structure at Ì3 Schwarzschild Radii with Millimeter-VLBI Observations of SAGITTARIUS A*. , 859(1):60, May 2018. doi: 10.3847/1538-4357/aabe2e.

Michael D. Johnson, Ramesh Narayan, Dimitrios Psaltis, Lindy Blackburn, Yuri Y. Kovalev, Carl R. Gwinn, Guang-Yao Zhao, Geoffrey C. Bower, James M. Moran, and Motoki Kino. The Scattering and Intrinsic Structure of Sagittarius A* at Radio Wavelengths. , 865(2): 104, Oct 2018. doi: 10.3847/1538-4357/aadcff.

T. Do, A. M. Ghez, M. R. Morris, S. Yelda, L. Meyer, J. R. Lu, S. D. Hornstein, and K. Matthews. A Near-Infrared Variability Study of the Galactic Black Hole: A Red Noise Source with NO Detected Periodicity. , 691:1021–1034, February 2009. doi: 10.1088/0004-637X/691/2/1021.

K. Dodds-Eden, D. Porquet, G. Trap, E. Quataert, X. Haubois, S. Gillessen, N. Grosso, E. Pantin, H. Falcke, D. Rouan, R. Genzel, G. Hasinger, A. Goldwurm, F. Yusef-Zadeh, Y. Clenet, S. Trippe, P.-O. Lagage, H. Bartko, F. Eisenhauer, T. Ott, T. Paumard, G. Perrin, F. Yuan, T. K. Fritz, and L. Mascetti. Evidence for X-Ray Synchrotron Emission from Simultaneous Mid-Infrared to X-Ray Observations of a Strong Sgr A* Flare. , 698:676–692, June 2009. doi: 10.1088/0004-637X/698/1/676.

K. Dodds-Eden, S. Gillessen, T. K. Fritz, F. Eisenhauer, S. Trippe, R. Genzel, T. Ott, H. Bartko, O. Pfuhl, G. Bower, A. Goldwurm, D. Porquet, G. Trap, and F. Yusef-Zadeh. The Two States of Sgr A* in the Near-infrared: Bright Episodic Flares on Top of Low-level Continuous Variability. , 728:37, February 2011. doi: 10.1088/0004-637X/728/1/37.

J. L. Hora, G. Witzel, M. L. N. Ashby, E. E. Becklin, S. Carey, G. G. Fazio, A. Ghez, J. Ingalls, L. Meyer, M. R. Morris, H. A. Smith, and S. P. Willner. Spitzer/IRAC Observations of the Variability of Sgr A* and the Object G2 at 4.5 μm. , 793:120, October 2014. doi: 10.1088/0004-637X/793/2/120.

S. Gillessen, F. Eisenhauer, E. Quataert, R. Genzel, T. Paumard, S. Trippe, T. Ott, R. Abuter, A. Eckart, P. O. Lagage, M. D. Lehnert, L. J. Tacconi, and F. Martins. Variations in the Spectral Slope of Sagittarius A* during a Near-Infrared Flare. , 640: L163–L166, April 2006. doi: 10.1086/503557.

S. D. Hornstein, K. Matthews, A. M. Ghez, J. R. Lu, M. Morris, E. E. Becklin, M. Rafelski, and F. K. Baganoff. A Constant Spectral Index for Sagittarius A* during Infrared/X-Ray Intensity Variations. , 667:900–910, October 2007. doi: 10.1086/520762.

D. P. Marrone, F. K. Baganoff, M. R. Morris, J. M. Moran, A. M. Ghez, S. D. Hornstein, C. D. Dowell, D. J. Muñoz, M. W. Bautz, G. R. Ricker, W. N. Brandt, G. P. Garmire, J. R. Lu, K. Matthews, J.-H. Zhao, R. Rao, and G. C. Bower. An X-Ray, Infrared, and Submillimeter Flare of Sagittarius A*. , 682:373-383, July 2008. doi: 10.1086/588806.

G. Witzel, A. Eckart, M. Bremer, M. Zamaninasab, B. Shahzamanian, M. Valencia-S., R. Schödel, V. Karas, R. Lenzen, N. Marchili, N. Sabha, M. Garcia-Marin, R. M. Buchholz, D. Kunneriath, and C. Straubmeier. Source-intrinsic Near-infrared Properties of Sgr A*: Total Intensity Measurements. , 203:18, December 2012. doi: 10.1088/0067-0049/203/2/18.

Sebastiano D. von Fellenberg, Stefan Gillessen, Javier Graciá-Carpio, Tobias K. Fritz, Jason Dexter, Michi Bauböck, Gabriele Ponti, Feng Gao, Maryam Habibi, and Philipp M. Plewa. A Detection of Sgr A* in the Far Infrared. , 862(2):129, Aug 2018. doi: 10.3847/1538-4357/aacd4b.

F. Eisenhauer, G. Perrin, W. Brandner, C. Straubmeier, A. Richichi, S. Gillessen, J. P. Berger, S. Hippler, A. Eckart, M. Schöller, S. Rabien, F. Cassaing, R. Lenzen, M. Thiel, Y. Clénet, J. R. Ramos, S. Kellner, P. Fédou, H. Baumeister, R. Hofmann, E. Gendron, A. Boehm, H. Bartko, X. Haubois, R. Klein, K. Dodds-Eden, K. Houairi, F. Hormuth, A. Gräter, L. Jocou, V. Naranjo, R. Genzel, P. Kervella, T. Henning, N. Hamaus, S. Lacour, U. Neumann, M. Haug, F. Malbet, W. Laun, J. Kolmeder, T. Paumard, R.-R. Rohloff, O. Pfuhl, K. Perraut, J. Ziegleder, D. Rouan, and G. Rousset. GRAVITY: getting to the event horizon of Sgr A*. In *Optical and Infrared Interferometry*, volume 7013 of , page 70132A, July 2008. doi: 10.1117/12.788407.

B. Balick and R. L. Brown. Intense sub-arcsecond structure in the galactic center. , 194: 265–270, December 1974. doi: 10.1086/153242.

R. Genzel, R. Schödel, T. Ott, A. Eckart, T. Alexander, F. Lacombe, D. Rouan, and B. Aschenbach. Near-infrared flares from accreting gas around the supermassive black hole at the Galactic Centre. , 425:934–937, October 2003. doi: 10.1038/nature02065.

F. K. Baganoff, M. W. Bautz, W. N. Brandt, G. Chartas, E. D. Feigelson, G. P. Garmire, Y. Maeda, M. Morris, G. R. Ricker, L. K. Townsley, and F. Walter. Rapid X-ray flaring from the direction of the supermassive black hole at the Galactic Centre. , 413:45–48, September 2001. doi: 10.1038/35092510.

R. Genzel, F. Eisenhauer, and S. Gillessen. The Galactic Center massive black hole and nuclear star cluster. *Reviews of Modern Physics*, 82:3121–3195, October 2010b. doi: 10.1103/RevModPhys.82.3121.

G. Ponti, B. De Marco, M. R. Morris, A. Merloni, T. Muñoz-Darias, M. Clavel, D. Haggard, S. Zhang, K. Nandra, S. Gillessen, K. Mori, J. Neilsen, N. Rea, N. Degenaar, R. Terrier, and A. Goldwurm. Fifteen years of XMM-Newton and Chandra monitoring of Sgr A^{â}:

evidence for a recent increase in the bright flaring rate. , 454:1525–1544, December 2015. doi: 10.1093/mnras/stv1537.

J.-H. Zhao, G. C. Bower, and W. M. Goss. Radio Variability of Sagittarius A*-a 106 Day Cycle. , 547:L29–L32, January 2001. doi: 10.1086/318877.

Heino Falcke, W. M. Goss, Hiroshi Matsuo, Peter Teuben, Jun-Hui Zhao, and Robert Zylka. The Simultaneous Spectrum of Sagittarius A* from 20 Centimeters to 1 Millimeter and the Nature of the Millimeter Excess. , 499(2):731–734, May 1998b. doi: 10.1086/305687.

R. Zylka, P. G. Mezger, D. Ward-Thompson, W. J. Duschl, and H. Lesch. Anatomy of the Sagittarius A complex. 4: SGR A* and the Central Cavity revisited. , 297:83–97, May 1995.

E. Serabyn, J. Carlstrom, O. Lay, D. C. Lis, T. R. Hunter, J. H. Lacy, and R. E. Hills. High-Frequency Measurements of the Spectrum of Sagittarius A*. , 490:L77–L81, November 1997. doi: 10.1086/311010.

A. Cotera, M. Morris, A. M. Ghez, E. E. Becklin, A. M. Tanner, M. W. Werner, and S. R. Stolovy. Mid-Infrared Imaging of the Central Parsec with Keck. In Heino Falcke, Angela Cotera, Wolfgang J. Duschl, Fulvio Melia, and Marcia J. Rieke, editors, *The Central Parsecs of the Galaxy*, volume 186 of *Astronomical Society of the Pacific Conference Series*, page 240, Jun 1999.

D. Gezari. SGR A* in the Mid-Infrared Reference Frame: The Relationship Between the Radio and Infrared Sources in the Central Parsec. In Heino Falcke, Angela Cotera, Wolfgang J. Duschl, Fulvio Melia, and Marcia J. Rieke, editors, *The Central Parsecs of the Galaxy*, volume 186 of *Astronomical Society of the Pacific Conference Series*, page 234, Jun 1999.

R. Schödel, A. Eckart, K. Mužić, L. Meyer, T. Viehmann, and G. C. Bower. The possibility of detecting Sagittarius A* at 8.6 μm from sensitive imaging of the Galactic center. , 462: L1–L4, January 2007. doi: 10.1051/0004-6361:20066590.

S. D. Hornstein, A. M. Ghez, A. Tanner, M. Morris, E. E. Becklin, and P. Wizinowich. Limits on the Short-Term Variability of Sagittarius A* in the Near-Infrared. , 577(1):L9–L13, Sep 2002. doi: 10.1086/344098.

F. K. Baganoff, Y. Maeda, M. Morris, M. W. Bautz, W. N. Brandt, W. Cui, J. P. Doty, E. D. Feigelson, G. P. Garmire, S. H. Pravdo, G. R. Ricker, and L. K. Townsley. Chandra X-Ray Spectroscopic Imaging of Sagittarius A* and the Central Parsec of the Galaxy. , 591:891–915, July 2003. doi: 10.1086/375145.

Feng Yuan, Eliot Quataert, and Ramesh Narayan. Nonthermal Electrons in Radiatively Inefficient Accretion Flow Models of Sagittarius A*. , 598(1):301–312, Nov 2003a. doi: 10.1086/378716.

V. M. Vasyliunas. A survey of low-energy electrons in the evening sector of the magnetosphere with OGO 1 and OGO 3. , 73:2839–2884, May 1968. doi: 10.1029/JA073i009p02839.

F. Xiao. Modelling energetic particles by a relativistic kappa-loss-cone distribution function in plasmas. *Plasma Physics and Controlled Fusion*, 48:203–213, February 2006. doi: 10.1088/0741-3335/48/2/003.

V. Pierrard and M. Lazar. Kappa Distributions: Theory and Applications in Space Plasmas. , 267:153–174, November 2010. doi: 10.1007/s11207-010-9640-2.

D. Biskamp. Magnetic reconnection via current sheets. *Physics of Fluids*, 29(5):1520–1531, May 1986. doi: 10.1063/1.865670.

D. Biskamp. Magnetic Reconnection in Plasmas. , 242:165–207, March 1996. doi: 10.1007/BF00645113.

E. N. Parker. Sweet's Mechanism for Merging Magnetic Fields in Conducting Fluids. , 62 (4):509–520, Dec 1957. doi: 10.1029/JZ062i004p00509.

P. A. Sweet. The Neutral Point Theory of Solar Flares. In B. Lehnert, editor, *Electromagnetic Phenomena in Cosmical Physics*, volume 6 of *IAU Symposium*, page 123, Jan 1958.

T. Yokoyama, K. Akita, T. Morimoto, K. Inoue, and J. Newmark. Clear Evidence of Reconnection Inflow of a Solar Flare. , 546(1):L69–L72, January 2001. doi: 10.1086/318053.

D. Kagan, L. Sironi, B. Cerutti, and D. Giannios. Relativistic Magnetic Reconnection in Pair Plasmas and Its Astrophysical Applications. , 191:545–573, October 2015. doi: 10.1007/s11214-014-0132-9.

W. Liu, H. Li, L. Yin, B. J. Albright, K. J. Bowers, and E. P. Liang. Particle energization in 3D magnetic reconnection of relativistic pair plasmas. *Physics of Plasmas*, 18(5):052105–052105, May 2011. doi: 10.1063/1.3589304.

K. Makwana, H. Li, F. Guo, and X. Li. Dissipation and particle energization in moderate to low beta turbulent plasma via PIC simulations. In *Journal of Physics Conference Series*, volume 837 of *Journal of Physics Conference Series*, page 012004, May 2017. doi: 10.1088/1742-6596/837/1/012004.

B. Cerutti, G. R. Werner, D. A. Uzdensky, and M. C. Begelman. Beaming and Rapid Variability of High-energy Radiation from Relativistic Pair Plasma Reconnection. , 754: L33, August 2012. doi: 10.1088/2041-8205/754/2/L33.

B. Cerutti, G. R. Werner, D. A. Uzdensky, and M. C. Begelman. Simulations of Particle Acceleration beyond the Classical Synchrotron Burnoff Limit in Magnetic Reconnection:

An Explanation of the Crab Flares. , 770:147, June 2013. doi: 10.1088/0004-637X/770/2/147.

B. Cerutti, G. R. Werner, D. A. Uzdensky, and M. C. Begelman. Three-dimensional Relativistic Pair Plasma Reconnection with Radiative Feedback in the Crab Nebula. , 782:104, February 2014. doi: 10.1088/0004-637X/782/2/104.

L. Sironi and A. Spitkovsky. Relativistic Reconnection: An Efficient Source of Non-thermal Particles. , 783:L21, March 2014. doi: 10.1088/2041-8205/783/1/L21.

T. V. Siversky and V. V. Zharkova. Particle acceleration in a reconnecting current sheet: PIC simulation. *Journal of Plasma Physics*, 75:619–636, October 2009. doi: 10.1017/S0022377809008009.

M. A. Riquelme, E. Quataert, P. Sharma, and A. Spitkovsky. Local Two-dimensional Particle-in-cell Simulations of the Collisionless Magnetorotational Instability. , 755:50, August 2012. doi: 10.1088/0004-637X/755/1/50.

M. W. Kunz, J. M. Stone, and E. Quataert. Magnetorotational Turbulence and Dynamo in a Collisionless Plasma. *Physical Review Letters*, 117(23):235101, December 2016. doi: 10.1103/PhysRevLett.117.235101.

E. N. Parker. The Solar-Flare Phenomenon and the Theory of Reconnection and Annihilation of Magnetic Fields. , 8:177, July 1963. doi: 10.1086/190087.

K. Shibata. New observational facts about solar flares from YOHKOH studies - evidence of magnetic reconnection and a unified model of flares. *Advances in Space Research*, 17(4-5): 9–18, January 1996. doi: 10.1016/0273-1177(95)00534-L.

Yang Su, Astrid M. Veronig, Gordon D. Holman, Brian R. Dennis, Tongjiang Wang, Manuela Temmer, and Weiqun Gan. Imaging coronal magnetic-field reconnection in a solar flare. *Nature Physics*, 9(8):489–493, August 2013. doi: 10.1038/nphys2675.

Markus J. Aschwanden. Global Energetics of Solar Flares. X. Petschek Reconnection Rate and Alfvén Mach Number of Magnetic Reconnection Outflows. , 895(2):134, June 2020. doi: 10.3847/1538-4357/ab8aec.

J. Dexter and P. C. Fragile. Tilted black hole accretion disc models of Sagittarius A*: time-variable millimetre to near-infrared emission. , 432:2252–2272, July 2013. doi: 10.1093/mnras/stt583.

C.-k. Chan, D. Psaltis, F. Özel, L. Medeiros, D. Marrone, A. Sa̧dowski, and R. Narayan. Fast Variability and Millimeter/IR Flares in GRMHD Models of Sgr A* from Strong-field Gravitational Lensing. , 812:103, October 2015a. doi: 10.1088/0004-637X/812/2/103.

G. S. Bisnovatyi-Kogan and A. A. Ruzmaikin. The Accretion of Matter by a Collapsing Star in the Presence of a Magnetic Field. , 28(1):45–59, May 1974. doi: 10.1007/BF00642237.

G. S. Bisnovatyi-Kogan and A. A. Ruzmaikin. The Accretion of Matter by a Collapsing Star in the Presence of a Magnetic Field. II: Self-consistent Stationary Picture. , 42(2):401–424, July 1976. doi: 10.1007/BF01225967.

Igor V. Igumenshchev, Ramesh Narayan, and Marek A. Abramowicz. Three-dimensional Magnetohydrodynamic Simulations of Radiatively Inefficient Accretion Flows. , 592(2): 1042–1059, August 2003. doi: 10.1086/375769.

R. Narayan, I. V. Igumenshchev, and M. A. Abramowicz. Magnetically Arrested Disk: an Energetically Efficient Accretion Flow. , 55:L69–L72, December 2003. doi: 10.1093/pasj/55.6.L69.

R. Narayan, A. SÄ dowski, R. F. Penna, and A. K. Kulkarni. GRMHD simulations of magnetized advection-dominated accretion on a non-spinning black hole: role of outflows. , 426:3241–3259, November 2012. doi: 10.1111/j.1365-2966.2012.22002.x.

Alexander Tchekhovskoy, Ramesh Narayan, and Jonathan C. McKinney. Efficient generation of jets from magnetically arrested accretion on a rapidly spinning black hole. , 418(1):L79–L83, November 2011a. doi: 10.1111/j.1745-3933.2011.01147.x.

A. Chael, M. Rowan, R. Narayan, M. Johnson, and L. Sironi. The role of electron heating physics in images and variability of the Galactic Centre black hole Sagittarius A*. , May 2018. doi: 10.1093/mnras/sty1261.

Gravity Collaboration, R. Abuter, A. Amorim, M. Bauböck, J. B. Berger, H. Bonnet, W. Brand ner, V. Cardoso, Y. Clénet, P. T. de Zeeuw, Y. Dallilar, J. Dexter, A. Eckart, F. Eisenhauer, N. M. Förster Schreiber, P. Garcia, F. Gao, E. Gendron, R. Genzel, S. Gillessen, M. Habibi, X. Haubois, T. Henning, S. Hippler, M. Horrobin, A. Jiménez-Rosales, L. Jochum, L. Jocou, A. Kaufer, P. Kervella, S. Lacour, V. Lapeyrère, J. B. Le Bouquin, P. Léna, M. Nowak, T. Ott, T. Paumard, K. Perraut, G. Perrin, O. Pfuhl, G. Ponti, G. Rodriguez Coira, J. Shangguan, S. Scheithauer, J. Stadler, O. Straub, C. Straubmeier, E. Sturm, L. J. Tacconi, F. Vincent, S. D. von Fellenberg, I. Waisberg, F. Widmann, E. Wieprecht, E. Wiezorrek, J. Woillez, S. Yazici, and G. Zins. The flux distribution of Sgr A*. , 638:A2, June 2020. doi: 10.1051/0004-6361/202037717.

S. M. Ressler, A. Tchekhovskoy, E. Quataert, M. Chand ra, and C. F. Gammie. Electron thermodynamics in GRMHD simulations of low-luminosity black hole accretion. , 454(2): 1848–1870, December 2015. doi: 10.1093/mnras/stv2084.

Aleksander Sądowski, Maciek Wielgus, Ramesh Narayan, David Abarca, Jonathan C. McKinney, and Andrew Chael. Radiative, two-temperature simulations of low-luminosity black hole accretion flows in general relativity. , 466(1):705–725, April 2017. doi: 10.1093/mnras/stw3116.

S. M. Ressler, A. Tchekhovskoy, E. Quataert, and C. F. Gammie. The disc-jet symbiosis emerges: modelling the emission of Sagittarius A* with electron thermodynamics. , 467 (3):3604–3619, May 2017. doi: 10.1093/mnras/stx364.

G. G. Howes. A prescription for the turbulent heating of astrophysical plasmas. , 409: L104–L108, November 2010. doi: 10.1111/j.1745-3933.2010.00958.x.

Michael E. Rowan, Lorenzo Sironi, and Ramesh Narayan. Electron and Proton Heating in Transrelativistic Magnetic Reconnection. , 850(1):29, November 2017. doi: 10.3847/1538-4357/aa9380.

Vladimir Zhdankin, Dmitri A. Uzdensky, Gregory R. Werner, and Mitchell C. Begelman. Electron and Ion Energization in Relativistic Plasma Turbulence. , 122(5):055101, February 2019. doi: 10.1103/PhysRevLett.122.055101.

F. Özel, D. Psaltis, and R. Narayan. Hybrid Thermal-Nonthermal Synchrotron Emission from Hot Accretion Flows. , 541:234–249, September 2000. doi: 10.1086/309396.

F. Yuan, E. Quataert, and R. Narayan. Nonthermal Electrons in Radiatively Inefficient Accretion Flow Models of Sagittarius A*. , 598:301–312, November 2003b. doi: 10.1086/378716.

C.-k. Chan, S. Liu, C. L. Fryer, D. Psaltis, F. Özel, G. Rockefeller, and F. Melia. MHD Simulations of Accretion onto Sgr A*: Quiescent Fluctuations, Outbursts, and Quasiperiodicity. , 701:521–534, August 2009. doi: 10.1088/0004-637X/701/1/521.

K. Dodds-Eden, P. Sharma, E. Quataert, R. Genzel, S. Gillessen, F. Eisenhauer, and D. Porquet. Time-Dependent Models of Flares from Sagittarius A*. , 725:450–465, December 2010. doi: 10.1088/0004-637X/725/1/450.

M. Kusunose and F. Takahara. Synchrotron Blob Model of Infrared and X-ray Flares from Sagittarius A*. , 726:54, January 2011. doi: 10.1088/0004-637X/726/1/54.

D. Ball, F. Özel, D. Psaltis, and C.-k. Chan. Particle Acceleration and the Origin of X-Ray Flares in GRMHD Quasiperiodicity of SGR A. , 826:77, July 2016. doi: 10.3847/0004-637X/826/1/77.

A. A. Chael, R. Narayan, and A. Sa̧dowski. Evolving non-thermal electrons in simulations of black hole accretion. , 470:2367–2386, September 2017. doi: 10.1093/mnras/stx1345.

J. Davelaar, M. Mościbrodzka, T. Bronzwaer, and H. Falcke. General relativistic magnetohydrodynamical κ-jet models for Sagittarius A*. , 612:A34, April 2018. doi: 10.1051/0004-6361/201732025.

N. I. Shakura and R. A. Sunyaev. Reprint of 1973A&A....24..337S. Black holes in binary systems. Observational appearance. , 500:33–51, Jun 1973.

I. D. Novikov and K. S. Thorne. Astrophysics of black holes. In *Black Holes (Les Astres Occlus)*, pages 343–450, Jan 1973.

Ann A. Esin, Jeffrey E. McClintock, and Ramesh Narayan. Advection-Dominated Accretion and the Spectral States of Black Hole X-Ray Binaries: Application to Nova Muscae 1991. , 489(2):865–889, Nov 1997. doi: 10.1086/304829.

Ramesh Narayan and Insu Yi. Advection-dominated Accretion: A Self-similar Solution. , 428:L13, Jun 1994. doi: 10.1086/187381.

Marek A. Abramowicz, Xingming Chen, Shoji Kato, Jean-Pierre Lasota, and Oded Regev. Thermal Equilibria of Accretion Disks. , 438:L37, Jan 1995. doi: 10.1086/187709.

Xingming Chen, Marek A. Abramowicz, and Jean-Pierre Lasota. Advection-dominated Accretion: Global Transonic Solutions. , 476(1):61–69, Feb 1997. doi: 10.1086/303592.

Steven A. Balbus and John F. Hawley. A Powerful Local Shear Instability in Weakly Magnetized Disks. I. Linear Analysis. , 376:214, Jul 1991. doi: 10.1086/170270.

John F. Hawley and Steven A. Balbus. A Powerful Local Shear Instability in Weakly Magnetized Disks. II. Nonlinear Evolution. , 376:223, Jul 1991. doi: 10.1086/170271.

C. F. Gammie, J. C. McKinney, and G. Tóth. HARM: A Numerical Scheme for General Relativistic Magnetohydrodynamics. , 589:444–457, May 2003. doi: 10.1086/374594.

J. C. McKinney and C. F. Gammie. A Measurement of the Electromagnetic Luminosity of a Kerr Black Hole. , 611:977–995, August 2004. doi: 10.1086/422244.

Jean-Pierre De Villiers and John F. Hawley. Global General Relativistic Magnetohydrodynamic Simulations of Accretion Tori. , 592(2):1060–1077, Aug 2003. doi: 10.1086/375866.

Peter Anninos, P. Chris Fragile, and Jay D. Salmonson. Cosmos++: Relativistic Magnetohydrodynamics on Unstructured Grids with Local Adaptive Refinement. , 635(1):723–740, Dec 2005. doi: 10.1086/497294.

Matthew D. Duez, Yuk Tung Liu, Stuart L. Shapiro, and Branson C. Stephens. Relativistic magnetohydrodynamics in dynamical spacetimes: Numerical methods and tests. , 72(2): 024028, Jul 2005. doi: 10.1103/PhysRevD.72.024028.

Masaru Shibata and Yu-Ichirou Sekiguchi. Magnetohydrodynamics in full general relativity: Formulation and tests. , 72(4):044014, Aug 2005. doi: 10.1103/PhysRevD.72.044014.

Yosuke Mizuno, Ken-Ichi Nishikawa, Shinji Koide, Philip Hardee, and Gerald J. Fishman. General Relativistic Magnetohydrodynamic Simulations of Jet Formation with a Thin Keplerian Disk. *arXiv e-prints*, art. astro-ph/0609344, Sep 2006.

Luis Antón, Olindo Zanotti, Juan A. Miralles, José M. Martí, José M. Ibáñez, José A. Font, and José A. Pons. Numerical 3+1 General Relativistic Magnetohydrodynamics: A Local Characteristic Approach. , 637(1):296–312, Jan 2006. doi: 10.1086/498238.

Matthew Anderson, Eric W. Hirschmann, Steven L. Liebling, and David Neilsen. Relativistic MHD with adaptive mesh refinement. *Classical and Quantum Gravity*, 23(22):6503–6524, Nov 2006. doi: 10.1088/0264-9381/23/22/025.

Yu-Ichirou Sekiguchi and Masaru Shibata. Axisymmetric collapse simulations of rotating massive stellar cores in full general relativity: Numerical study for prompt black hole formation. , 71(8):084013, Apr 2005. doi: 10.1103/PhysRevD.71.084013.

Bruno Giacomazzo and Luciano Rezzolla. WhiskyMHD: a new numerical code for general relativistic magnetohydrodynamics. *Classical and Quantum Gravity*, 24(12):S235–S258, Jun 2007. doi: 10.1088/0264-9381/24/12/S16.

L. Del Zanna, O. Zanotti, N. Bucciantini, and P. Londrillo. ECHO: a Eulerian conservative high-order scheme for general relativistic magnetohydrodynamics and magnetodynamics. , 473(1):11–30, Oct 2007. doi: 10.1051/0004-6361:20077093.

P. Cerdá-Durán, J. A. Font, L. Antón, and E. Müller. A new general relativistic magnetohydrodynamics code for dynamical spacetimes. , 492(3):937–953, Dec 2008. doi: 10.1051/0004-6361:200810086.

Feng Yuan, Jun Lin, Kinwah Wu, and Luis C. Ho. A magnetohydrodynamical model for the formation of episodic jets. , 395(4):2183–2188, Jun 2009. doi: 10.1111/j.1365-2966.2009.14673.x.

Zachariah B. Etienne, Yuk Tung Liu, and Stuart L. Shapiro. Relativistic magnetohydrodynamics in dynamical spacetimes: A new adaptive mesh refinement implementation. , 82 (8):084031, Oct 2010. doi: 10.1103/PhysRevD.82.084031.

Akshay K. Kulkarni, Robert F. Penna, Roman V. Shcherbakov, James F. Steiner, Ramesh Narayan, Aleksander Sä Dowski, Yucong Zhu, Jeffrey E. McClintock, Shane W. Davis, and Jonathan C. McKinney. Measuring black hole spin by the continuum-fitting method: effect of deviations from the Novikov-Thorne disc model. , 414(2):1183–1194, Jun 2011. doi: 10.1111/j.1365-2966.2011.18446.x.

Monika Mościbrodzka and Heino Falcke. Coupled jet-disk model for Sagittarius A*: explaining the flat-spectrum radio core with GRMHD simulations of jets. , 559:L3, Nov 2013. doi: 10.1051/0004-6361/201322692.

Aleksander Sądowski, Ramesh Narayan, Alexander Tchekhovskoy, David Abarca, Yucong Zhu, and Jonathan C. McKinney. Global simulations of axisymmetric radiative black hole accretion discs in general relativity with a mean-field magnetic dynamo. , 447(1):49–71, Feb 2015. doi: 10.1093/mnras/stu2387.

Chi-kwan Chan, Dimitrios Psaltis, Feryal Özel, Lia Medeiros, Daniel Marrone, Aleksander Saážowski, and Ramesh Narayan. Fast Variability and Millimeter/IR Flares in GRMHD Models of Sgr A* from Strong-field Gravitational Lensing. , 812(2):103, Oct 2015b. doi: 10.1088/0004-637X/812/2/103.

Mani Chandra, Francois Foucart, and Charles F. Gammie. grim: A Flexible, Conservative

Scheme for Relativistic Fluid Theories. , 837(1):92, Mar 2017. doi: 10.3847/1538-4357/aa5f55.

Ya-Ping Li, Feng Yuan, and Q. Daniel Wang. A magnetohydrodynamic model for multi-wavelength flares from Sagittarius A* (I): model and the near-infrared and X-ray flares. , 468(3):2552–2568, Jul 2017. doi: 10.1093/mnras/stx655.

S. M. Ressler, E. Quataert, and J. M. Stone. Hydrodynamic simulations of the inner accretion flow of Sagittarius A* fuelled by stellar winds. , 478(3):3544–3563, Aug 2018. doi: 10.1093/mnras/sty1146.

Benjamin R. Ryan, Sean M. Ressler, Joshua C. Dolence, Charles Gammie, and Eliot Quataert. Two-temperature GRRMHD Simulations of M87. , 864(2):126, September 2018. doi: 10.3847/1538-4357/aad73a.

Benjamin R. Ryan, Joshua C. Dolence, Charles F. Gammie, Sean M. Ressler, and Jonah Miller. EBHLIGHT: General relativistic radiation magnetohydrodynamics with Monte Carlo transport, Sep 2019.

Fernando F Grinstein, Len G Margolin, and William J Rider. *Implicit large eddy simulation: computing turbulent fluid dynamics*. Cambridge university press, 2007.

M. Miesch, W. Matthaeus, A. Brandenburg, A. Petrosyan, A. Pouquet, C. Cambon, F. Jenko, D. Uzdensky, J. Stone, S. Tobias, J. Toomre, and M. Velli. Large-Eddy Simulations of Magnetohydrodynamic Turbulence in Heliophysics and Astrophysics. , 194:97–137, November 2015. doi: 10.1007/s11214-015-0190-7.

L. G. Fishbone and V. Moncrief. Relativistic fluid disks in orbit around Kerr black holes. , 207:962–976, August 1976. doi: 10.1086/154565.

Gábor Tóth. The ∇·b=0 constraint in shock-capturing magnetohydrodynamics codes. *Journal of Computational Physics*, 161(2):605–652, jul 2000. doi: 10.1006/jcph.2000.6519. URL `https://doi.org/10.1006/jcph.2000.6519`.

Sean M. Carroll. *Spacetime and geometry: An introduction to general relativity.* 2004. ISBN 0805387323, 9780805387322. URL `http://www.slac.stanford.edu/spires/find/books/www?cl=QC6:C37:2004`.

S. A. Orszag and C.-M. Tang. Small-scale structure of two-dimensional magnetohydrodynamic turbulence. *Journal of Fluid Mechanics*, 90:129–143, January 1979. doi: 10.1017/S002211207900210X.

N. F. Loureiro, A. A. Schekochihin, and S. C. Cowley. Instability of current sheets and formation of plasmoid chains. *Physics of Plasmas*, 14(10):100703–100703, October 2007. doi: 10.1063/1.2783986.

Scott C. Noble, Julian H. Krolik, and John F. Hawley. Direct Calculation of the Radiative Efficiency of an Accretion Disk Around a Black Hole. , 692(1):411–421, Feb 2009. doi: 10.1088/0004-637X/692/1/411.

Yohei Kawazura, Michael Barnes, and Alexander A. Schekochihin. Thermal disequilibration of ions and electrons by collisionless plasma turbulence. *Proceedings of the National Academy of Science*, 116(3):771–776, January 2019. doi: 10.1073/pnas.1812491116.

T. G. Cowling. The magnetic field of sunspots. , 94:39–48, Nov 1933. doi: 10.1093/mnras/94.1.39.

H. K. Moffatt. *Magnetic field generation in electrically conducting fluids.* 1978.

John F. Hawley and Steven A. Balbus. A Powerful Local Shear Instability in Weakly Magnetized Disks. III. Long-Term Evolution in a Shearing Sheet. , 400:595, Dec 1992. doi: 10.1086/172021.

Jeremy Goodman and Guohong Xu. Parasitic Instabilities in Magnetized, Differentially Rotating Disks. , 432:213, Sep 1994. doi: 10.1086/174562.

Steven A. Balbus and John F. Hawley. Instability, turbulence, and enhanced transport in accretion disks. *Reviews of Modern Physics*, 70(1):1–53, Jan 1998. doi: 10.1103/RevModPhys.70.1.

G. B. Rybicki and A. P. Lightman. *Radiative Processes in Astrophysics.* June 1986.

Feng Yuan and Ramesh Narayan. Hot Accretion Flows Around Black Holes. , 52:529–588, Aug 2014. doi: 10.1146/annurev-astro-082812-141003.

A. Pandya, Z. Zhang, M. Chandra, and C. F. Gammie. Polarized Synchrotron Emissivities and Absorptivities for Relativistic Thermal, Power-law, and Kappa Distribution Functions. , 822:34, May 2016. doi: 10.3847/0004-637X/822/1/34.

S. C. Noble, P. K. Leung, C. F. Gammie, and L. G. Book. Simulating the emission and outflows from accretion discs. *Classical and Quantum Gravity*, 24:S259–S274, June 2007. doi: 10.1088/0264-9381/24/12/S17.

M. Mościbrodzka, C. F. Gammie, J. C. Dolence, H. Shiokawa, and P. K. Leung. Radiative Models of SGR A* from GRMHD Simulations. , 706:497–507, November 2009. doi: 10.1088/0004-637X/706/1/497.

M. Mościbrodzka and C. F. Gammie. IPOLE - semi-analytic scheme for relativistic polarized radiative transport. , 475:43–54, March 2018. doi: 10.1093/mnras/stx3162.

Alexander Tchekhovskoy, Ramesh Narayan, and Jonathan C. McKinney. Efficient generation of jets from magnetically arrested accretion on a rapidly spinning black hole. , 418(1):L79–L83, November 2011b. doi: 10.1111/j.1745-3933.2011.01147.x.

Prateek Sharma, Eliot Quataert, Gregory W. Hammett, and James M. Stone. Electron Heating in Hot Accretion Flows. , 667(2):714–723, October 2007. doi: 10.1086/520800.